DISPERSION CHARACTERISTICS AND EFFECT OF HEATING RATES ON THE MECHANICAL PROPERTIES OF SPARK PLASMA SINTERED MULTI-WALLED CARBON NANOTUBES REINFORCED NICKEL ALUMINIDE COMPOSITES

By

OLUSOJI OLUREMI AYODELE

SUBMITTED IN PARTIAL FULFILMENT OF THE REQUIREMENTS FOR THE DEGREE

DOCTOR OF PHILOSOPHY

In the

School of Mining, Metallurgy and Chemical Engineering,

FACULTY OF ENGINEERING AND THE BUILT ENVIRONMENT

UNIVERSITY OF JOHANNESBURG, SOUTH AFRICA

Supervisor: Prof. P.A. Olubambi

Co-Supervisor: Dr. M.B. Shongwe

Co-Supervisor: Prof. L. Bichler

February 2020

DECLARATION

I hereby declare that the thesis submitted for Doctor of Philosophy Degree, at University of Johannesburg, South Africa, is my actual research work. It has not been presented to any other institution of higher education. The sources cited are listed and acknowledged by means of references.

……

Olusoji Oluremi Ayodele

DEDICATION

This research work is dedicated to Jehovah for being the source of my life, in Him I live and move and have my being.

ACKNOWLEDGEMENTS

I would like to proffer my deepest appreciation to my supervisor, Prof. Peter Apata Olubambi for his immense guidance and support through words of wisdom and finances through the entire duration of this study. I acknowledge him for this ample privilege he has given me to learn, make mistakes, and take decisions based on this study. I appreciate all your support to make me a better person. I would like to thank my co-supervisors, Dr. Mxolisi Brendon Shongwe for allowing me to use the facilities of Tshwane University of Technology, Pretoria and Dr. Adewale Olawale Adegbenjo for his understanding, assistance and support during the duration of my research work. Thank you for the courage to point out my mistakes. Also, to Prof. Lukas Bichler for his kind heart and support throughout my stay at the University of British Columbia, Okanagan, Canada. I want to thank my colleagues in Centre for Nanoengineering and Tribocorrosion Lab for their love, guidance and patience throughout this study. My appreciation goes to Dr. Segun Falodun, Dr. Ranti Oke, Mr. Jeremaih Akinribide, Mr. Samuel Akinwamide, Mr. Moses Okoro, Mr. Tajudeen Mojisola, Ms. Mosima Maja, Mr. Olusola Ayeleru and Mrs. Mary Awotunde for your unending effort and contributions during this study. To my senior researcher, Dr. Babatunde Obadele, thank you for reading and correcting my manuscripts. My profound gratitude goes to my families whom have supported me on all side, thank for your love Mr. and Mrs. Ayodele, Engr. David Fulani, Mr. Dele Fulani, Ms. Abimbola Ayodele and Mr. Sumbo Jones. I will not forget to acknowledge my beloved, Miss Inioluwalayomi Olaniyi for her prayers, love, and support. I would also like to express my gratitude my colleagues at the University of British Columbia, Okanagan, for their willingness to assist me at all time.

ABSTRACT

The dispersion of multi-walled carbon nanotubes (MWCNTs) in NiAl matrix was successfully carried out through the combination of two steps planetary ball millings. Low energy ball milling (LEBM) was employed for preliminary milling of the starting powders at 150 rpm. Subsequently, the milled powders were transferred to the high energy ball milling (HEBM) for auxiliary milling, and to ensure proper dispersion. This was performed at different milling hours (1 h, 2 h and 3 h) to further de-bundle the MWCNTs. The milled powders were consolidated via spark plasma sintering (SPS) using the sintering temperature of 1000 ^{o}C, sintering pressure of 50 MPa, holding time of 10 min and heating rates from 50-150 ^{o}C/min. The morphology of the milled powders and the consolidated compacts were observed using the scanning electron microscopy (SEM) and the structural and phase identifications were examined through the X-ray diffractometer (XRD). Raman spectroscopy was used to determine the structural integrity of MWCNTs in the metal matrix and Transmission electron microscopy (TEM) revealed the level of damages or defects done to the MWCNTs. The SEM micrograph of the consolidated NiAl-1wt% MWCNTs composite (HEBM, 1 hour) revealed a relative dispersion of MWCNTs with a few agglomerations and this was corroborated by the TEM images. Furthermore, the Vickers microhardness and relative density of the consolidated samples was observed to decrease as the heating rate was increased and further increase in heating rate led to the increase in the density of the consolidated NiAl. Conversely, the Vickers microhardness and relative density of the consolidated NiAl-1wt% MWCNTs composites decreased as the heating rate was increased from 50-150 ^{o}C/min. The nanoindentation plot indicates that the sintered samples with higher penetration depths at the indentation load of 75 mN had lower nanohardness values. MWCNTs was observed to have decreased the coefficient of friction due to the formation of lubricating tribolayer at the contact

surface. The crystallographic orientations of all the consolidated samples revealed no texture and the mean grain size of the consolidated composites were found to increase, as the heating rate was increased. These findings revealed that NiAl-MWCNTs may be exploited as a potential aerospace application especially in the area of turbine coating.

PUBLICATIONS

JOURNAL PAPERS

1. **Olusoji Oluremi Ayodele,** Mary Ajimegoh Awotunde, Mxolisi Brendon Shongwe, Adewale Oladapo Adegbenjo, Bukola Joseph Babalola, Ayorinde Tayo Olanipekun and Peter Apata Olubambi. 2019. Carbon nanotube-reinforced intermetallic matrix composites: processing challenges, consolidation, and mechanical properties. **The International Journal of Advanced Manufacturing Technology, 1-18**
2. **Olusoji Oluremi Ayodele,** Adewale Oladapo Adegbenjo, Mary Ajimegoh Awotunde, Mxolisi Brendon Shongwe, and Peter Apata Olubambi. 2019. The influence of hearting rate on the microstructural evolutions and mechanical properties of spark plasma sintered multi-walled carbon nanotubes reinforced NiAl intermetallic matrix composites. **Materials Science and Engineering A, Volume 773, 138869.**
3. **Olusoji Oluremi Ayodele,** Mary Ajimegoh Awotunde**,** Mxolisi Brendon Shongwe, Adewale Oladapo Adegbenjo, Bukola Joseph Babalola, Babatunde Abiodun Obadele, and Peter Apata Olubambi. 2019. Effect of heating rate on the microstructure and mechanical properties of spark plasma sintered CNTs reinforced nickel aluminide. **Key Engineering Materials, Volume 821, 440-444**
4. **Olusoji Oluremi Ayodele,** Lukas Bichler**,** Adewale Oladapo Adegbenjo, Mary Ajimegoh Awotunde, Mxolisi Brendon Shongwe, and Peter Apata Olubambi. 2020. Nanoindentation and wear analysis of spark plasma sintered carbon nanotubes reinforced nickel aluminide composite. **Journal of Alloys and Compound** (**Submitted)**
5. **Olusoji Oluremi Ayodele,** Lukas Bichler**,** Adewale Oladapo Adegbenjo, Mary Ajimegoh Awotunde, Mxolisi Brendon Shongwe, and Peter Apata Olubambi. 2020.

Synthesis of NiAl-MWCNT composite via spark plasma sintering: effect of heating rate parameters and agglomerations on densification, hardness and grain size. **Materials and Design** (**Submitted)**

CONFERENCES

1. **Olusoji Oluremi Ayodele,** Adewale Oladapo Adegbenjo, Mary Ajimegoh Awotunde, Samuel Olukayode Akinwamide, Mxolisi Brendon Shongwe, and Peter Apata Olubambi. 2020. Planetary ball milling of MWCNTs reinforced NiAl composites. **Materials Today: Proceedings** 1-5
2. **Olusoji Oluremi Ayodele,** Adewale Oladapo Adegbenjo, Mary Ajimegoh Awotunde, Babatunde Abiodun Obadele, Mxolisi Brendon Shongwe and Peter Apata Olubambi. 2020. Synthesis and heating rate effect on the mechanical properties of NiAl intermetallic compound. **Materials Today: Proceedings** 1-5

TABLE OF CONTENT

LISTS OF FIGURES

LIST OF TABLES

CHAPTER ONE

1. INTRODUCTION

Monolithic materials appear to have proved inefficient to meet the required performance and economic target for diverse applications, where high stiffness and strength are desired at elevated temperatures (Munir *et al.*, 2015). However, novel technological developments (e.g., gas turbine engines) require materials to operate at even higher temperature and harsher in-service conditions. Additives such as, multi-walled carbon nanotubes (MWCNTs) have been recognized as a potential reinforcing agent for the next generation of metal matrix composites (MMCs). This has been primarily driven by the high thermo-mechanical properties of MWCNTs (Bakshi *et al.*, 2010). Upon the discovery of nanotubes by Sumio Iijima (1991), studies reporting on the theoretical properties of CNTs suggest a tensile strength of 100 GPa, Young's modulus up to 1 TPa, low density (1.7-2.1 gcm^{-3}), high aspect ratios and high thermal and electrical conductivities (Esawi *et al.*, 2010; Allaedini *et al.*, 2016; Kumar *et al.*, 2017). The desirable properties of MWCNTs are attributed to the presence of strong sp^2 carbon-carbon networks in their outermost shells and their smooth and continuous cylindrical morphology (Munir *et al.*, 2017a). The sp^2 carbon-carbon networks establish closed hexagonal structures (honeycomb), which serve as the source of their excellent thermo-mechanical characteristics (Zhu *et al.*, 2010; Munir *et al.*, 2015).

Research focusing on the effect of MWCNTs to enhance the titanium alloys, aluminum and nickel alloys has been reported in the literature (Reinert *et al.*, 2015 ; Ameri *et al.*, 2016; Adegbenjo *et al.*,, 2017; Cavaliere *et al.*, 2017; Okoro *et al.*, 2019). The addition of CNTs led to an increase in porosity and tensile strength of Al-CNTs by 24.5% according to the studies by Cavaliere *et al.* (2017). It was also observed to increase the hardness and the fracture toughness of NiAl-CNTs composites by 6.4 % (Ameri *et al.*, 2016). Past studies by Qian *et al.*, (2000), revealed that the addition of 1 wt % CNTs to polymer matrix yielded an increase in elastic modulus by 36-42 %.

Despite these promising results, using MWCNTs as novel reinforcements in metal matrices for industrial applications has not been realized, primarily due to the large aspect ratios, nano-scale dimensions and the presence of strong Van der Waal forces which impedes the dispersion of MWCNTs in metal matrices (Bakshi et al., 2010; Thostenson et al., 2001).Therefore, achieving a homogeneous dispersion of MWCNTs in matrices, as well as preserving their structural integrity is still a major challenge. Previous investigations on dispersion of MWCNTs within metal matrices, e.g., Ti, Al and Cu have been studied (Esawi et al., 2010; Adegbenjo et al., 2018; Munir et al., 2018; Xiong et al., 2019). They found out that homogeneous dispersion of MWCNTs within the metal matrix contributes to the significant improvement in the mechanical attributes of the composites, but the reinforcement of intermetallics with MWCNTs have not been sufficiently explored.

NiAl has a very high potential for expanded use in industry, especially as high temperature structural material, due to its high mechanical properties at elevated temperatures, excellent corrosion and oxidation resistance, high thermal conductivity and light weight (Grabke, 1999; Hu *et al.,* 2006). These properties made NiAl a material of choice for aerospace applications (e.g., compressors and turbine blades) and combustion systems (e.g., piston rings and valves (Darolia, 1991). However, the low ductility and fracture toughness of NiAl at ambient temperature have limited wider use of this material (Geist *et al.,* 2015).Various approaches to overcome these challenges were explored through second phase strengthening, grain refinement and alloying (Ameri *et al.,* 2016), but with limited success. The incorporation of boron in nickel aluminides was observed to increase the strength and the ductility of the composite by 40 %, after doping with 0.04 wt.% boron (Liu *et al.,* 1985; Meng *et al.,* 2006; Mohammadnejad *et al.,* 2018).

The improvement of mechanical properties of NiAl through the doping with MW-CNTs was typically achieved through powder metallurgical processes (PMs). PM entails the milling or mixing of powders through the planetary ball milling, and the process development for fabricating fully dense composites (Obadele *et al.,* 2017). High energy planetary ball milling (HEBM) has been employed to achieve the dispersion of MWCNTs in metal matrices (Jia *et al.,* 2009; Esawi *et al.,* 2010). However, for non-optimal milling conditions, MWCNTs may encounter extreme bending stresses leading to CNT buckling (Munir *et al.,* 2017). Past studies by Oh *et al.* (2007) show that HEBM creates defects in MWCNTs by transforming sp^2 carbon-carbon networks into sp^3 carbon-carbon bonds. This may result into the loss of the unique characteristic, create open edges and vacancies in MWCNTs. Thus, promoting interfacial reactions at the matrix and carbon nanotube interface region (Gill & Munroe, 2012). In addition, the investigations by Liu *et al.,* (2012) on CNTs /Al composite showed a gradual dispersion of MWCNTs in Al matrix through the use of HEBM. A homogeneous dispersion of MWCNTs was observed at the deterioration of the integrity of the carbon nanotubes in the metal matrix during the milling procedure for 4-12 h. Homogeneous dispersion was realized after ball milling for 6 h together with defects (shortenings) of nanotubes, and it increased with the milling time. The defects formed during ball milling are sites for the brittle phase formation which may be deleterious in fabricating composites with good mechanical properties.

Recently, spark plasma sintering (SPS) has been used to realize fully dense composites from initial powders. SPS is a pressure driven process with the use of pulsed direct current (Azarniya, Azarniya, et al., 2017). This process is characterized by uniform sintering, rapid heating rate, high energy efficiency, minimized grain growth and better activation of powder surface (Tokita, 2015). SPS is used to fabricate complex alloys and composites with enhanced mechanical properties. The

sintering mechanisms of SPS entail the activation of powder surface, neck formation and growing of neck, and plastic deformation of the powder (Zhaohui *et al.,* 2008). The potential utilization of spark plasma sintered (SPSed) components are found in aerospace, automobile, biomedical and chemical industries. It is worth note that the effects of sintering parameters on SPSed composites play crucial roles in improving the microstructures and the mechanical properties of the consolidated materials. Some of these parameters include the sintering temperature, pressure, heating rate and sintering time. It was reported that the combination of the sintering temperature and time during SPS had positive impacts on the mechanical properties and sinterability of the bulk sample as compared to the compressive pressure (Khalil *et al.,* 2011). It is also noticeable from the literatures that high sintering temperature and low heating rate are necessary to achieve good densification (Lee *et al.,* 2011, Devaraj *et al.,* 2013). Thus far, the process parameters of MWCNTs /NiAl composites have not been sufficiently reported in the literature. Hence, this research work focused on the dispersion characteristics and the influence of heating rate on the mechanical properties and microstructures of spark plasma sintered carbon nanotubes reinforced nickel aluminide composites.

1.1 RESEARCH PROBLEM

NiAl has been observed with the challenges of low fracture toughness and ductility at room temperature, and this has limited the broad use of this material (Ameri *et al.,* 2016). MWCNTs has been adopted in this research to improve the properties of NiAl. Meanwhile, the dispersion of MWCNTs within the metal matrix has not been fully realized due to the agglomeration of MWCNTs, nano-scale dimensions and strong van der Waals forces present among individual nanotubes (Chen *et al.,*, 2016). This is a key processing challenge that impedes the homogeneous dispersion of MWCNTs in metal matrix (Thostenson *et al.,* 2001).

High energy ball milling (HEBM) through powder metallurgy process has been used to de-bundle and further achieve uniform dispersions of MWCNTs within the metal matrix because it is economical and effective to use (Chen *et al.,* 2015; Liao & Tan, 2011). However, HEBM could damage the walls of MWCNTs during harsh ball milling, thus causing structural defects in the network of MWCNTs (Chen *et al.,* 2015). This leads to loss of unique features, where a non-sp^2 disorders are produced in the C-C bonds of MWCNTs, and results to open edges and vacancies formation in MWCNTs (Oh *et al.,* 2007). In addition, sp^3 C-C amorphous phases could cause interfacial reactions during milling, thus promoting carbides formation (Huang & Terentjev, 2012). Weak bonding between the metal matrix and MWCNTs may lead into non-uniform dispersion of MWCNTs (Bhat et al., 2011), and this could hinder the effectiveness of load sharing abilities by MWCNTs. It is significant to enhance the strengthening mechanism of the composites by retaining the load bearing ability of MWCNTs during processing times (Goh *et al.,*2005; Xing *et al.,* 2005).

1.2 AIM AND OBJECTIVES

The aim of this research work is to investigate the effect of heating rates on the microstructural evolutions and mechanical properties of dispersed multi-walled carbon nanotube reinforced nickel aluminide composites. The results from this investigation would be relevant for the design of ultra-light components that are utilized in aerospace industries. The aim of this research would be accomplished through these objectives:

I. Investigate the dispersion and synthesis of MWCNTs reinforced NiAl matrix composites.
II. Evaluate the microstructural evolutions and phase identifications of the milled powders.
III. Investigate the mechanical properties of the consolidated NiAl and NiAl-1wt% MWCNTs composites.

IV. Evaluate the effect of MWCNTs on the wear properties of the composites.

V. Evaluate the effect of heating rates on the grain size of the consolidated composites.

1.3 JUSTIFICATION FOR THIS STUDY

The reason for selecting NiAl as a material choice is because of their promising mechanical properties and benefits in aerospace applications, especially over the nickel base superalloys. One of key potential applications of NiAl is as a high-pressure turbine blade due to its low density, which can lower the weight of the turbine rotor by 40 % (Bochenek & Basista, 2015). Also, it is important to note that the temperature distribution in the turbine blade is much even as a result of the high thermal conductivity of NiAl, as compared with nickel base superalloys. Other advantages of NiAl includes good oxidation resistance and high melting temperature which is about 300 ^{o}C higher than the nickel base superalloys (Darolia, 1991). However, incorporating NiAl with carbon nanomaterials (MWCNTs) possessing excellent thermo-mechanical properties would further improve the properties of the composite. For instance, the wear properties of the composite may be improved due to the formation of a lubricating tribolayer by the MWCNTs. The role of the heating rates on the microstructures and mechanical properties of the sintered composite is a key factor that has not been or sufficiently explored.

1.4 SCOPE OF THE STUDY

This study involves the use of the existing technique in the literature to disperse MWCNTs in NiAl metal matrix, by using two steps ball millings. The as-received MWCNTs, Ni, Al powders were synthesized, and the milled powders were characterized. The consolidation of the admixed powders was prepared by SPS and the effect of heating rates was observed. Varying metallurgical interactions such as microstructural evolutions, phase identifications, mechanical properties and interface analysis of the sintered bulk samples were investigated.

1.5 STRUCTURE OF THE STUDY

Chapter One highlights the introduction of this study, research problems, aim and objectives, justification and the scope of this study. **Chapter Two** presents the literature review on metal matrix composites, nickel aluminide, carbon nanotubes, dispersion and synthesis of carbon nanotubes, ball milling and the influence of ball milling, sintering parameters and their effects on the mechanical properties of CNT reinforced metal matrix composites. **Chapter Three** shows the materials, methods and the equipment used for this investigation. The morphology of the starting and the admixed powders, XRD analysis and Raman analysis of the MWCNTs and NiAl-MWCNTs composites, dispersion characteristics of MWCNTs and NiAl-MWCNTs composites are discussed in **Chapter Four. Chapter Five** entails the SEM morphology of the consolidated NiAl and NiAl-MWCNTs composites with different HEBM dispersion time, fracture morphology, grain size analysis, inverse pole and pole figure maps. Meanwhile the densification mechanisms, microhardness, nanoindentation analysis, nanohardness and elastic modulus, the wear behaviour and the coefficient of friction of the sintered composites are discussed in **Chapter Six.** The contributions to knowledge, conclusions and recommendations from this investigation are highlighted in **Chapter Seven.**

CHAPTER TWO

2 LITERATURE REVIEW

This chapter illustrates the previous, present and future investigations on metal matrix composites, nickel aluminide, carbon nanotubes, their dispersion and synthesis, powder metallurgy and the role of sintering parameters.

2.1 METAL MATRIX COMPOSITES

Metal matrix composites (MMCs) comprises of two or more distinct phases which are usually metal matrix and reinforcing phases. In MMCs, stiffness and strength are attained by reinforcing materials whereas strength and ductility are obtained from the matrix (Bakshi et al., 2010). MMCs possesses bulk characteristics that are remarkably different from their constituents (Das *et al.*, 1997). These properties include excellent strength to density ratio, higher stiffness, lower creep rate, excellent wear resistance, good fatigue resistance and lower coefficient of thermal expansion (Cavaliere *et al.*, 2017). Due to these outstanding features, MMCs are applied in automobile as pistons and valves, also in aerospace as turbine blades, compressor, and exhaust manifold of aircraft. MMCs are significant in synthesizing unique materials that have the capability to perform at elevated temperature through appropriate combination of metals such as Mg, Al, Cu, Ti, and Ni with diverse reinforcing material which include TiB, TiN, CNT, SiC, etc (Nardone & Prewo, 1986; Rohatgi *et al.*, 1991; Falodun *et al.*, 2019). Several metals have been utilized as matrices, the most common matrices are aluminium matrix, titanium matrix, magnesium matrix and copper matrix and nickel matrix. Nickel based composites can operate at higher temperatures as compared with Titanium-base composites which are applicable at low or intermediate temperatures because of oxidation problems (Nathal, 1995).

2.2 MATRIX

Matrix material is a monolithic material which exhibits desirable physical and mechanical properties. A matrix has a continuous character, into which the reinforcements are incorporated. The matrix imparts ductility and protects the reinforcement from surface damage. Example of a matrix includes nickel, aluminum, titanium, magnesium, ceramics and polymers. The reinforcement materials are stronger than the matrix materials, possess distinct properties, and are usually imbedded in a matrix material. The reinforcement includes whiskers, carbon fibers, silicon fibers and particulates (Chawla, 2006).

2.3 COMPOSITES

Composite is a material that comprises of two or more physically or chemically unique phases, usually a matrix material and reinforcement materials. Their properties are completely different from their constituent, which include toughness, wear resistance, thermal conductivity, electrical conductivity etc. The characteristic of a good composite is determined by the matrix, reinforcement and the interface, shape and distribution of the constituents (Kumar & Anandaheerthan, 2008).

2.3.1 Composites based on matrix

- Polymer Matrix Composites (PMC): PMCs are made up of a thermoset or thermoplastic (matrix) with carbon, steel and glass as the reinforcing material.
- Ceramic Matrix Composites (CMC): CMCs are made up of ceramic as the matrix, embedded with fibers of other ceramic material (reinforcement).
- Metal Matrix Composites (MMC): MMCs comprises of titanium, nickel, magnesium etc. as the metallic matrix and a reinforcing material like oxides, carbides or metallic phase (Kumar & Anandaheerthan, 2008).

2.3.2 Types of metal matrix composites

1. Titanium matrix composite (TMC): TMCs are composed of titanium and its alloys (matrix) with oxides, carbides or metallic phase as reinforcing phase. Titanium and its alloys are widely utilized in aerospace and automotive industries due to their good properties. The development of the TMCs has increased the performance of titanium and its alloy especially in aerospace industries. TMCs based (titanium aluminides) could provide a potential 50% weight savings as compared to nickel based super alloys in high temperature compressor applications (Singerman *et al.*, 1996; Hayat *et al.*, 2019)
2. Aluminum matrix composite (AMC): AMCs are made up of aluminum and its alloys (matrix) with oxides, carbides or metallic phase as reinforcing material. Alumina reinforced AMCs have found its application next to silicon carbide and carbon reinforced composites in aerospace and automotive industries. It was reported that Al-Al_2O_3 metal matrix composites possesses elevated temperature strength, good electrical conductivity and coefficient of thermal expansion (Rajan *et al.*, 1998)
3. Magnesium matrix composite (MMC): MMCs are made up of magnesium and its alloy reinforced with oxides, metallic phase or carbides. Magnesium and its alloys are used as energy conversion due to their low density (two-third of Al) and high strength. They are widely utilized aerospace and automotive for fuel consumption and reduction of green house emission (Mordike & Ebert, 2001; Habibnejad-Korayem *et al.*, 2009). The application of magnesium is restricted as a result of low wear resistance and poor creep resistance. Moreover, the development of MMCs has resulted in enhanced properties such as high elastic modulus, high wear resistance and creep at high temperature. MMCs showed better improvement as compared to monolithic magnesium (Dey & Pandey, 2015).

4. Nickel matrix composite (NMC): NMCs are composed of nickel and its alloys (matrix) with oxides, carbides or metallic phase as reinforcing phase. NiAl-matrix composites were fabricated via reactive sintering, and were reinforced with oxide, silicide and carbides. It was reported that the addition of reinforcement could increase the strength, hardness, and elastic modulus of the composites. Also, the increase in wear resistance and chemical compatibility may be achieved by aluminium oxide fibers (Novák *et al.*, 2011).

2.3.3 Metal matrix reinforcement

Several reinforcing materials have been used to achieve better mechanical properties of a composite. The particle size and type of reinforcement, the stability of the reinforcement in a specified working temperature should be considered during the selection of materials (Dey & Pandey, 2015). The most widely used reinforcements are listed below:

1. Silicon carbide (SiC): SiC particles are among the most widely recognized reinforcing material for aluminium matrix composites. They are known to be brittle and hard ceramic particles consisting of high modulus of elasticity, high strength and high electrical resistance. SiC is used to increases the yield strength, hardness, ultimate tensile strength and wear properties of magnesium and its alloys (Wong & Gupta, 2007). SiC particle distribution improves the properties of magnesium matrix composites through intensive shearing.
2. Alumina (Al_2O_3): Composites reinforced with Al_2O_3 are extensively utilized in tribological applications where wear rate and coefficient of friction are necessary. The reinforcement of alumina produces good compressive strength, excellent wear resistance and creep resistance. Creep strengthening materialize as a result of the load transfer between the plastic flow in the matrix and reinforcement (Pekguleryuz & Celikin, 2010)

3. Titanium carbide (TiC): This particle is used in coating applications in order to enhance wear resistance, high temperature stability and friction properties of the composites for diverse engineering applications. They play a significant role on damping behaviour of magnesium composites (Dey & Pandey, 2015). TiC can impart high toughness; yield strength, elastic modulus in a composite.
4. Boron carbide (B_4C): B_4C is a refractory material for structural and electronic applications because of its high temperature stability and thermoelectric properties. B_4C belongs to the family of ceramic materials that are frequently utilized in composite reinforcement. The particles are known for high hardness and they are applied where hardness requirement is of necessity.
5. Carbon nanotube (CNT): CNTs are ideal reinforcing material because of their high aspect ratios and high strength. The reinforcement of CNTs improves the wettability, bonding strength and tensile strength of metal matrix composites.

2.4 NICKEL ALUMINIDE METAL MATRIX

The early investigations of nickel aluminide (NiAl) as high temperature refractory material was reported by (Wachtell, 1952). In 1960s, there were more studies that focused on the processing and other metallurgical variables on the mechanical behaviour of NiAl (Wood *et al.*, 1964), and this intermetallic compound was recognized as a promising leading-edge material for a superalloy turbine vane in the mid-1960s. At this period, the challenges of low fracture toughness were noticeable and the interest in NiAl faded away by the end of 1960s. Efforts were made to study the mechanical and oxidation behaviour of NiAl between 1970s till mid-1980s. Towards the end of 1980s, investigations on NiAl gained wide attraction in the science communities (Noebe *et al.*, 1996). In spite of this, the mechanical attributes of NiAl are still restricted due to low fracture

toughness and ductility at room temperature (Geist et al., 2015). Recent investigations have been initiated in improving the mechanical properties of NiAl through microstructural control, addition of alloying elements and processing techniques. NiAl has complex atomic arrangements with AB, AB2, and AB3 (i.e A represents the lattice arrangement of an atom and B represents the lattice arrangement of another atom) types of stoichiometry. The crystal structures of NiAl may be achievable as a result of their covalent bonding, relative atom sizes, and atom ratio (Figure 2.1). It consists of ordered BCC (body-centered cubic) structure and the phase is established below ~400 °C at the range of ~ 45– 60 at. % of Ni. It consists of a Strukturbericht-superstructure designation of B2 having ordered crystal structure of simple CsCl prototype. The stoichiometry composition of NiAl are formed by Ni (0,0,0) and Al (1/2,1/2,1/2) in the body centered position consisting of α and β sub-lattices (Talaş, 2018), as shown in Figure 2.1. NiAl has a lattice constant of 2.887 Å (Foiles & Daw, 2011); the ratio of the valance electron density to atoms (in their stoichiometric compound) is 3:2, which is in agreement with Hume-Rothery (Makino, 1998). The stable β phase influences the properties of NiAl. The phase diagram of Ni–Al has three peritectic and two eutectic sections, alongside intermetallic regions of distinct compositions (NiAl3, Ni3Al, and NiAl) as shown in Figure 2.2. The phase diagram of NiAl was plotted by (Robertson & Wayman, 1984) and the new version by (Okamoto, 2004) as shown in Figure 2.2. NiAl intermetallic is thermodynamically steady owing to large negative formation of heat as compared to other intermetallic phases. The stability of the intermetallic phases within a range of temperature determines the utilization of the intermetallic material. Furthermore, NiAl possesses the followings: high melting temperature (1639 ^{o}C), which is bigger than nickel super alloys by 299 ^{o}C, low density of 5.95 g /cm^{3} (about two third of nickel super alloys), oxidation resistance and

good corrosion, lower ductile to brittle transition temperature, and thermal conductivity (between four to eight times) of nickel super alloys (Darolia, 1991).

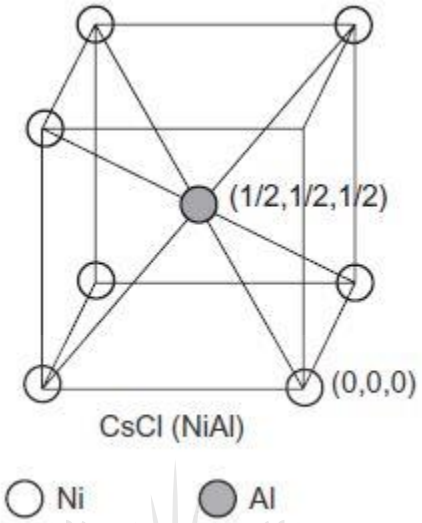

Figure 2.1. Crystal structure of NiAl (Talaş, 2018)

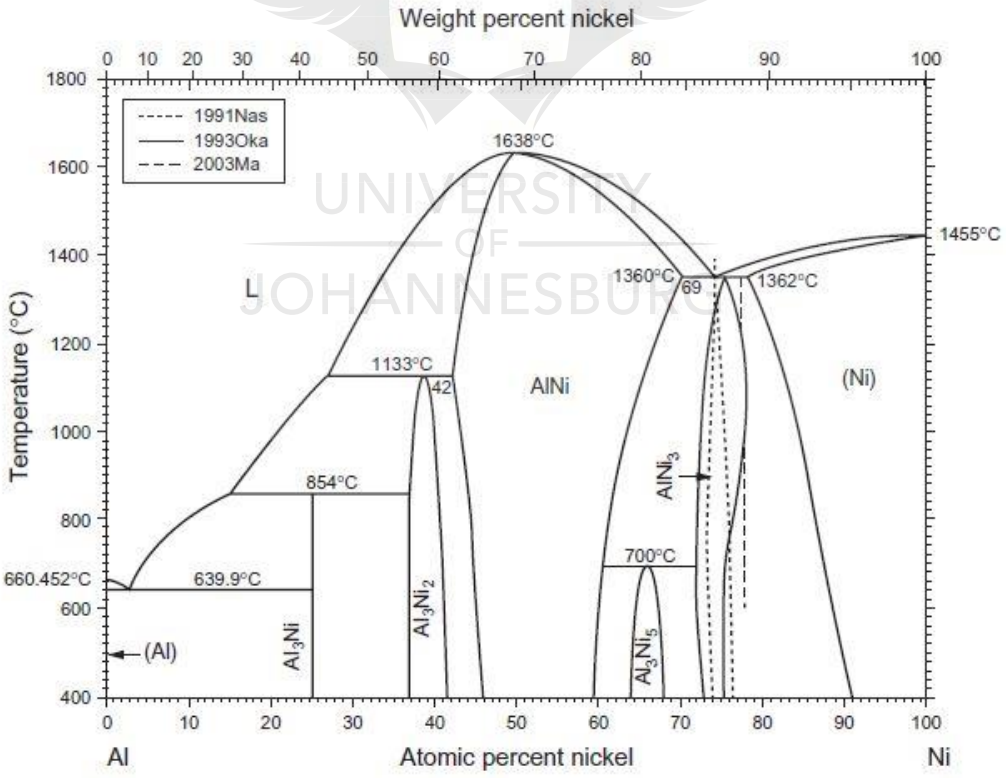

Figure 2.2. Phase plot of Ni-Al (Okamoto, 2004)

NiAl intermetallics find their applications as vane of aircraft and turbine blades because of their density. This compound (NiAl) was found to reduce the weight of turbine rotor by 40% (Darolia, 1991). Similarly, it is used as heat exchangers, jet engine hardware, combustion engines for non-structural application (Schilke & Schenectady, 2004; Frommeyer & Rablbauer, 2008).

The main slip system exhibited by NiAl at ambient temperature is the < 100 > (110) system (Cahn, 1991; Field *et al.,* 1991; Dollar *et al.,* 1992). NiAl has three independent slip systems; it does not possess the five independent slip systems required for polycrystalline deformation. Studies have illustrated that < 001 > dislocations are dominant inside the NiAl polycrystalline. Also, some observations revealed that the numbers are limited and the effect of dislocation on the properties of NiAl is not visible (Noebe, 1994). NiAl exhibits two types of behaviour; soft and hard orientations. Soft orientation crystal has a non < 100 > growth orientation and the slip systems in the soft orientation are < 001 > (110) and < 001 > (100). In the case of hard orientation, the result is independent of temperature (Loretto & Wasilewski, 1971; Bowman *et al.,* 1989), and the slip system is (011). In addition, the stress required for deformation is considerably higher in hard orientation as compared with the soft orientation because the resolved shear stress advanced toward zero during deformation (Wasilewski *et al.,* 1967; Bowman *et al.,* 1989).

2.4.1 Challenges of NiAl

Single crystal and polycrystalline NiAl are ductile at elevated temperature and brittle at room temperature. The (DBTT) ductile to brittle transition temperature ranges from 349 ^{o}C to 399 ^{o}C in oriented single crystals and 199 ^{o}C in oriented crystals (Darolia, 1991). The NiAl polycrystalline has been studied, and it depicts a (0–2%) tensile ductility at room temperature (Vedula *et al.,* 1988). The impurity content, texture, content of aluminum, and grain size (Schulson & Barker, 1983) influences the ductility of this intermetallic compound (NiAl). Also, the fracture toughness

is anisotropic which decreased from 8 MPa (m) $^{1/2}$ to 4 MPa (m)$^{1/2}$ in orientation (Sauthoff, 1989). The ductility of NiAl have been improved with the addition of Boron, but sufficient improvement have not been recorded (George & Liu, 1990). This transforms the fracture mode from brittle to ductile fracture surfaces mostly in Ni_3Al. Various methods have been used to enhance the fracture toughness and ductility of NiAl, such as fine-grain toughening, slip modification method, ductile phase toughening, mechanical alloying, heat treatment, and martensitic phase transformation toughening (Field *et al.*, 1991; Bochenek & Basista, 2015). Among these methods, grain refinement approach was used to enhance ductility by reducing the crystallite size of NiAl to nanometer scale, this allow the brittle material to transform into ductile material (Liu *et al.*, 2014). Nevertheless, carbon nanotubes (CNTs) can be used in enhancing the mechanical characteristics of NiAl. Studies by Ameri *et al.*, (2016), reported an increase in the fracture toughness of the mechanical alloyed NiAl-CNTs composites by 6.4% with the addition of 0.5% CNTs.

2.5 STRUCTURE OF CARBON NANOTUBES

Carbon nanotubes is a graphite sheet rolled in a tube with the caps of an hemisphere at both ends (Thostenson *et al.*, 2001). CNTs is different from diamond which has a three-dimensional diamond cubic crystal structure, each carbon atom has four neighbours that are organized in a tetrahedron. Likewise, graphite has a two-dimensional sheet of carbon atoms structured hexagonally, with each carbon atom connected to three closest neighbours (Harris, 1999). They are either single-walled (SWCNT) or multi-walled (MWCNT) nanotubes. SWCNT has a wrap of graphite sheet whereas MWCNT has many wraps of graphite sheets (Belin & Epron, 2005). Their features may be ascribed to rolled graphite sheet, the diameter of nanotubes, the length and structure of the nanotubes. MWCNTs (diameter between 5-40 nm) are known with their outstanding mechanical attributes. Some of these attributes include high modulus at 1.2 TPa

(comparable to diamond and 100 times higher than steel (Siegel *et al.,* 2001), excellent thermal and electrical characteristics. SWCNT has superior attributes as compared with MWCNT, although MWCNT is relatively simple in terms of preparation and economical for most applications. SWCNT consists of chiral angle (ɵ) and vector ($\bar{C}_h$), this indicates the level of twist in the nanotube. The chiral vector is presented below;

$\bar{C}_h = u\bar{a}_1 + v\bar{a}_2$ ..... Equation 2.1

u and v are integers while $\bar{a}_1$ and $\bar{a}_2$ depicts the unit vectors in two-dimensional grapheme sheet (Saito *et al.*, 1992; Bethune *et al.*, 1993). Due to the chiral angle and integers (u, v) of nanotubes, it exists as armchair, chiral, and ziz-zag nanotubes (Poole Jr & Owens, 2003).

- Armchair nanotube: It exists when chiral angle is at 30^o.
- Ziz-zag nanotube: This exists when the chiral angle (ɵ) is at zero degree.
- Chiral nanotube: It influences the number of twist in a tube (Terrones, 2003).

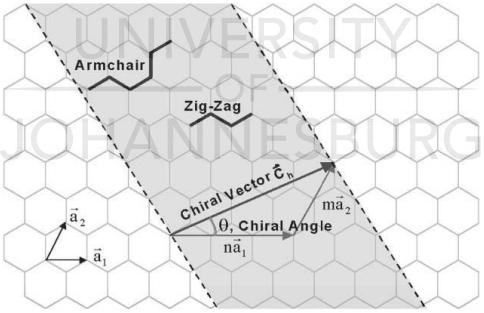

Figure 2.3. Illustration of a hexagonal rolled sheet of graphite forming CNT*(*Thostenson *et al.,* 2001)

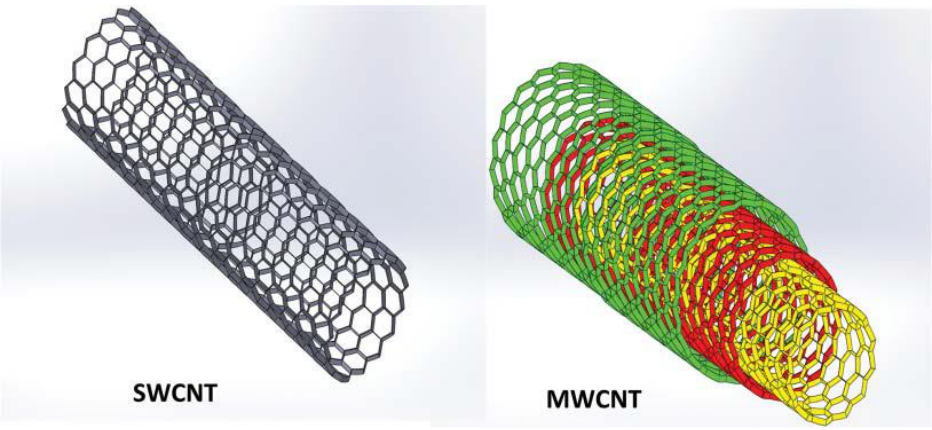

Figure 2.4. Structures of single-walled and multi-walled nanotubes (K. S. Munir & Wen, 2016)

2.6 FEATURES OF CARBON NANOTUBES

CNTs is used in enhancing metal matrices due to their outstanding characteristics like, electrical properties, high thermal conductivity, good mechanical properties, and excellent wear properties. CNTs possesses a high thermal conductivity (Shi *et al.*, 2007), and a very low thermal expansion coefficient. Deng *et al.* (2008) reported a 12% decrease in the thermal expansion coefficient of CNTs-Al composite which was attributed to the substantial surface area of the nanotubes. Also, the thermal expansion of Ni-CNTs composite showed an increment. Owing to the good bonding within the CNTs and the matrix, a 200% increment in thermal conductivity was achieved using the electro-deposition technique. Shi *et al.* (2007) investigated the reinforcement of 4 wt% CNTs with W-Cu composite, in which the thermal conductivity increased by 27.8%. However, good interfacial bonding between matrices and CNTs can be used in enhancing better thermal properties. The reinforcement of CNTs with metallic matrices have enormously improved the electrical properties of the composites. Yang *et al.* (2008) observed that the electrical resistivity of SWCNTs reinforced Cu composites are similar with copper. Similarly, a 66% increment in electrical resistivity was observed for the fabricated Al-12.5% Vol. CNTs composites (Xu *et al.*, 1999). Feng *et al.* (2005) reported a marginal increase in electrical resistivity with the studies on Ag-CNT.

An increment was observed in the electrical property of CNTs (beyond 10 Vol%) owing to the increment in strain and interfacial area of the metallic matrix due to CNTs agglomeration.

The wear properties of the composite coatings (Ni-CNT) were studied using electro-deposition method, the coefficient of friction (COF) decreased and wear resistance increased due to the lubricating nature of CNTs which resulted in easy sliding of their walls (Chen *et al.,* 2001; Chen *et al.,* 2003). Chen *et al.* (2003) worked on the powder metallurgy of Cu-CNT composite by using a nickel coated CNT and they attained a great enhancement in the wear properties of the composite. Studies depicts a 140% decrease in wear rate and a 91% decrease in COF because of the CNT contents (16 Vol%). The wear properties of Al- 20% Vol. CNTs composite was studied, indicating a 22% decrease in COF and 25% reduction in the wear rate (Zhou *et al.,* 2007).

CNT shows exceptional mechanical attributes because of the C-C bond present in them (Salvetat *et al.,* 1999). They have good tensile strength and Young's modulus more than the diamond due to the σ bonding that occurred in the carbon atoms (Meyyappan, 2005). The modulus of elasticity of carbon nanotubes rely on their diameter. Thus, SWCNTs possesses a high modulus of elasticity of 100 000 000 Pa owing to their diameter that extends from 1 to 2 nm (Dresselhaus *et al.,* 1995; Salvetat *et al.,* 1999; Meyyappan, 2005). Delaney *et al.* (1998) reported that the Young's modulus of CNTs decreases from 1TPa to 100GPa upon the increase in diameter (3 nm to 20 nm) of SWCNT bundle. MWCNTs are observed with higher elastic modulus as a result of their various nanotube diameters and the Van der Waals forces in the tubes (Meyyappan, 2005). CNTs are able to endure great strains in tension before fracture (Yakobson & Avouris, 2001) than materials that fails with a strain less than 1% because of defects propagation . It leads to the sp^2 C-C networks, which re-hybridize when the CNTs are bent (Dresselhaus *et al.,* 1995). MWCNTs

has the tensile strength of about 50 GPa (Yu *et al.,* 2000) which are 20 times stronger than steel (Dresselhaus *et al.,* 1995).

2.7 SYNTHESIS OF CARBON NANOTUBES

This is a technique employed in producing carbon nanotubes in sizable quantities, these includes chemical vapour deposition, laser ablation and electric arc discharge methods.

2.7.1 Chemical vapour deposition

This method synthesizes lengthy CNTs with excellent morphology. It enables the production of CNTs with good mechanical attributes. This is a process where hydrocarbons are heated at high temperature between 973 K to 1273 K through a catalytic system in a quartz tube. CNTs are synthesized by thermal decomposition of carbon (with gas molecules) on catalytic systems. The carbon atoms disperse on the metallic surface at elevated temperature when the hydrocarbon breaks into carbon and hydrogen. This results into carbon (hexagonal shape) before CNTs is obtained. Nevertheless, growth of CNTs can be aborted once the carbon atoms does not have contact with the metal catalyst. The hydrocarbons used in CVD are in form of solid, liquid, and gaseous states (Kong *et al.,* 1998; Ren *et al.,* 1998). Also, synthesis of Si/CNT used in Li-ion battery anode was conducted using the CVD method (Kim *et al.,* 2006; Shu *et al.,* 2006), with Ni as catalyst. The formation of CNT clusters was observed on the Si particles, with voids in the composite. The voids are utilized in accommodating structural changes in Si particles through the battery cycles without generating structural stress. The fabrication of CNTs-Si coated composites by silane decomposition to increase the thermal stability of CNTs was observed by Wang *et al.* (2006). Studies by Koziol *et al.* (2005) revealed the use of nitrogen precursors in synthesizing CNTs through the CVD. Diazine (hydrocarbon feed stock) was used to synthesize MWCNTs by placing it in a reactor at a temperature of 760 ^{o}C. The MWCNTs were observed with excellent

amount of internal order and the electron diffraction patterns suggested that the walls had similar chiral angle that were not seen in concentric cylindrical CNTs due to geometrical constrain, although it existed in conical CNTs. The diffraction patterns depicted a plain achiral form when the angles of chiral was observed. The CNTs indicates an armchair or Zigzag (Figure 2.4), with conical angle between 0.5^{o} and 5^{o}. Furthermore, the lattice depicts the presence of nitrogen and N_2 gas was observed in the tube, for instance in the core (Friedrichs *et al.*, 2005; Ducati *et al.*, 2006). The shallow cones observed was as a result of high diazine concentrations.

Figure 2.5. MWCNTs diffraction patterns: From the Left to Right, chirality, armchair and zig-zag (Koziol *et al.*, 2005).

2.7.2 Electric arc discharge technique

This method is used to synthesize CNTs consisting a structural flawlessness (Li *et al.*, 2004). It is among the earliest method which utilizes graphite electrodes in synthesizing CNTs (Bethune *et al.*, 1993; Iijima & Ichihashi, 1993; Journet *et al.*, 1997), in a chamber with an inert gas (Poole Jr & Owens, 2003; Meyyappan, 2005). Direct current (50-100A) flows from the graphite electrodes which leads to carbon atoms deposition at the cathode (negative electrode) and carbon atoms discharge at the anode (positive electrode). CNTs initiates at the cathode owing to the reduction in anode length (Wilson *et al.*, 2002). At the anode, crystallites are produced which leads to the carbon agglomeration in form of MWCNTs. Also, as a result of undesirable crystallites which fail

to form nanotubes can restrict the synthesis of substantial yields (Gamaly & Ebbesen, 1995; Ajayan & Ebbesen, 1997). This method is used to produce SWCNTs using Ni or Fe as metallic catalyst, but MWCNTs synthesis may not require a metallic catalyst (ChhowallaM & Amaratunga, 2001). The synthesis of MWCNTs in a liquid environment was studied using electric discharge technique between pure graphite electrodes (Antisari *et al.*, 2003). This was carried out with deionized water and liquid nitrogen. Liquid nitrogen provides the necessary environment in MWCNTs production, but the thermal exchange among the synthesized MWCNTs and its environment was hindered by the evaporation produced by electron arc discharge, therefore degrading MWCNTs structure. However, good quality of MWCNTs can be synthesized in deionized water, thereby providing a suitable atmosphere with thermal exchange because of the cooling ability of water than liquid nitrogen. Huang *et al. (*2011) reported a high quality of SWCNTs from Y-Ni alloy as catalyst and Se as a promoter. The purity of SWCNTs was attained with HNO_3 reflux and air oxidation (diameter of 1.5 nm). The process of utilizing Se as a promoter for producing SWCNTs depicted better syntheses than FeS as a promoter because of the wetting effect of Se, thereby promoting uniform diameter distribution (Figure 2.9(a-f)). Thus, with electrolysis, air oxidation and centrifugation processes, better purification of SWCNTs have been obtained with less damage.

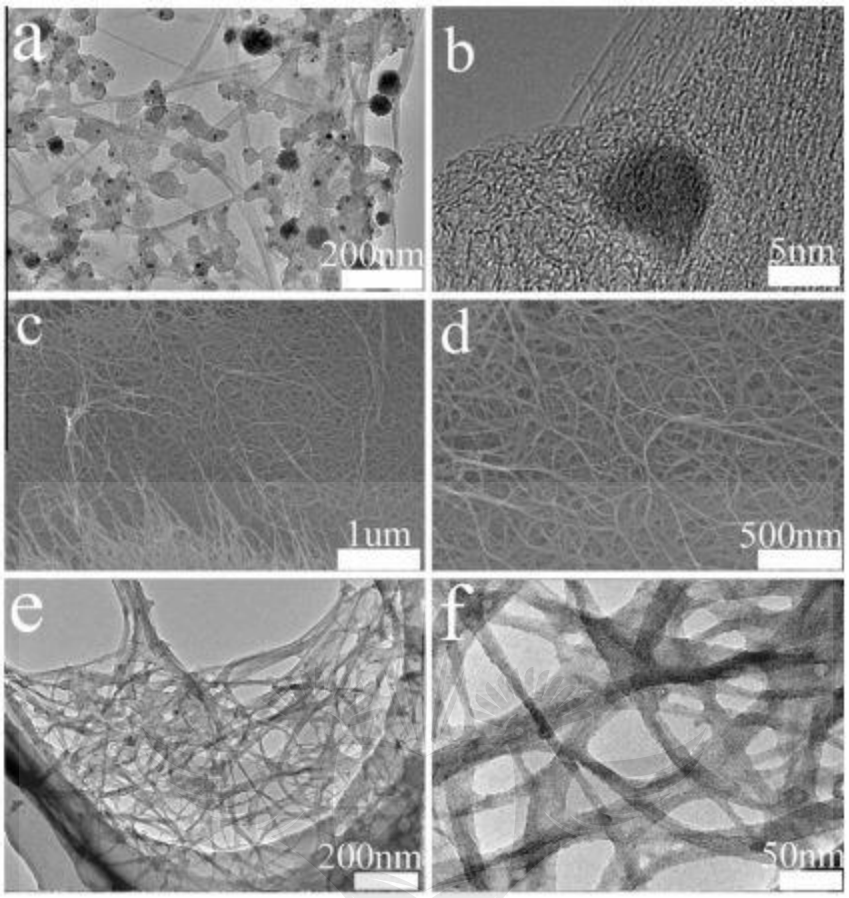

Figure 2.6. Images of web-like SWCNTs produced with Se as a promoter: (a-b)TEM micrographs of as-prepared specimen, (c-d) SEM micrographs of the purified specimen and (e-f) TEM micrographs of the purified specimen (Huang *et al.*, 2011)

2.7.3 Laser ablation method

This technique is used to fabricate SWCNTs (Thess et al., 1996; Rinzler et al., 1998; Zhang & Iijima, 1999). It involves the use of a laser which vaporizes a carbon target in an argon environment. This method was utilized in early production of fullerenes. It is conducted by subjecting the carbon target to a high temperature (1200 ^{o}C) in a furnace, the evaporation of carbon takes place (Terrones, 2003). The carbon atoms were charged by the inert gas at high temperature to a collector and CNTs are produced after cooling (Poole Jr & Owens, 2003). This technique was reportedly studied in 1955 by Smalley and his co-workers, and the synthesis of SWCNT and MWCNT were successfully achieved. The properties and structures of the CNTs depends on the

hydrocarbon used, the carrier gas and flow rate of the gases (Meyyappan, 2005). The disadvantage of this method is the cost owing to substantial power lasers (Terrones, 2003). The fabrication of SWCNTs with Co and Ni as catalyst was carried out in a nitrogen environment using laser ablation (Zhang *et al.* 1998). The transmission electron microscopy and electron loss spectroscope revealed a great yield of SWCNTs like the nanotubes produced with an inert gas. Similarly, the effect of laser wavelength on the synthesis of CNTs was investigated by Chrzanowska *et al.* (2015). The range of UV laser radiation was observed through the Raman spectroscopy and scanning electron microscope, but the attributes of the CNTs are dependent on the laser fluence. The illustration of the laser ablation is presented in Figure 2.10.

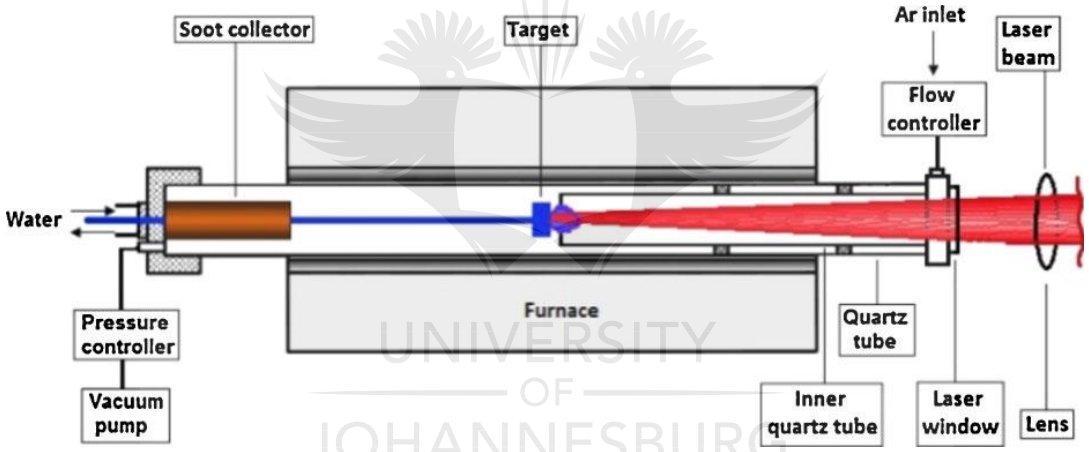

Figure 2.7 Illustration of laser ablation depicting the synthesis of carbon nanotubes (Chrzanowska *et al.*, 2015)

2.8 DISPERSION OF CARBON NANOTUBES WITHIN THE METAL MATRIX

Mechanical attributes of MMCs depends on the methods of dispersing nanotubes in metal matrices, different means of consolidating the composites, morphology of the starting materials, interfacial reactions between reinforcement and matrix, and percentage weight of CNTs utilized (Desai & Haque, 2005; Reihanian *et al.*, 2009). CNTs are used to enhance metal matrices because of their excellent properties, although they are very difficult to disperse in metallic matrices

because of the Van der Waals force found in them (Kondoh *et al.*, 2009; Zeng *et al.*, 2010). They may lose their structural integrity during harsh processing conditions; therefore, several processing methods have been developed to minimize CNTs damages during fabrication.

2.8.1 Electrodeposition method

This method entails the deposition of film on a material by using the electrochemical cells, it is facilitated through the current flow between the anode and cathode. Electrodeposition technique is utilized in incorporating CNTs-Ni /Cu composites (Ferrer-Anglada *et al.*, 2006; Shi *et al.*, 2004; Liu *et al.*, 2013), and this method suggests great benefit over spray and sputtering techniques because it is cost effective (Chen *et al.*, 2002). It is widely studied due to its good wear resistance and distribution strengthening (Changrong *et al.*, 2001; Choa *et al.*, 2003). Chen *et al.* (2001) reported that the content of CNT increased with bath rate agitation, current density, and with CNTs concentration in the electrolyte during electro-deposition of 14% CNT-Ni. This was done at a concentration of 2 g L^{-1} and with the current density of 15 A dm^{-2}. Cho *et al.* (2006) used the electrodeposition method in producing CNT field emission structure, where SWCNT depicts a good bonding with the substrate during their dispersion in Ni matrix. SWCNT and Ni serves as the emitter structure. Studies by Arai *et al.* (2004) on the electrodeposition of CNT-Cu and CNT-Ni revealed a uniform CNTs dispersion with the addition of polyacrylic acid to the basic bath through stirring. The deposited CNTs on Ni film produced a skewered dumpling structure. Ni depicts non-uniform deposition on the CNTs, though it was electrodeposited on the outer surface of CNTs (indicated in Figure 2.8(a)). Guo *et al.* (2007) reported an increase in reverse ratio and pulse frequency of Ni-CNT coating as a result of the increase in the CNTs content which resulted in a smooth surface. The electrodeposition of Ni-CNTs with the current density (40 mA/cm^2) revealed the dispersion of CNTs in the composite, as a result of etchant (Nitric acid). The

Increment in CNTs concentration led to a better dispersion of the Ni-CNTs composite (Sung-Kyu & Tae-Sung, 2011), indicated in Figure 2.9(a-d).

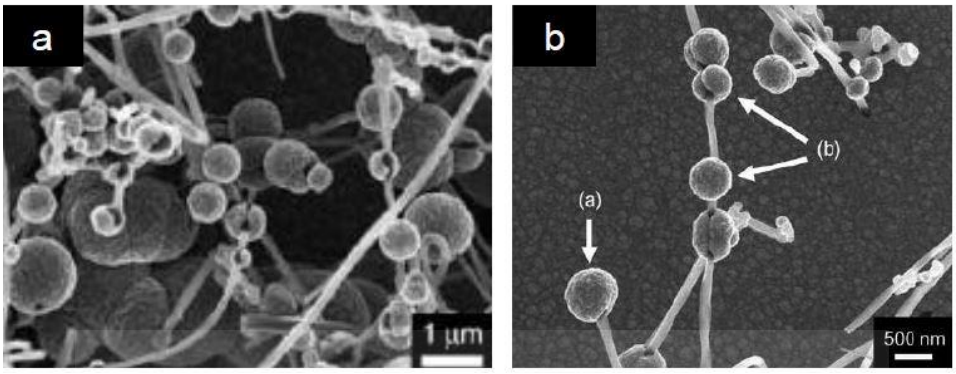

Figure 2.8. Skewered micrograph of Ni-CNTs composite (Arai *et al.*, 2004)

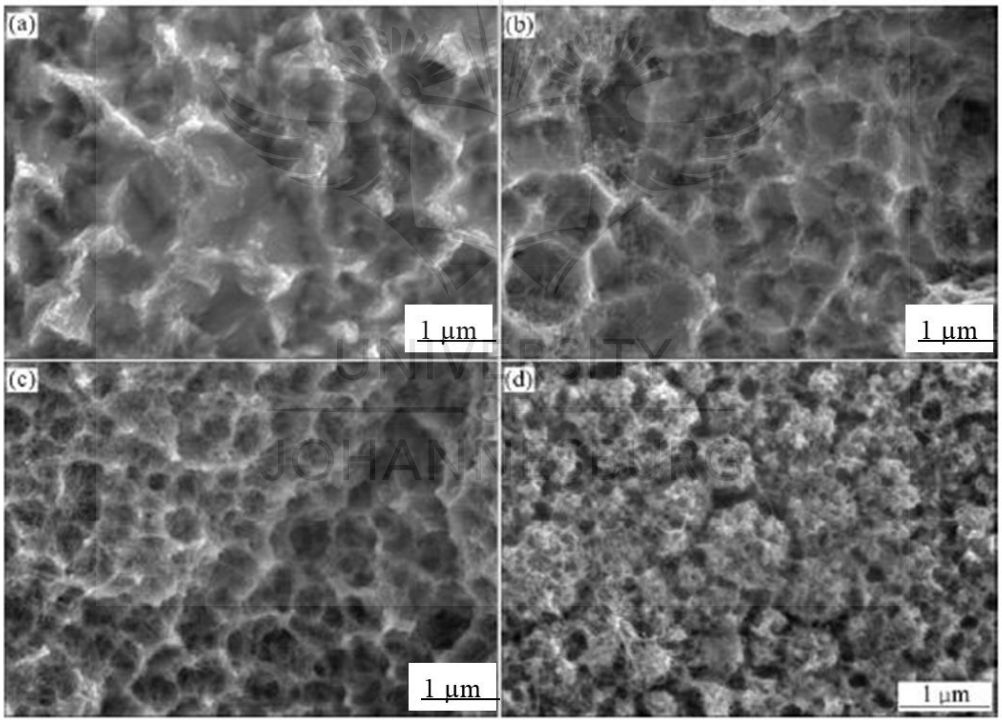

Figure 2.9. FESEM micrographs depicting Ni-CNTs nano-composites electrodeposition : (a)1 g/L, (b) 2 g/L, (c) 5 g/L, and (d) 10 g/L (Sung-Kyu & Tae-Sung, 2011).

2.8.2 Ultrasonication method

This process is used to unbundle nanotubes through the application of ultrasonic bath (Rosca *et al.*, 2005; Yu *et al.*, 2007; Montazeri *et al.*, 2011). It is very effective in dispersing nanotubes in

a high or low concentration of liquid. CNTs are unbundled with the help of shock waves derived in the sonicator, and it has been largely utilized by researchers to disperse CNTs in polymers and metals through the help of surfactants (Kim *et al.,* 2006; White *et al.,* 2007; Rastogi *et al.,*2008; Wang *et al.,* 2008; Duque *et al.,* 2010). During this process, shock waves are produced from high sonication energy which causes defects. Therefore, sonicator parameters are regulated to prevent unenviable phases. Likewise, long sonication time may shorten CNTs, thereby reducing their aspect ratios and finally affects their load abilities (Shelimov *et al.,* 1998; Kang *et al.,* 2006; Yu *et al.,* 2007). Other challenges accompanied by ultrasonication include the formation of cavitation bubbles in the sonicated medium due to compression and expansions waves (Lucas *et al.,* 2009). Mukhopadhyay *et al.* (2002) investigated that long sonication time of CNTs resulted in non-crystalline carbon nanoparticles after the graphene layers had been damaged (Figure 2.10(a-d). Furthermore, Munir *et al.* (2015) reported a uniform dispersion of CNTs, a 89% raise in Young's modulus, and 192% increment in the nano hardness of the sonicated assisted ball milled Ti-MWCNTs composite when compared with the ball milled composites. This investigation revealed that sonication assisted ball milling method could preserve the structural integrity of the nanotube.

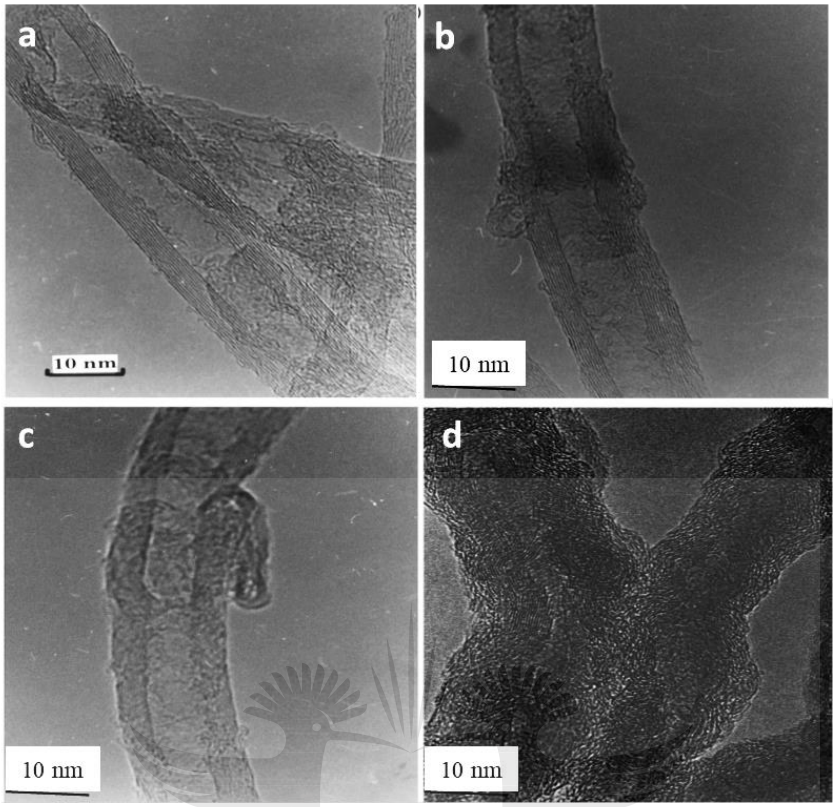

Figure 2.10. HREM images of CNTs: (a) unsonicated layers of graphene on each side, (b) sonicated layers of graphene was changed into amorphous layers after 4 hours, (c) sonicated layers of graphene transformed to amorphous layers after 8 hours, (d) sonicated layers of graphene transformed to carbon nanofiber after 24 hours (Mukhopadhyay *et al.,* 2002).

2.8.3 Ball milling process

Ball milling is another method of dispersing CNTs in metal matrices and it a process where powders are milled in a container (e.g. hardened steel vials) with different balls. During the ball milling technique, the matrix-powder undergoes fracturing and welding, which enables CNT entrapment between the matrix-powder (Morsi *et al.*, 2010; Yadav & Harimkar, 2011). Furthermore, CNTs/matrix powders are trapped between the milling container and the balls, and the interplay of the grinding motion de-bundles the CNTs in the matrix-powder. The role of milling time is also significant in ensuring better dispersion, as it proceeds then the agglomerations in CNTs are reduced. In the early period of the milling procedure, the matrix powder is spherical in

shape and the CNTs are dispersed at powder surface. Afterwards the matrix powder become soft and flattens, and the CNTs were embedded within the matrix powder (Morsi *et al.,* 2010). The benefits of using ball milling process includes; ease of processing powders, mass production of powders can be achieved, and it is cost effective. The challenges of using this process includes; production of defects in CNTs, shortening of CNTs, contamination and long processing time (Azarniya *et al.*, 2017). The utilization of PCA (process control agent) may enhance the dispersion of CNTs within the matrices. Notwithstanding, there are different ball milling equipment employed in dispersing the powders, the low energy ball milling exerts less energy on the powders while the high energy ball milling exerts substantial energy on the powders. The latter can embed CNTs in the matrix, while the former may not evenly disperse CNTs. This may not allow the effective diffusion of CNTs in the matrix. Therefore, adequate practical condition is necessary to attain high yield of the composites (Liao & Tan, 2011). The effect of low and high energy ball milling technique on the dispersion of CNTs in aluminum matrix was investigated by (Liao & Tan, 2011). They reported that Al-0.5 wt% CNT composite powders were milled using the high energy ball milling 200 rpm for 4 hours. PCA was used in the milling to avoid cold welding of powders and the ball to powder ratio was set as 5:1. The composite powders were milled with low energy ball milling with similar condition. They observed CNTs embedment (depicted by yellow arrows) within the Al matrix through diffusion process due to the impact of high energy ball milling. Better dispersion of CNTs was achieved with no agglomeration, while in the low energy ball milling, some CNTs agglomerate were observed among the Al matrix powder. Also, some CNTs separates and embeds within the matrix powder and most Al powders still shows their round shape, rather than flake that was observed in the high energy ball milling. The SEM micrographs of the milling processes were observed (Figure 2.11).

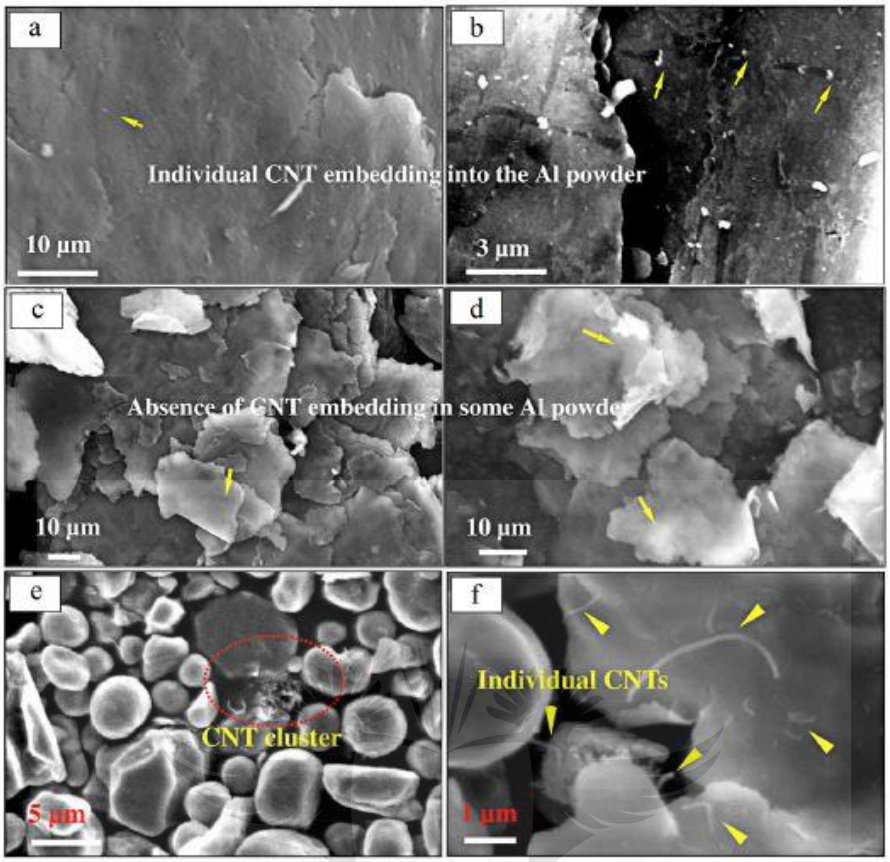

Figure 2.11. SEM micrographs of Al-CNT powder: (a–d) after milling by high energy ball milling and (e-f) low energy ball milling (Reproduced by (Azarniya *et al.*, 2017).

Esawi & Morsi, (2007) investigated the dispersion of CNTs in Al matrix powder using the high energy ball milling. In this study, the effect of milling time and the dispersion of CNTs on the microstructures of the composite powders was studied. Al-2wt% CNT powders were milled using the high energy ball milling at the speed of 200 rpm for varied milling times (30 min, 1 h, 3 h, 6 h, 12 h, 18 h, 24 h, 36 h, and 48 h). Mechanical alloying involves two competing processes; cold welding of particles which resulted in decreasing ductility and fracturing of particles. The other process entails the cold welding of the particles which increases the particle size (Suryanarayana, 2001). They reported that Al particles were flattened, formed flakes and then welded together to form large particles. The surface became smoother after continuous milling. CNTs was homogeneously dispersed on the flakes' surface after 30 min of ball milling. It was also dispersed

after the ball milling was increased from 1 h to 3 h. Then after 6 h of ball milling, the particles had cold welded with CNTs embedded in the particles, thereby forming large smooth particles. The effect of the ball milling on the microstructures of the composites are presented in Figure 2.12.

The effect of ball milling time on the mechanical properties of Al-CNT composites was studied by Liu *et al.* (2012). Al-CNT powders were milled using the high energy ball milling at a speed of 300 rpm for the durations of 2 h, 4 h, 6 h, 8 h and 12 h. They reported that the powders were flattened as the milling time increased from 2 h to 8 h due to the shearing effect of the milling balls. Further increase in the milling time to 12 h resulted in the fracturing of the powders. Clustered CNTs were observed at the surface of Al particles at the milling time of 2 h and the entangled CNTs decreases at 4 h. When the ball milling was increased from 6 h to 8 h, CNTs clusters disappeared, showing a gradual dispersion.

.

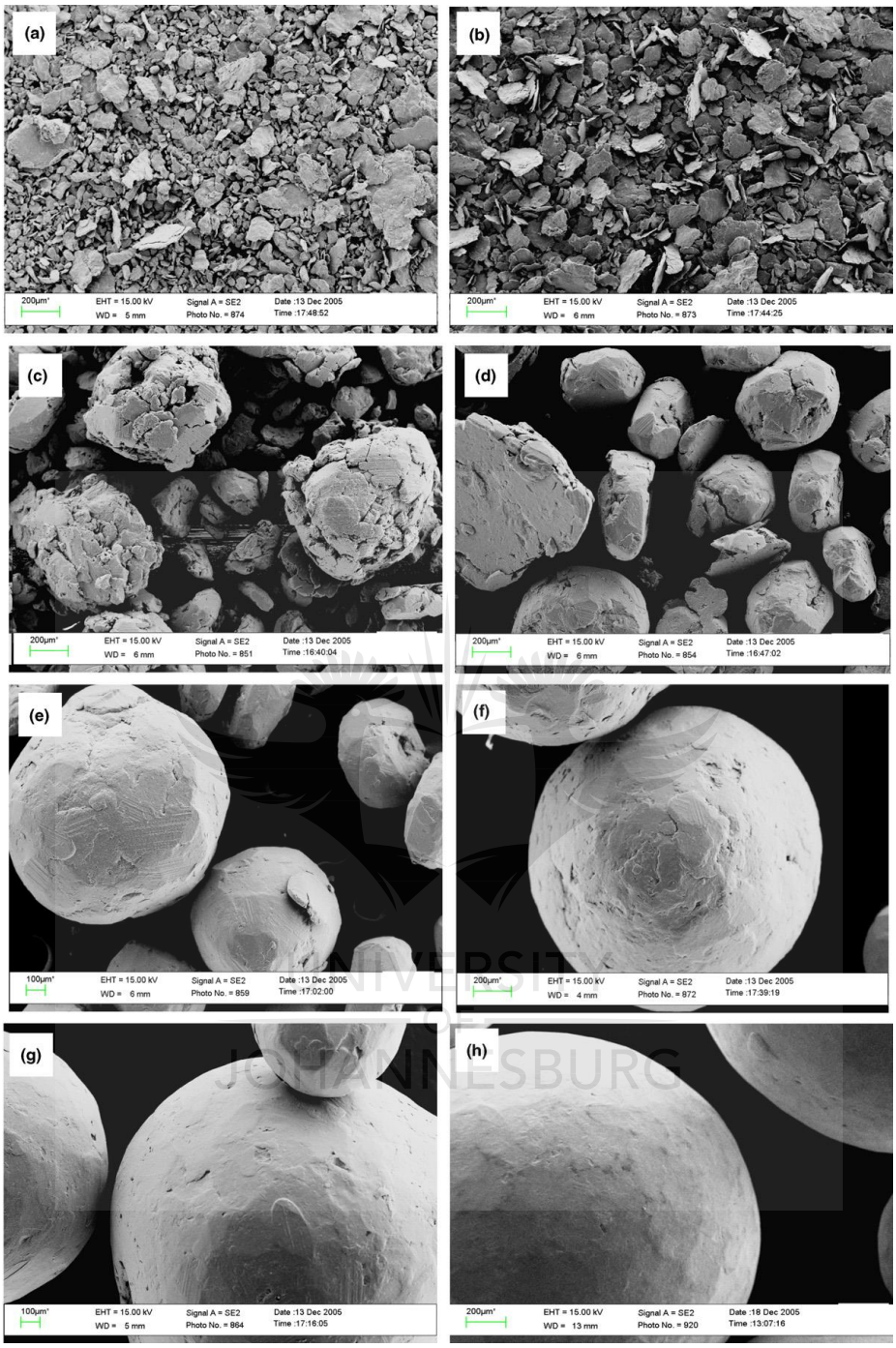

Figure 2.12. SEM images of mechanically alloyed Al-2 wt% CNT powder after (a) 0.5 h, (b) 1 h, (c) 3 h, (d) 6 h, (e) 12 h, (f) 18 h, (g) 36 h and (h) 48 h (Esawi & Morsi, 2007).

The strength of the unreinforced Al matrix increased, and the elongation decreased with the milling time, and zero elongation was recorded for the ball milled composites at 12 h as a result of alumina

and iron impurities. The ultimate tensile strength and yield strength of the composites increased with the milling time (about 18.4% and 42.3% increments) and the elongation increased from 4-6 h and it further decreased from 8 h, as shown in Figure 2.13.

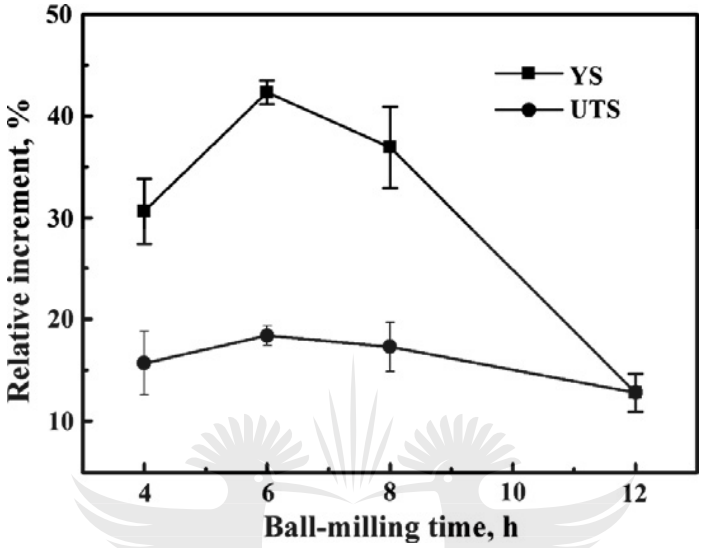

Figure 2.13. Relative increments of UTS and YS of Al-CNT composites relative to Al matrix (Liu *et al.*, 2012).

In a bit to ensure good dispersion of CNTs in metal matrices, some milling techniques have been developed by researchers, these techniques include:

- **Cryogenic milling**: This is another milling technique that is used to suppress heat-induced changes in metal powder. It is carried out at a low temperature below 174 ^{o}C, to reduce grain growth, promote grain refinement, increase brittleness and decrease grain size in metal particles. The method is associated with reduced processing time, and the increase in hardness of the nanocomposites are achieved through the Hall-Petch mechanism. Cryogenic milling was used to achieve the dispersion of CNTs in Al 2009 matrix under liquid nitrogen at the speed of 180 rpm for 2 h (He *et al.*, 2017). They observed the dispersion of CNTs in a short time, with little damage under cryogenic milling. Also, a

balance was attained between the high strength and yield strength (443.3 MPa) and elongation of 10.2%.

- **Two stage milling**: This technique entails the combination of the low energy ball milling and high energy ball milling process. Xu *et al.* (2017) utilized the two-stage milling to achieve the dispersion of 1.5 wt% CNT in Al matrix composites. The low energy was carried at the speed of 135 rpm for 8 h while the high energy ball milling was carried out at 270 rpm for 1 h. They reported an ultimate tensile strength of 376 MPa, a yield strength of 326 MPa and elongation of 12.4%. With this approach, a balance was achieved between ductility and strength with uniform dispersion of CNTs and little structural damage.
- **Dual matrix method**: This approach was investigated by Salama *et al.* (2017) to disperse CNTs within Al composites. A single matrix approach was used in dispersing CNTs in Al matrix powder via high planetary ball milling for 2 hours at the speed of 400 rpm. Afterwards dual matrix approach was achieved through the embedment of the single matrix powder in an auxiliary Al matrix at the duration of 0.5 h and 1 h. During this experiment, 1 wt% and 2.5 wt% CNT contents was used. They achieved a higher ductility with the auxiliary milling of the dual matrices as compared to single matrices due to good bonding between the two phases. The dual matrix approach gave the best mechanical properties with the tensile strength of 298.3 MPa and ductility of 11.6% for 1 wt% CNTs and 348.3 MPa and 7.2% (tensile strength and ductility) for 2.5 wt% CNTs respectively.

2.9 FABRICATION TECHNIQUES

2.9.1 Powder metallurgy

Powder metallurgy (PM) can fabricate complex materials which are not easily carried out by convectional casting technique. PM entails the mixtures of powder to produce bulk samples after

fabrication at a temperature lower than the melting point of the powder sample (Oghbaei & Mirzaee, 2010). It has been extensively used because of its excellent benefits which includes near-net shape production of parts, low cost of manufacturing and material loss (Long *et al.*, 2013). The mixture of the reinforcement and the matrix powder are achieved with the help of mechanical alloying, and the syntheses are carried out with hot pressing, spark plasma sintering, and microwave sintering (Obadele *et al.*, 2017). Mechanical alloying (MA) has been used in processing different powders and nano powder composites with fine microstructures by cold welding, fracturing, and re-welding of powder mixtures through high energy ball milling (HEBM). Due to the nano size and high-volume fraction of CNTs, they tend to agglomerate, therefore HEBM has been employed to debundle and disperse CNTs (Prabhu *et al.*, 2006). HEBM was used to produce oxide-dispersion strengthened Fe and Ni based alloys for aerospace applications (Benjamin, 1990). It was also used in producing crystalline and metastable intermetallics phases after undergoing repeated cold welding, fracturing, and re-welding due to ball collision (Suryanarayana, 2001). A plastic deformation of the powder takes place, steady and repeated equilibrium is attained through welding and fracturing of the powders (Benjamin & Volin, 1974). During MA, harsh ball milling may cause defects and bending stress in CNTs (Pierard *et al.*, 2001), without adequate control of the milling parameters such as milling duration, speed and interval, ball to powder ratio (BPR), and radius of sample holder (Agarwal *et al.*, 2016). The schematic diagram of the ball milling process is shown in Figure 2.14, the milling may undergo either wet or dry milling. The latter require no solvent during milling while the former utilizes solvent with low surface energy, for instance ethanol. Therefore, PM can be used in dry and wet states to achieve homogeneous dispersion (Nishida, 2013).

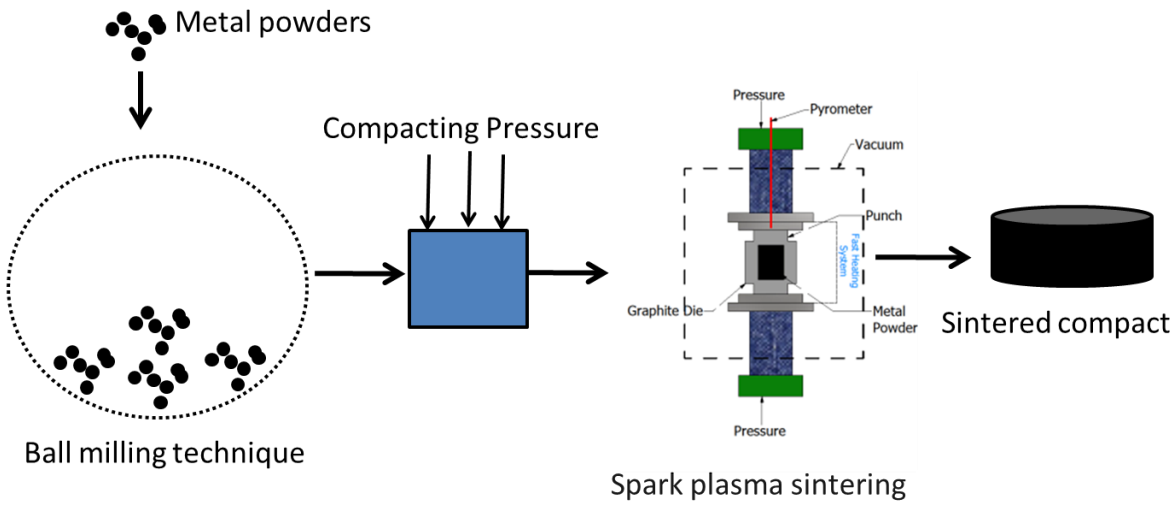

Figure 2.14. Diagram of powder metallurgy technique

2.9.2 Spark plasma sintering

Spark plasma sintering (SPS) involves the fabrication of powders using the pulsed current and force under the exertion of compressive pressure. The heating in SPS is achieved by spark discharges in voids between the powder particles, which refines and activates the powder surface. The refined surface of the particles melts and join to form a neck. Afterwards the direct current passes through the particles via the necks. The direct current produced the joule heating, and there is atomic diffusion in the necks, thereby resulting to their growth (Munir *et al.*, 2006). The role of high temperature reduces the grain coarsening. The material is heated and becomes soft, and thereby exerts plastic deformation under the force. The densification of the material is achieved through the combination effect of the plastic deformation and diffusion. With the use of SPS, nanocrystalline materials can be fabricated by suppressing the grain size as a result of rapid heating rate (Matizamhuka, 2016). This technique is an upgrade of the hot-pressing process (Kessel & Hennicke, 2007; Suárez *et al.*, 2013). In the hot-pressing process, the material is being heated indirectly through conduction or convection. Therefore, full densification is not attainable but SPS

can attain 100% densification without the use of binder (Kessel *et al.*, 2010; Rajeswari *et al.*, 2010, Khalil, 2012). It is associated with fast heating and cooling rates, short sintering time, high densification, preservation of the innate properties of fully dense powders, high energy efficiency, better refinement of powder surface and limitation of grain growth (Suárez *et al.*, 2013). Studies shows that SPS can prevent interfacial reactions by decreasing the consolidation time of CNTs reinforced metal matrix composites (Hulbert *et al.*, 2009). The sintering of nano powders can be achieved without providing necessary time for grain growth. The formation of plasma as a result of the direct current effect in SPS is still unclear (Matsugi, 1995; Chaim, 2007; Shen *et al.*, 2002). Figure 2.15 depicts the technique of SPS and flow of direct current in the particles.

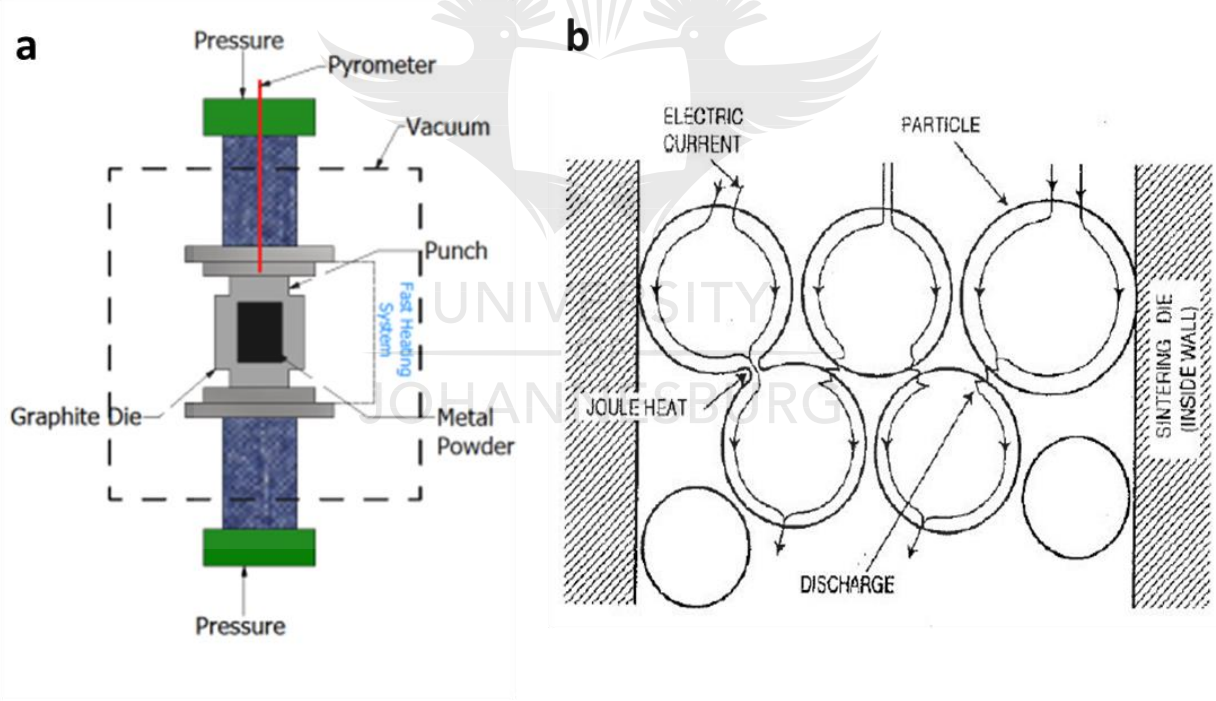

Figure 2.15. Illustration showing: (a) SPS, and (b) current passing through the powder particles (Suárez *et al.*, 2013).

2.9.3 Influence of sintering parameters

During the sintering process, different sintering parameters such as temperature, pressure, holding time, and heating rate contributes to the augmentation of the properties of CNTs reinforced metal

matrix. The influence of sintering temperatures was observed in the fabrication of CNT/AMCs. According to the reports from Guo *et al.* (2017), different CNTs weights (0.75 and 1%) and sintering temperatures (590 ^{o}C and 630 ^{o}C) were considered during the consolidation of the composites. The results revealed that the sintered composite (0.75 Wt% CNT) at 590 ^{o}C had the minimum mechanical properties which include tensile strength, yield strength and elongation. Irrespective of the CNT weights, the mechanical characteristics of the composites increased while the sintering temperature increased from 590 ^{o}C to 630 ^{o}C. This showed that sintering temperature can improve the properties of a sintered composite. During sintering process, sintering temperature may facilitate the activation of the powder surface due to the passage of electric current which leads to high rate of atom diffusion. With the interplay of both pressure and temperature, powder-particles are well arranged and thus favoring high densification. Vasanthakumar *et al.* (2017) consolidated Ti-CNT composites and they reported an improvement in the sintered density of the composite at a high temperature of about 1200 ^{o}C. They also observed that higher temperature had a direct effect on the porosity of the composites. At higher temperature (1200 ^{o}C), no porosity was visible due to grain growth, even with the increase in the CNT content. The sintered composites at 800 ^{o}C and 1000 ^{o}C had porosities as shown in their microstructures (Figure 2.16). Porosity was observed to decrease with increasing temperature, this depicts that high sintering temperature can improve the relative density of the composites. The densification increased with the contents of CNT for sintered Ti-CNTs composites at 1200 ^{o}C, while the densification of sintered composites (Ti-CNT) at both 800 and 1000 ^{o}C decreased with increasing CNT contents. They also reported the effect of the temperatures on the hardness and the reduced modulus of elasticity of the sintered composites. The hardness of the Ti-5 wt% CNT and Ti-10 wt% CNT composites increased with the sintering temperature. Sintered Ti depicts same hardness at 800 and 1200 ^{o}C, meanwhile the

sintered Ti at 1000 ^{o}C showed an improved hardness due to the TiC present in the sample. It was observed that the addition of CNTs from 0-5 wt% increased the hardness at all the sintering temperatures but little or no significant increase was recorded from 5-10 wt% CNT. At 1200 ^{o}C, the hardness of Ti-10 wt% CNT was more than Ti-5 Wt% CNT due to high ratio of C/Ti, as shown in Figure 2.17. In the case of the reduced modulus of elasticity, significant increase was observed with the increase in CNT content at 1200 ^{o}C. However, a few deviations was observed at the lower temperatures as a result of the unreacted Ti, CNT and non-stoichiometric TiCx (Vasanthakumar *et al.*, 2017).

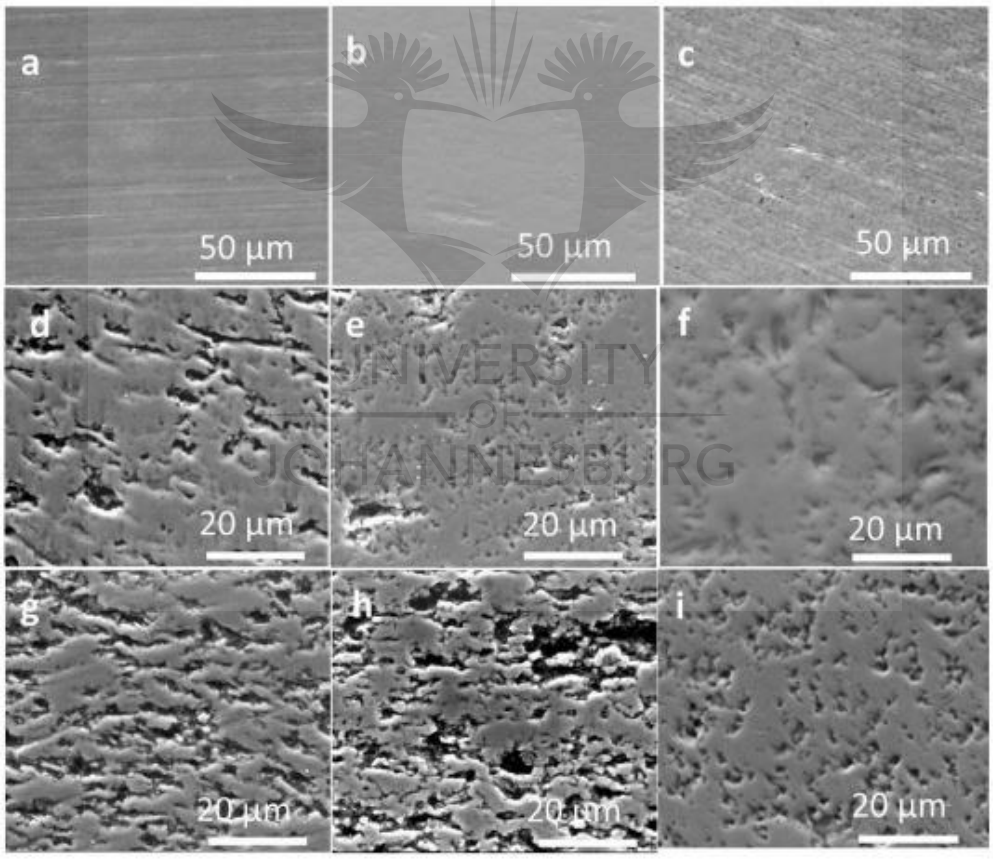

Figure 2.16. SEM micrographs depicting the cross section samples: Ti (a, b, c), Ti-5CNTs (d, e, f), and Ti-10CNTs (g, h, i) fabricated at the temperature of 800 ^{o}C, 1000 ^{o}C and 1200 ^{o}C respectively (Vasanthakumar *et al.*, 2017).

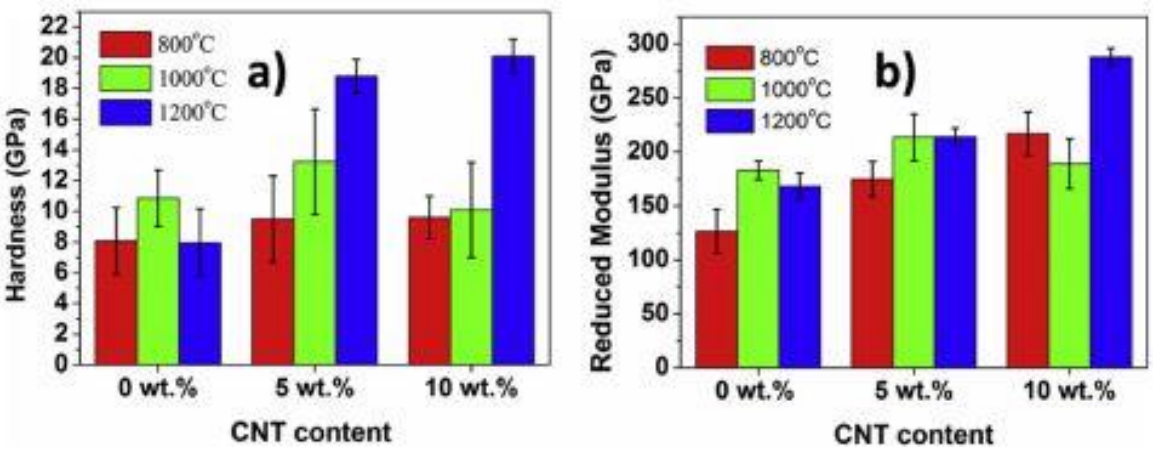

Figure 2.17. Plots showing nanohardness, and reduced modulus of the fabricated composites with CNTs weights and at different temperatures (Vasanthakumar *et al.*, 2017)

The influence of sintering temperature and heating rate on the properties of CNTs-Al matrix composites was investigated by Singh *et al.*, (2018). They noticed an increase in the microhardness of the composites due to the increase in sintering temperature (Figure 2.18a). This may be associated with the increase in densification and interparticle atomic bonding as a result of high temperature. Also, there was a rapid interparticle adhesion at higher temperature based on the joule heating of the particles, which was facilitated by the passage of the electric current (Ye *et al.*, 2006). The indentations of the hardness test with different sintering temperatures is presented in (Figure 2.18b-d). The indents of the fabricated composite at the temperature of 400 ^{o}C revealed the presence of cracks on the surface due to poor interparticle adhesion, as compared to the sintered composite at 600 ^{o}C which showed a perfect diamond shape. No evidence of crack was observed for this composite, this further revealed the influence of sintering temperatures on the hardness property. The hardness increased from 68 VHN to 81 VHN, as the temperature increased from 400 to 600 ^{o}C. The influence of the heating rate on microhardness was not as dominant as the sintering temperature. The sintered composite at the heating rate of 100 ^{o}C/min depicted the hardness of 71

VHN. The hardness increased to 77 VHN as the heating rate was reduced to 50 ^{o}C/min and a further decrease was observed in microhardness (74 VHN) as the heating rate was decreased to 25 ^{o}C/min.

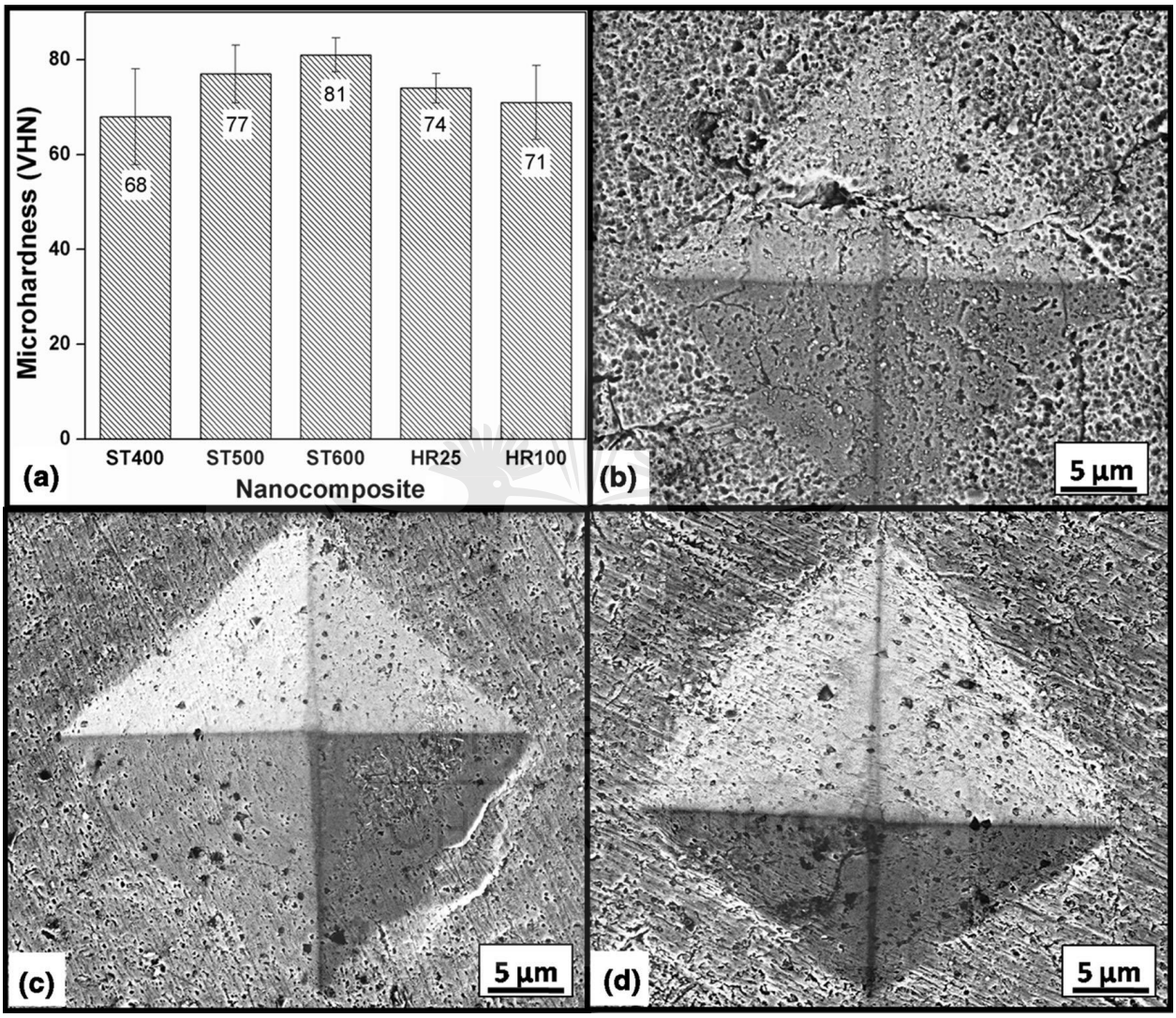

Figure 2.18. Microhardness results of the nanocomposites and SEM images of the microhardness indentation of the composites: (a) 400 ^{o}C, (b) 500 ^{o}C, and (c) 600 ^{o}C at the heating rate of 50 ^{o}C/min (Singh *et al.*, 2018).

They also reported the effect of sintering temperature on the elastic modulus and nanohardness of the sintered composites. A 48.8% and 20.2% increment were observed in the nanohardness and

elastic modulus of the composites as the temperature increased from 400 to 600 ^{o}C. Also, there was no significant impact of the heating on the nanohardness and elastic modulus respectively.

2.10 SUMMARY

The literature review on metal matrix composites, synthesis of carbon nanotubes and their dispersion techniques, fabrication techniques of CNTs reinforced metal matrix composites and their sintering parameters have been highlighted in this chapter. It revealed the challenges associated in obtaining a good CNTs dispersion within metal matrices and how it can be minimized. Over the years, different methods have been used to disperse CNTs, but it is worth noting that uniform dispersions of CNTs would improve the properties of metal matrix composites. Thus, dispersion of CNTs have been achieved by using the ball milling process. The role of ball milling has been highlighted in this review, with their effects on mechanical features of metal matrix composites. Although, the process is associated with some challenges, but with adequate control of milling parameters, defects and shortenings of CNTs can be minimized. The significance of SPS as a rapid sintering process and the role of its sintering parameters on mechanical properties have been reviewed, but it could be established that the reinforcement of CNTs into nickel aluminide has not been sufficiently investigated as compared to titanium and aluminum alloys.

CHAPTER THREE

3. EXPERIMENTAL

In this chapter, the materials, methods and equipment used for this research are analyzed. The methods utilized for this study involves:

1. As received powders
2. Milling of the as received powders
3. Dispersion and characterization of the milled composite powders
4. Consolidation of the milled powders

3.1 AS RECEIVED POWDERS

As received MWCNT powder (99.8% purity, 9.5 nm diameter) from Nanocyl, Belgium was used. The MWCNTs (1.0 wt.%) were added to nickel powder (99.5% purity, 0.5-3.0 µm average particle) from WearTech and aluminum powder (99.8% purity, 25 µm average particle size) from Technik GmbH (TLS) and Co. Spezialpulver, Germany.

3.2 MILLING OF THE AS-RECEIVED POWDER

The measured powders were charged in a 250 ml hardened steel container (diameter = 100 mm), containing two different steel balls (diameter (d) = 3 and 7 mm respectively) and the ball to powder ratio adopted was 10:1. The purpose of using the steel balls is to prevent the powders from being heated up and to increase impact energy during ball milling (Suryanarayana, 2001). The initial powder milling was done to synthesize the admixed powders at 150 rpm for 6 h in a low energy ball milling (LEBM, Germany, Retsch PM 100). Then, additional powder milling was carried out with high energy ball milling (Retsch PM 400, HEBM, Germany) at 80 rpm for the durations of 1 hour, 2 hours and 3 hours. At this stage the energy transfer in the ball milling is very

low to preserve the integrity of the nanotubes. This was carried out to ensure even distribution of nanotubes within the matrix. The planetary ball mill was shown in Figure 3.1(b).

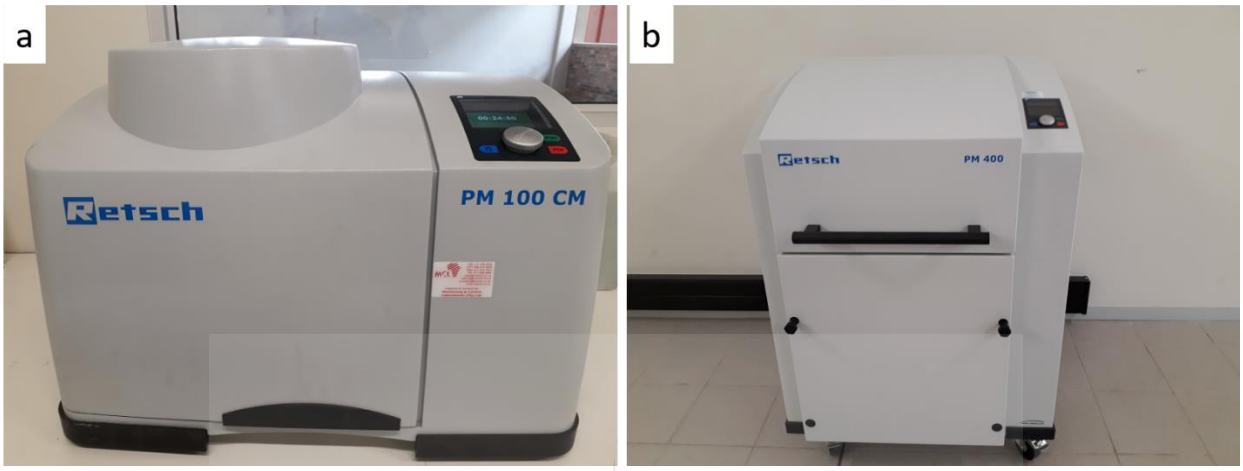

Figure 3.1 Planetary ball milling (a) Low Energy Ball Milling PM 100, and (b) High Energy Ball Milling PM 400

3.3 CHARACTERIZATION OF THE MILLED POWDERS

3.3.1 Morphology of the powders

The samples utilized for Field Emission Scanning Electron Microscope (FESEM, Carl Zeiss Sigma) furnished with energy dispersive X-ray spectrometry (EDS, Oxford) were prepared by using a double-sided carbon tape fixed into a sample holder to gather small amount of powders. The mounted samples were placed in an automatic carbon cord coater (Turbomolecular pumped coater, Q150T E) consisting of graphite rods, where the samples were coated. This was carried out to make the samples conductive and to prevent charging during SEM analysis. The SEM utilized has a beam of high energy electrons which was employed to scan the surface of the samples thereby producing a magnified image. The microscopy has a high magnification up to 1 million times and was used to generate high resolution images. Furthermore, the signals from the electron-sample interactions showed the detailed information about the sample's morphology and reinforced sample arrangement. The EDS was used to confirm the composition of the samples for the purpose

of qualitative analyses. The morphology of the samples was carried out using the SEM (Figure 3.2). The crystal orientation of the samples was analysed using the Electron backscattered diffraction detector (EBSD). The consolidated samples were polished using Eposil M Colloidal Silica to prepare the surface and EBSD analysis was performed on the polished surface of the samples with a step size of 0.5 µm and a voltage of 20 kV. The grain size and the crystallographic orientation were analyzed with AZtecHKL software (Denmark) and the EBSD maps were obtained.

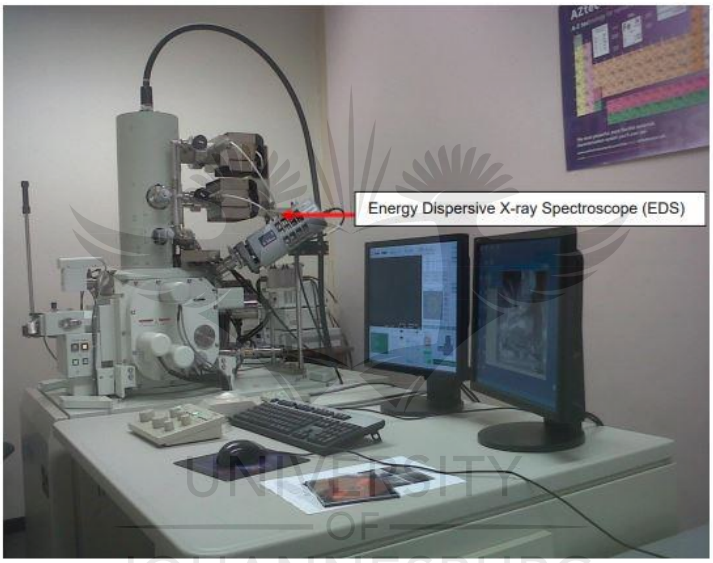

Figure 3.2 FESEM, Carl Zeiss Sigma Scanning Electron Microscope

3.3.2 Transmission electron microscopy of the powders

The samples used for Transmission Electron Microscopy (TEM, JEOL-Jem 2100) were prepared by dispersing the powders in ethanol for 20 minutes with the aid of an ultrasonicator bath (Mecan, MC-PS-06A). Then, copper grids coated with a holey carbon film (Ayache *et al.*, 2010), were immersed in the sonicated samples for few seconds. The high resolution TEM used for analysis, has an electrons beam transferred through the prepared ultrathin specimen, thereby interacting with the specimen as it travels through it. The TEM has a maximum accelerating

voltage of about 200 KV, resolution of 0.14 nm (lattice image) and a magnification between 30 to 800,000. The TEM image was formed with the influence of the electrons as the beam was transferred through the sample. Thus, the image is magnified and focused on a screen. The equipment was used to observe the morphology and the dispersion level of nanotubes (Figure 3.3).

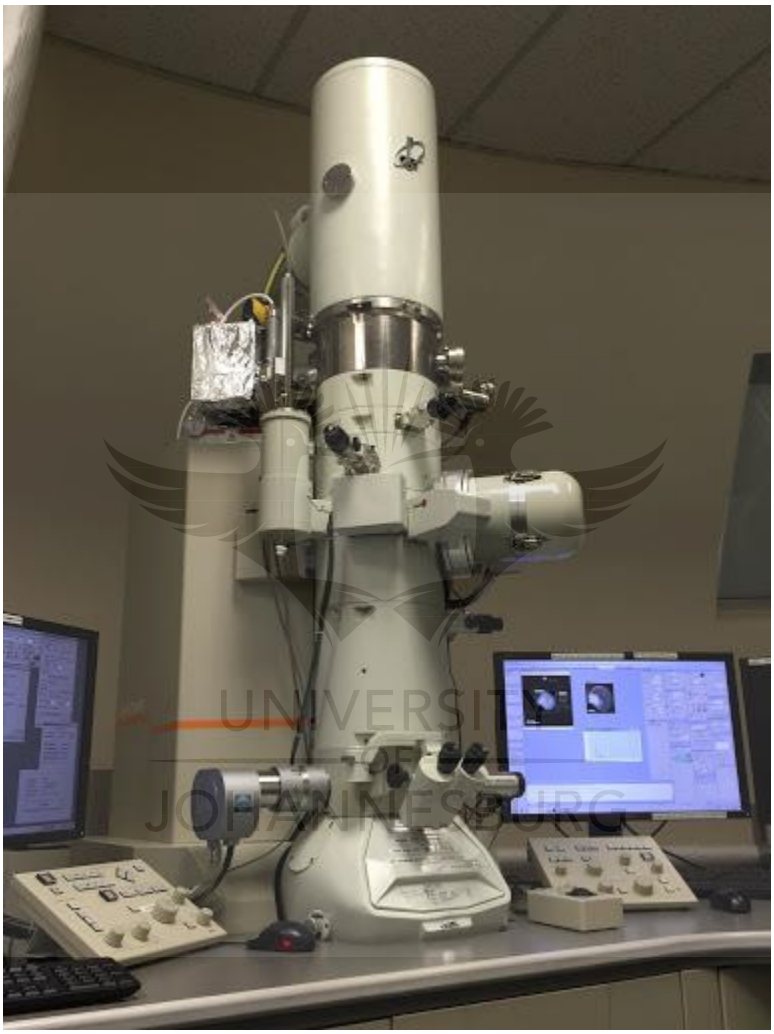

Figure 3.3 JEOL-JEM 2100, Transmission Electron Microscope

3.3.3 X-ray diffractometer of the sample

The samples for X-ray diffractometer (Rigaku, Ultima IV, XRD) were prepared by placing the sample in the sample holder. The sample holder was placed in the path of an X-ray beam. X-ray diffraction was observed through the sample and in the detector. Both the detector and beam rotate

over an angular range. The scanning of the sample was carried out between a low and medium elevated temperature (-180 to 350 ^{o}C). It has an accelerating voltage of 40 KV, current of 30 mA and a maximum rated output of 1.2 KW. The evaluation of structural identification and crystalline phases of the fabricated samples was conducted upon the polished samples by making use of Cu-Ka radiation (λ = 0.154). XRD was scan at a speed of 0.500 deg/min over the angular range of 10-90^{o}. PDXL integrated X-ray diffraction software was used as a search-match routine in order to identify the phases present in the samples. Likewise, the peak positions and intensities were determined from automatic integration procedures. The phase identifications of the samples were analyzed using XRD (Figure 3.4).

Figure 3.4 Rigaku X-Ray Diffractometer

3.3.4 Raman analysis of the powders

The specimens used for Raman microspectrometer (WITec Alpha300 R confocal, Germany) were placed (a few specimens) on the glass slide by using a spatula (stainless steel), before

mounting on the Raman stage. The microspectrometer was calibrated with a silicon standard before acquisition commenced. Beam centering and Raman spectra calibration were performed before spectral acquisition using a Si standard (111). The 5X and 20X Nikon objectives lens were used to collect the scattered radiation and, when needed, the 50X lens was used for more detailed analysis, with a laser power of 3 mW. The laser interacts with the specimen, the specimen was focused, and the images were obtained within the acquisition time of 2 sec. The specimens were analyzed at the spectra range of 300-2500 cm^{-1}, with a 532 nm laser at 5 different positions. WITec (Software 2.5) was used to analyze the Raman spectra into two Gaussian peaks. This was performed to determine the intensity, peaks, and extent of defects done to the MWCNTs (Figure 3.5).

Figure 3.5. WITec Focus Innovations Raman spectroscope.

3.3.5 Consolidation of the powders

The samples used for consolidation were measured and consolidated by spark plasma sintering (SPS, HHPD-25, FCT, Germany) in a die (graphite) containing the sintering punches. Graphite foils were inserted in the die, and between powders and sintering punches; furthermore, porous graphite felt was used to protect the die exterior. The consolidation of milled samples was carried

out in a vacuum using the following sintering parameters; 1000 ^{o}C, 50 MPa, 10 min, as the sintering temperature, pressure, holding time and the heating rates of 50 ^{o}C/min, 100 ^{o}C/min, and 150 ^{o}C/min respectively.

3.4 CHARACTERIZATION OF THE SINTERED SAMPLES

3.4.1 Relative density of the sintered samples

The samples were placed in a weigh balance which contain a beaker filled with de-ionized water. The weight in air of the samples was taken, subsequently the samples were placed in the beaker and the weight in water was recorded. The relative density (RD) of the sintered samples was carried out in line ASTM B962 (Cavaliere *et al.*, 2017), which is based on Archimedes' principle. The RD was calculated with reference to the theoretical density (TD). The equations below was used in our calculations;

$A = \frac{a}{a-b}$ ---------- (equation 3.1)

Hence, the mass of the sintered sample in air and water are represented by *a,* and *b;* and *A* is the experimental density. The TD was determined by the formula;

$R_D = \frac{1}{\frac{w_x}{D_x} + \frac{w_y}{D_y}}$ ---------- (equation 3.2)

Relative density ($R_{D)} = \frac{Experimental\ density}{Theoretical\ density}$ $_x$ 100% --------- (equation 3.3)

Thus, the weight fraction of the matrix and reinforcement are denoted by w_x and $w_{y,}$ while the density of the matrix and reinforcement are denoted by D_x and D_y.

3.4.2 Morphology of the sintered samples

Field Scanning Electron Microscopy (FESEM, Carl Zeiss Sigma), furnished with energy dispersive X-ray spectrometry (EDX detector) was used to analyze the morphology of the consolidated samples. The samples were prepared by placing the samples in a 20 mm (diameter)

mounting cup. Then, the prepared mixture of catalyst and resin was poured on the samples. The cold mounted samples were grounded by using MD-Molto 220 and fine grounded on MD-Largo disc with 6 μm diamond suspension. The samples were further polished on MD-Allegro disc with 3 μm diamond suspension and fine polished on Aka-Chemal with fumed silica suspension in order to achieve a mirror-like surface. The polished samples were rinsed with distilled water and allowed to dry. Afterwards, the cold mounted resins were removed carefully from the samples before observing the morphology of the samples through the SEM (Figure 3.2) and EDX (confirm the composition of the samples).

3.4.3 Vickers microhardness of the sintered samples

The hardness test was carried out using Vickers microhardness (Micro star 2000, inc., Figure 3.6) at room temperature on polished samples. The samples were placed on the motorized XY-stage of the machine and bright view of the surfaces was achieved under low magnification lens by adjusting the focus. An impression was made on the samples with the aid of the indenter at a load of 4.90 N and dwell time of 10 seconds. The average value of five indentations was recorded at intervals. The Vickers microhardness tester comprises of 2 indenters, working distance objectives, optical zoom system and loads of 0.098, 0.246, 0.49, 0.98, 1.96, 2.94, 4.90, to 9.8 N.

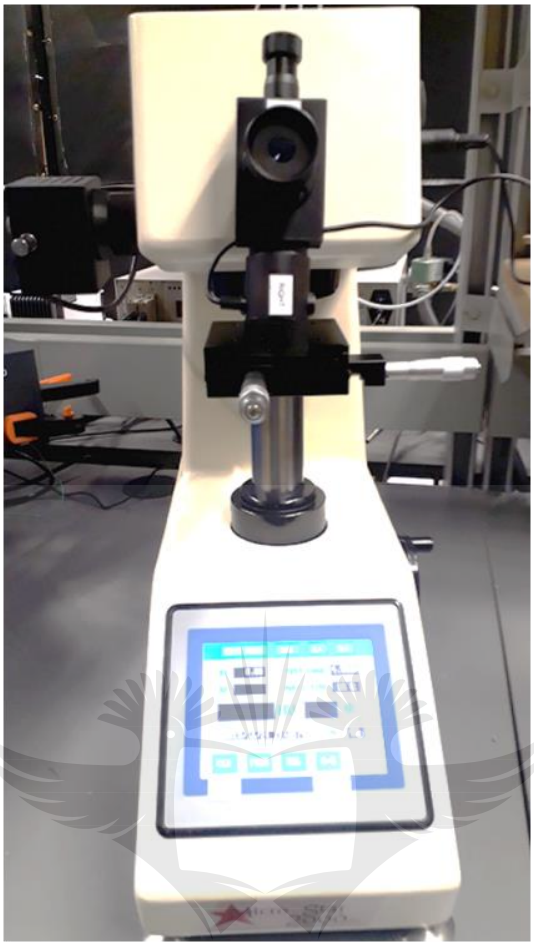

Figure 3.6. Micro Star 2000, Vickers microhardness tester.

3.4.4 Nanoindentation analysis of the sintered samples

Nanoindentation test was done on an ultra nanoindenter, on polished samples using a diamond indenter (Berkovich, Figure 3.7). The technique measures the time, and depth against load of an indenter tip of the sample (Fischer-Cripps, 2006). The indenter tip was calibrated to achieve uniformity and the tests were carried out using a load of 75 mN. Seven indentations were taken per sample with 8 µm spacing to prevent work hardening (Džunić *et al.*, 2015). Also, a period of 1000 sec was used to measure the time dependent properties and all the experiment was carried out in agreement with ISO 14577 (Maja *et al.*, 2018). Thereafter, the mechanical attributes of the

samples such as nanohardness and elastic modulus, were determined from the information of the unloading and loading cycle (Pillai *et al.*, 2012).

Figure 3.7. Nanoindentation.

3.4.5 Wear behaviour of the sintered samples

Wear analysis was carried out using a ball on disc tribometer (Anton Paar GmbH, Austria) (Figure 3.8) with stainless steel ball as the counterface material upon the polished samples. The tribometer is furnished with double Linear Voltage Displacement Transducer sensor, positioned on each side of the arm for measuring the frictional force. The samples were placed on the disc and different loads were applied during the test. The test was performed in a manner that would enable the ball to make a reciprocating movement on the samples. The sliding wear test was done at varied sliding loads of 2 N, 5 N, and 8 N at linear speed of 15.91 cm/s and the coefficient of friction were monitored during the test.

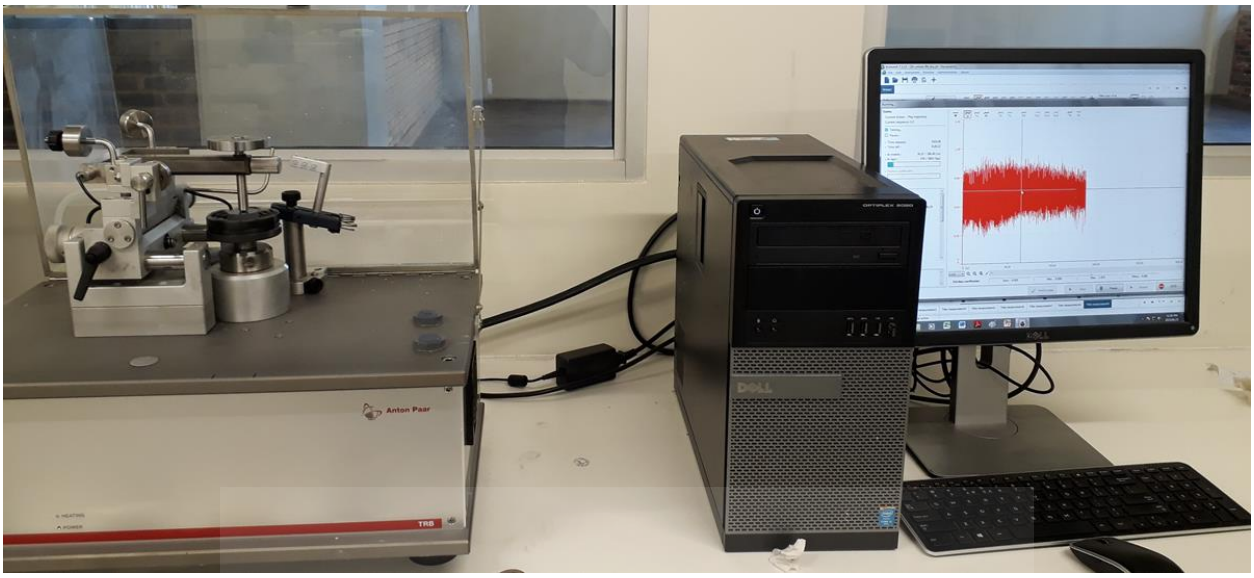

Figure 3.8. Ball on disc tribometer.

CHAPTER FOUR

4 RESULTS AND DISCUSSION ON THE DISPERSION CHARACTERISTICS OF MWCNTs INTO NiAl

This chapter presents the characterization of the as-received powders (Ni, Al and MWCNTs) and the admixed powders. SEM was utilized to obtain the morphologies of all the starting and the admixed powders, and EDS was used to analyze the chemical composition of the powders. The phase identification of the admixed powders was determined from the XRD analysis. The dispersion characteristics and structural integrity of the as-received MWCNTs and the dispersed composite powders at different HEBM times were determined using the TEM and Raman analysis.

4.1 MORPHOLOGY OF THE STARTING POWDER

Figure 4.1 shows the SEM image and the EDS spectrum of the as-received Al powder. Al particles are spherical with smooth and nonporous surface, depicting bundled satellites. The EDS analysis revealed the peak of Al, as shown in Figure 4.1(c). Figure 4.2 represents the SEM micrograph and EDS spectrum of the as-received Ni powder. It was observed that Ni particles are uneven in shape, forming clusters. The EDS spectrum revealed the peaks of Ni as the elemental composition present in the particle, as shown in Figure 4.2(c). Figure 4.3 denotes the image of the MWCNTs with agglomerated tube-like shape (highly entangled), due to Van der Waals forces and high aspect ratio presents in the nanotubes (Munir *et al.*, 2015).

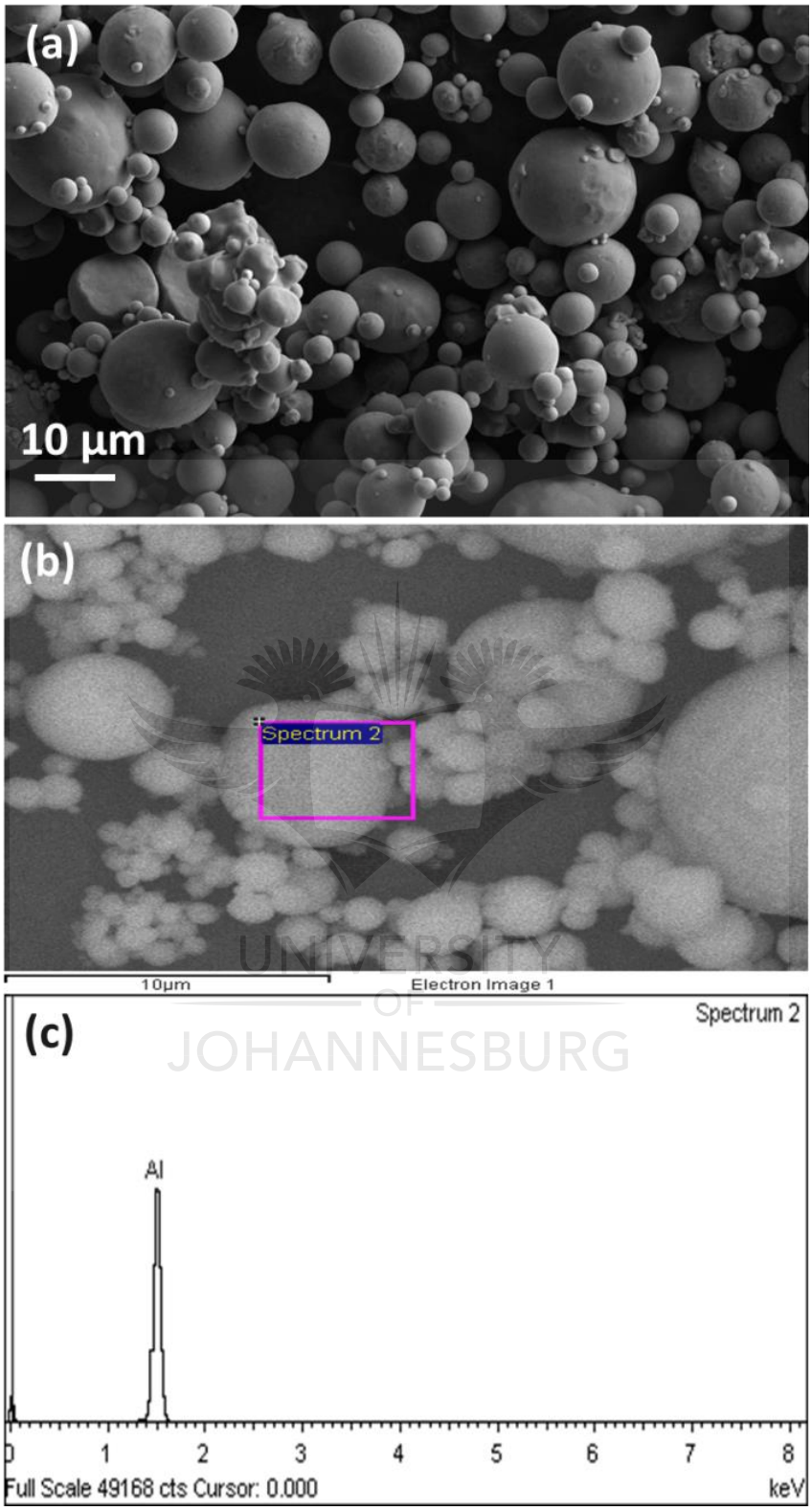

Figure 4.1. SEM micrograph of Al particles: (a) Nonporous and clustered satellite, (b and c) EDS spectrum.

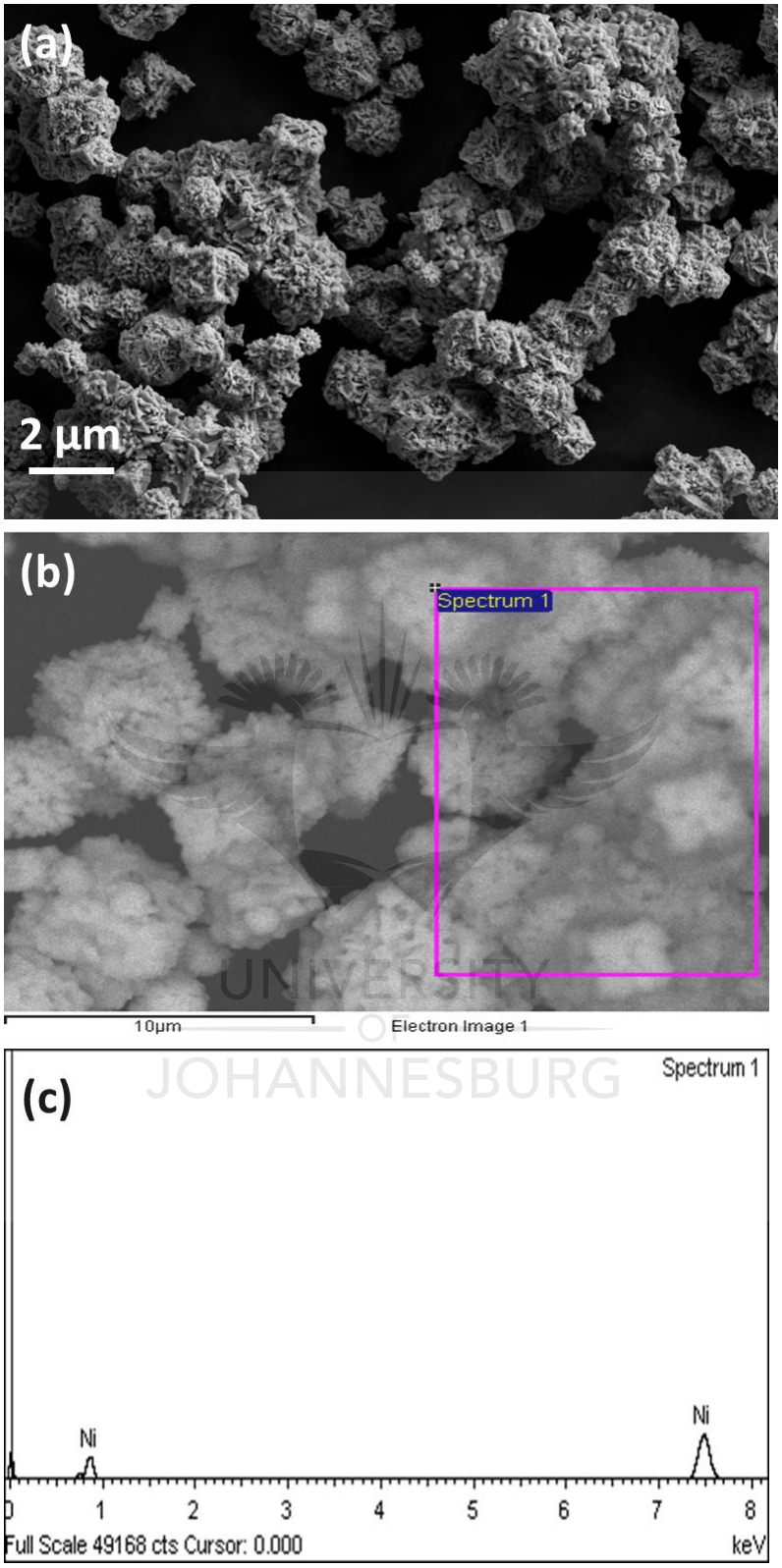

Figure 4.2. SEM micrograph of Ni particles: (a) Irregular shape, (b and c) EDS spectrum.

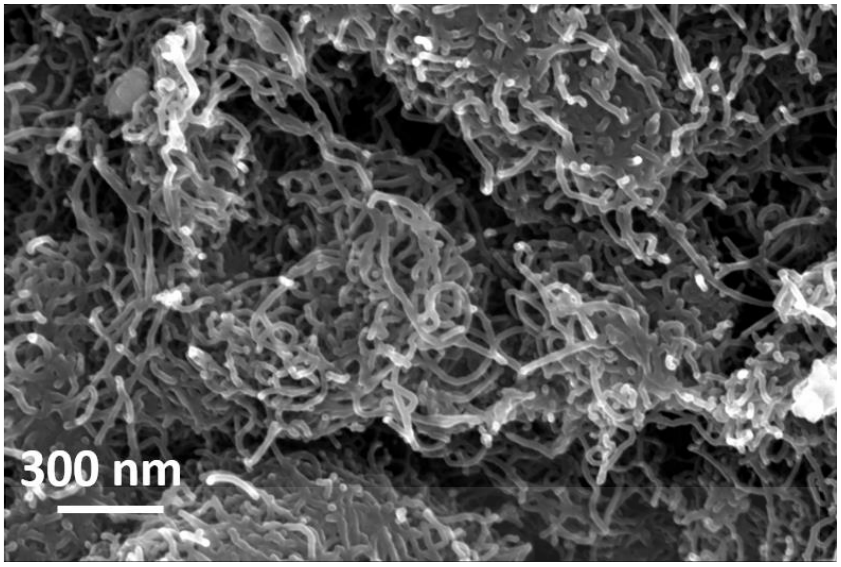

Figure 4.3. SEM micrograph of MWCNTs.

4.2 MORPHOLOGY OF THE MILLED POWDER

Figure 4.4(a-d) shows the SEM images of the milled powders. Figure 4.4(a) shows the image of NiAl powder with large rough particles, the structure was obtained from ball collisions of Ni and Al particles resulting to cold welding and fracturing (Suryanarayana, 2001). Figure 4.4(b) denotes the SEM micrograph of the milled NiAl-1wt% MWCNTs composite powder with the HEBM of 1 hour. The white arrows in the micrograph point to the dispersion of MWCNTs in the metal matrix and the red circle point to the clustered MWCNTs due to poor wettability. The micrograph of the milled NiAl-1wt% MWCNTs composite powder with the HEBM of 2 hours was represented in Figure 4.4(c). The image depicts the agglomeration of MWCNTs in NiAl metal matrix as illustrated using a red dotted circle. Meanwhile, Figure 4.4(d) depicts the dispersed composite powder with the HEBM of 3 hours. The white arrows on the micrograph point to the regions of dispersion, and the clustered MWCNTs were also represented by a red circle. This study suggests that the agglomerations of MWCNTs in the metal matrix was due to the inability of the impact energy to overpower the strong Van der Waals forces between the nanotubes (Munir

& Wen, 2016). It was observed from the image that the dispersed composite with HEBM of 1 hour showed fewer agglomerations of MWCNTs in the metal matrix.

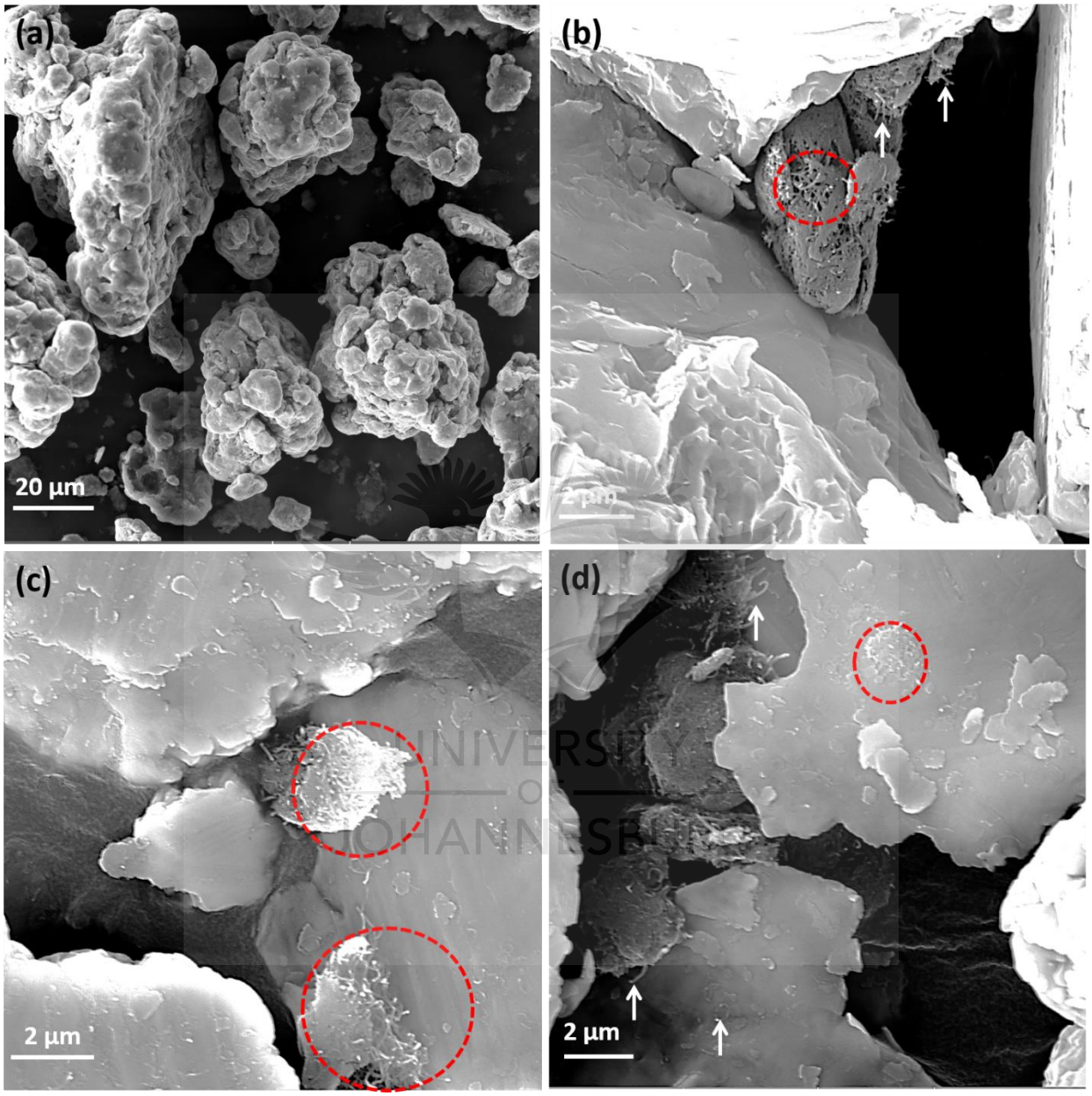

Figure 4.4. SEM micrograph of the milled powders: (a) NiAl, (b) NiAl-1wt% MWCNTs, HEBM for 1 h, (c) NiAl-1wt% MWCNTs, HEBM for 2 h, and (d) NiAl-1wt% MWCNTs, HEBM for 3

4.2.1 XRD analysis of the milled powder

Figure 4.5 denotes the XRD diffractographs of the powders which consists of NiAl and NiAl-1 wt% MWCNT composites respectively. From the diffractographs, the peaks of the milled powders were not broadened. The highest peak in the pattern indicates the formation of NiAl which has ordered body centered cubic structure (a strukturbericht-superstructure designation of B2), which is made up of ordered crystal structure of simple CsCl prototype (Talaş, 2018). NiAl peaks were observed at 2Θ = 44.63º, and 65.54 º which corresponds to the planes (110) and (211). However, the formation of nickel carbide (NiC, a precipitate) was seen in the diffractograph of the composite powders, maybe due to the impact of the ball milling. NiC peaks were seen at 2Θ = 38.9 º, 44.63 º, 52.3 º, 74.5 º which corresponds to the planes (111), (110), (200), and (220) respectively.

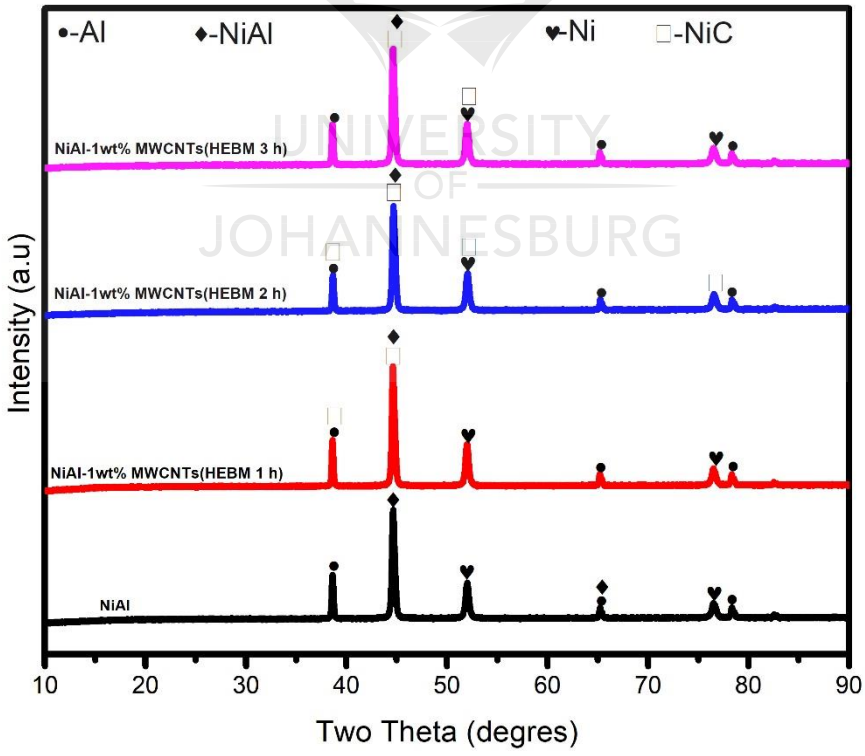

Figure 4.5. XRD patterns of milled NiAl and NiAl- 1 wt % MWCNTs composites at different milling time.

4.2.2 Raman analysis of the milled powder

Raman spectroscopy is used to determine the structural integrity of MWCNTs in the matrix powder**.** This consists of two graphitic peaks known as D and G bands respectively. The D band peak is associated with disorder C-C networks, which indicates a non-crystallinity (non-sp^2 structural defects) in graphitic materials while the G band is termed as the in-plane stretching mode in C-C networks. This peak corresponds to the level of crystallinity (Delhaes *et al.,* 2006). The Raman spectra of MWCNTs and the dispersed NiAl-MWCNTs composite powders at 1 hour, 2 hours and 3 hours respectively are presented in Figure 4.6. The D and G bands of MWCNTs was observed at 1350 and 1575 cm^{-1} respectively and it had the I_D / I_G ratio of 0.802, which indicates a dominance of crystallinity over the non-crystallinity. Moreover, the decrease in the intensity of G band may be ascribed to non-crystallinity (McCarthy & Thedchanamoorthy, 1988; Ferrari, 2007). The milled NiAl-1wt% MWCNTs powder (HEBM, 1 hour) had the I_D/I_G ratio of 0.895 which indicates a 11.5% increase than the as-received MWCNTs. The composite showed similar and broadened peaks, which suggests that the integrity of MWCNTs are not fully preserved in the matrix. The milled NiAl-1wt% MWCNTs powder (HEBM, 2 hours) had the I_D/I_G ratio of 0.896 which indicates a 12% increase than the as-received MWCNTs, and the dispersed NiAl-1wt% MWCNTs powder (HEBM, 3 hours) had the I_D/I_G ratio of 0.933 which indicates a 16% increase from the as-received MWCNTs, which suggests a more dominance of non sp^2 disorders over sp^2 C-C bonds. The I_D/I_G ratio increased as the dispersion time of MWCNTs in NiAl matrix increased.

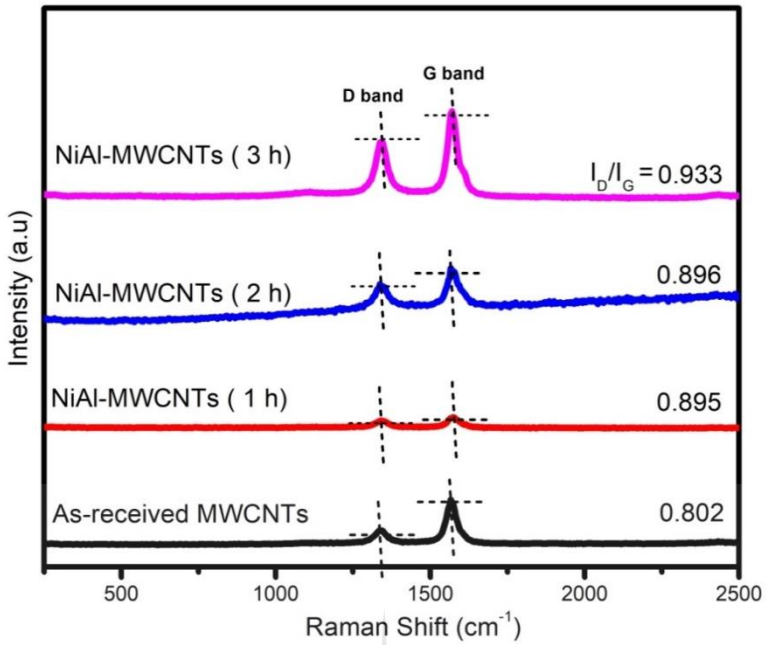

Figure 4.6. Raman spectra of the as received MWCNTs and the milled NiAl-1wt% MWCNTs composites.

4.3 DISPERSION CHARACTERISTICS OF MWCNTs AND NiAl –MWCNTs

The dispersion characteristics of the as-received MWCNTs and the NiAl-1wt% MWCNTs composite powders were analyzed with the TEM, to depicts the selected area of electron diffraction pattern (SAED), Fast fourier transform (FFT), and the walls of the MWCNTs.

4.3.1 Diffraction pattern of the as-received MWCNTs

The SAED is used to examine the crystallographic information, amorphous phases, dislocations (partial rings, extra spots and streaks) and crystalline phases in composites. The SAED pattern of the MWCNT was presented in Figure 4.7(a), with a bright ring which matches the interplanar spacing and the pattern of a graphite ring. It consists of many rings which corresponds to a set of atomic planes of graphite (Asadabad & Eskandari, 2016). In the SAED pattern of MWCNTs, the observed planes (002) and (101) suggests a high crystallinity of carbon nanotubes. They are identified with similar chiralities of zigzag type, bright coaxial ring, and without planes dislocation

(Sreekanth *et al.*, 2014; Jafari Eskandari *et al.*, 2017). The TEM image of MWCNTs (Figure 4.7(b)), revealed an entangled nanotubes due to Van der Waals forces and high aspect ratio presents in the nanotubes (Munir *et al.*, 2017a). The image of the MWCNT walls has an interlayer spacing of 0.345 nm, as shown in Figure 4.7(c). Furthermore, the fast fourier transform (FFT) of the MWCNTs in Figure 4.7(d) was observed with narrow tips, and this indicates the nature of crystallinity in the nanotubes (Lehman *et al.*, 2011).

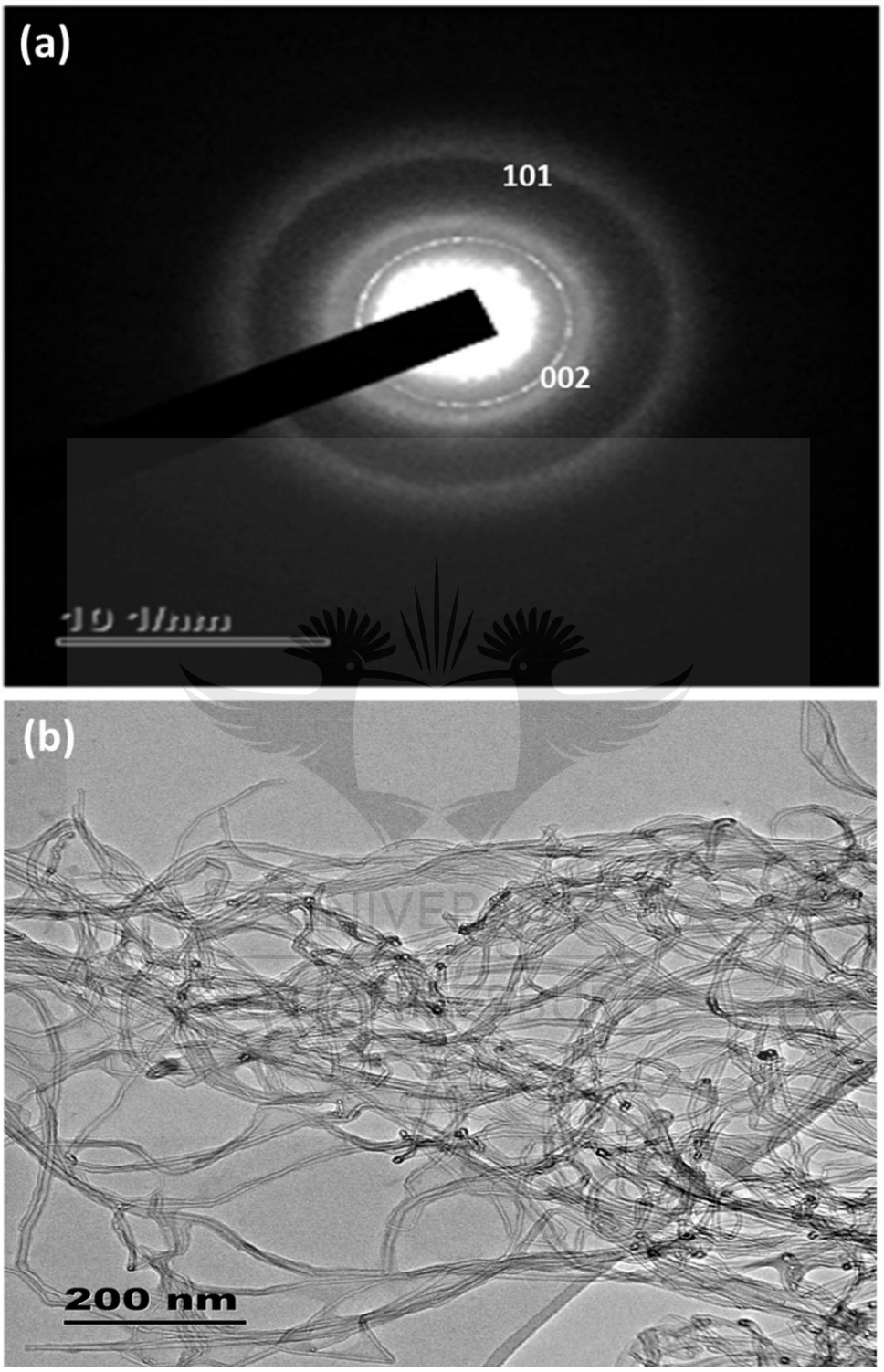
(a)
101
002
(b)
200 nm

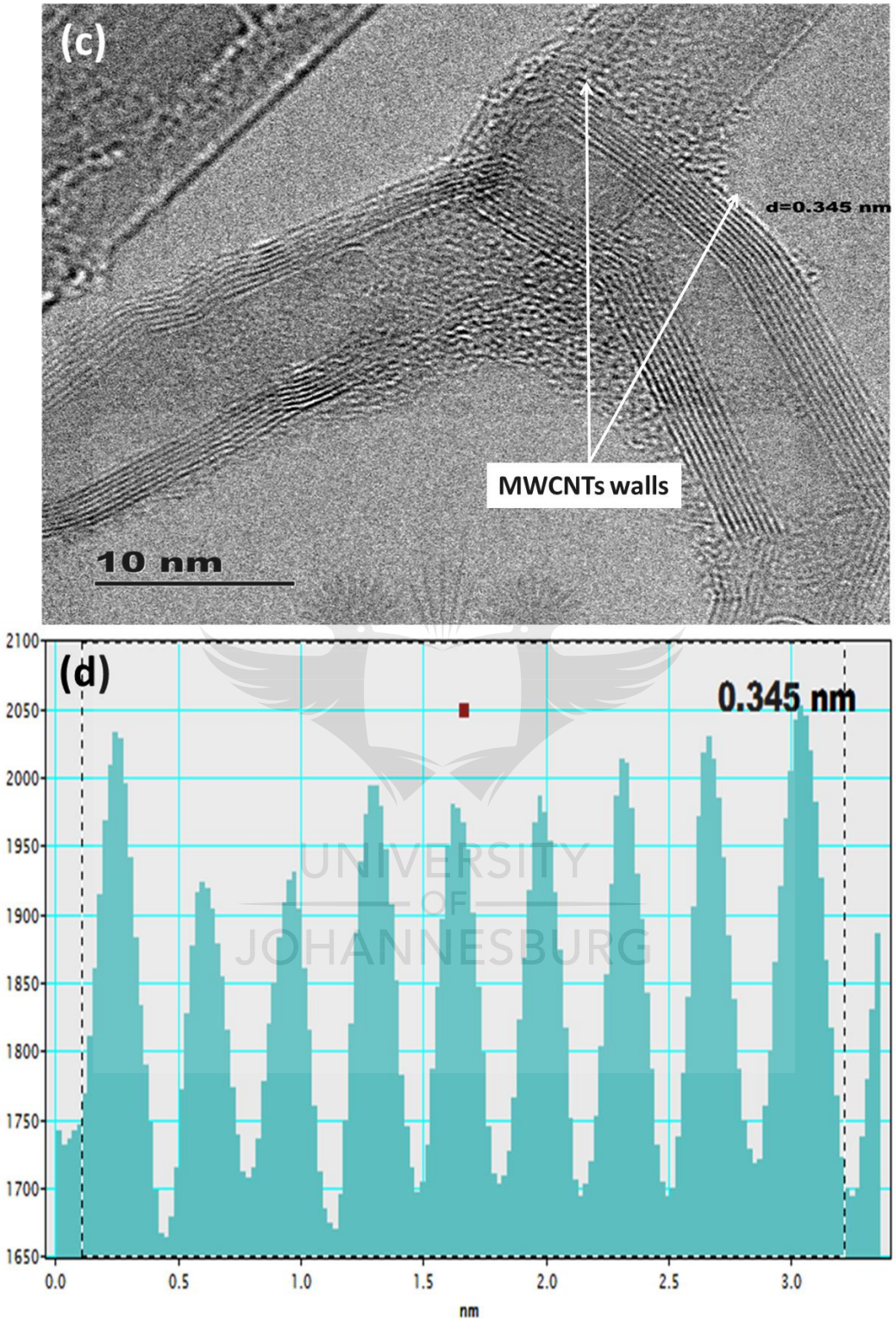

Figure 4.7. HRTEM of as received MWCNTs showing the: (a) SAED pattern, (b) image of clustered nanotubes (c) MWCNTs walls, and (d) FFT.

4.3.2 Milled NiAl - 1wt% MWCNTs composite

The SAED pattern of the milled NiAl-1wt% MWCNTs composite powder (HEBM, 1 hour) was presented in Figure 4.8(a). The coaxial and halo rings were still intact as compared to the graphitic ring (as-received MWCNTs). The rings were not fully coaxial, but revealed some streaks and extra spots, which denotes the presence of dislocations on the structure of nanotubes during dispersion. This further results to the presence of non-sp^2 disorder which scatters electrons during diffraction. Furthermore, there was no observation of the formation of streak on spots in the coaxial ring which take place during severe dislocation accumulations that distorts the crystal orientations of the nanotubes. The big spots on the SAED pattern may be ascribed to the matrix and precipitate observed (Asadabad & Eskandari, 2016). The atomic planes (002) and (101) were still present in the ring. The TEM micrograph of the milled NiAl-1wt% MWCNTs composite powder (Figure 4.8(b), shows a relative dispersion of MWCNTs within the NiAl matrix (pointed with orange arrows) due to the impact force applied during the milling process. This energy overcame the Van der Waals forces in the nanotubes. The walls of the MWCNT were measured to determine extent of the strain in the composite, and it shows an interlayer spacing of 0.3502 nm (1.5% increase than the as-received MWCNTs) as shown in Figure 4.8(c). It indicates that the walls of nanotubes were subjected to some extent of bending stresses or strain during the milling process. Furthermore, the fast fourier transform (FFT) of the milled NiAl-1wt% MWCNTs in Figure 4.8(d) showed slight broad tips, and this indicates the nature of non-crystallinity in the nanotubes.

The SAED pattern of the milled NiAl-1wt% MWCNTs composite powder (HEBM, 2 hours) is presented in Figure 4.9(a). The coaxial and halo rings were fading out gradually as compared to the composite powder (HEBM, 1 hour). This is an indication of strain on the planes (002) and (101) during ball milling. Also, the rings were not fully coaxial, showing the presence of more

streaks and extra spots due to dislocations as illustrated in the composite (HEBM, 1 hour). This further indicates the presence of more amorphous carbon which scatters electrons during diffraction. The TEM micrograph of the dispersed NiAl-1wt% MWCNTs composite powder (Figure 4.9(b), shows the agglomerations of MWCNTs within the NiAl matrix. This may be due to severe plastic deformation during the dispersion of MWCNTs, when the milling time was prolonged. It may have compromised the exclusive structure of the MWCNTs (Okoro *et al.,* 2019). The composite was observed with the interlayer spacing of 0.3516 nm (1.9% increase than the as-received MWCNTs), as shown in Figure 4.9(c). It depicts that the composite was subjected to more strains during the prolonged milling. Furthermore, the fast fourier transform (FFT) of the milled NiAl-1wt% MWCNTs in Figure 4.9(d), was observed with broader tips, and this indicates more defects in the nanotubes.

The SAED pattern of the milled NiAl-1wt% MWCNTs composite powder (HEBM, 3 hours) was presented in Figure 4.10(a). The coaxial and halo rings were fading out gradually, which is an indication of more strain on the planes (002) and (101) during ball milling. Also, the rings were not fully coaxial, showing the presence of more streaks and extra spots due to dislocations as illustrated in the composite (HEBM, 1 hour). The TEM micrograph of the milled NiAl-1wt% MWCNTs composite powder (Figure 4.10(b), shows more agglomerations of MWCNTs within the NiAl matrix. This may be due to severe plastic deformation during the dispersion of MWCNTs, when the milling time was more prolonged. The powder was observed with the interlayer spacing of 0.3540 nm (2.6% increase than the as-received MWCNTs), as shown in Figure 4.10(c). It depicts that the composite was subjected to more strains during the prolonged milling. Furthermore, the fast fourier transform (FFT) of the milled NiAl-1wt% MWCNTs in Figure 4.10(d), was observed with more broader tips, and this indicates more defects in the nanotubes.

From the milled NiAl-1wt% MWCNTs composite powders (HEBM, 1 hour, 2 hours and 3 hours), it was observed that there were formation of streaks and extra spots on all the powders which showed the presence of dislocations on the structure of the nanotubes. It depicts that the nanotubes were subjected to strain during the dispersion and there were more strains as the dispersion time was prolonged. The dispersion of MWCNTs in NiAl matrix can be achieved when the impact energy applied on the powders is enough to overcome the Van der Waals forces in the nanotubes. The impact energy applied on powders during HEBM is function of the milling time, charged powders, collision of balls and milling speed. HEBM can inflict higher mechanical energy on powders to yield uniform dispersion of MWCNTs, but not at the expense of the structural integrity of the MWCNTs. From this study, the impact energy applied on the composite powders could not overcome the Van der Waals forces in the nanotubes. This was observed with the TEM analysis of the composites, depicting the presence of streak and extra spots. Although, relative dispersions were achieved with NiAl-MWCNTs (HEBM, 1 hour) powder, as compared with the composites with prolonged dispersion time.

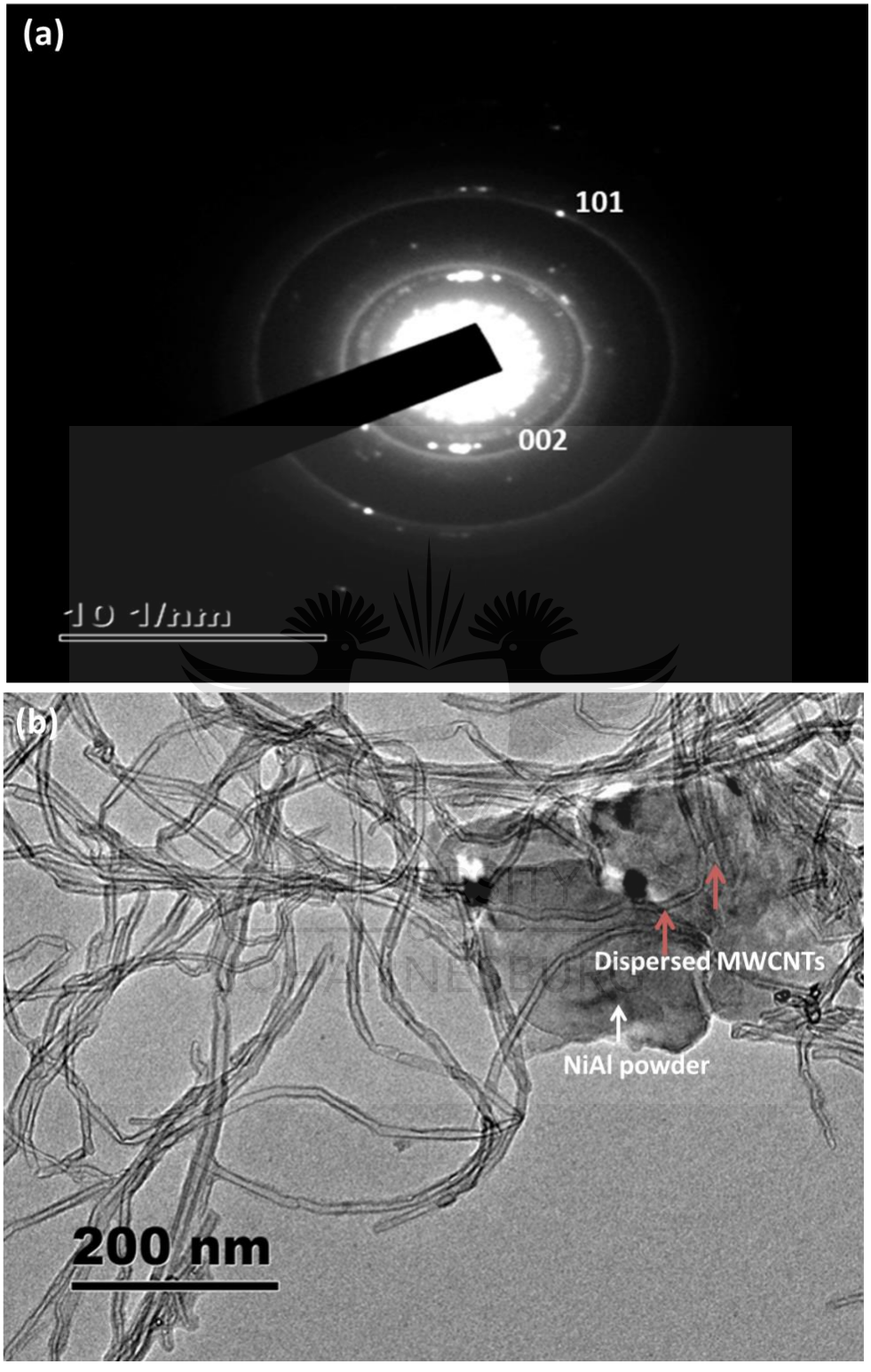
(a)
101
002
10 1/nm
(b)
Dispersed MWCNTs
NiAl powder
200 nm

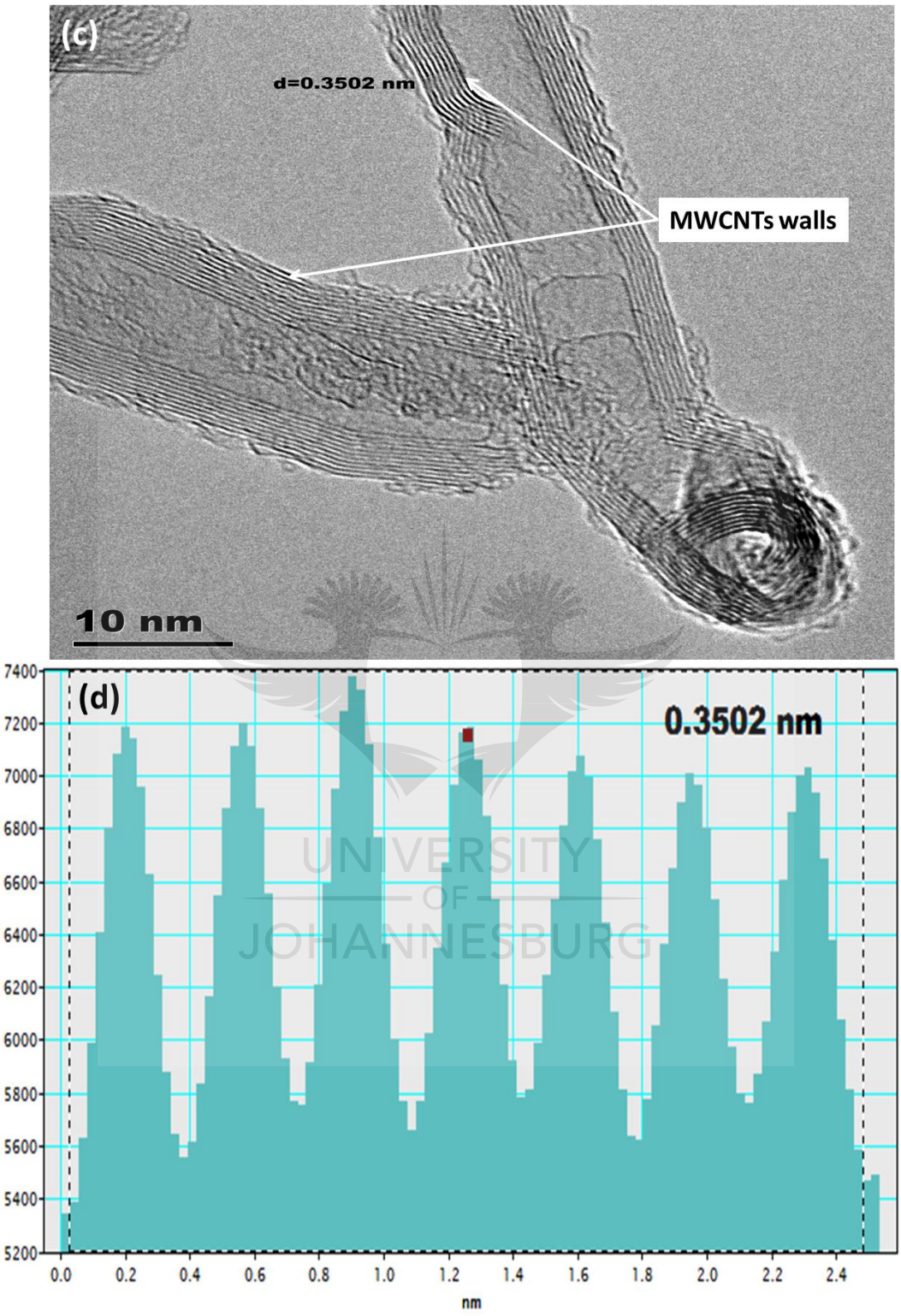

Figure 4.8. HRTEM of the milled NiAl-1wt% MWCNTs, HEBM 1 hour: (a) SAED pattern, (b) Image the composite (c) MWCNTs walls and (d) FFT

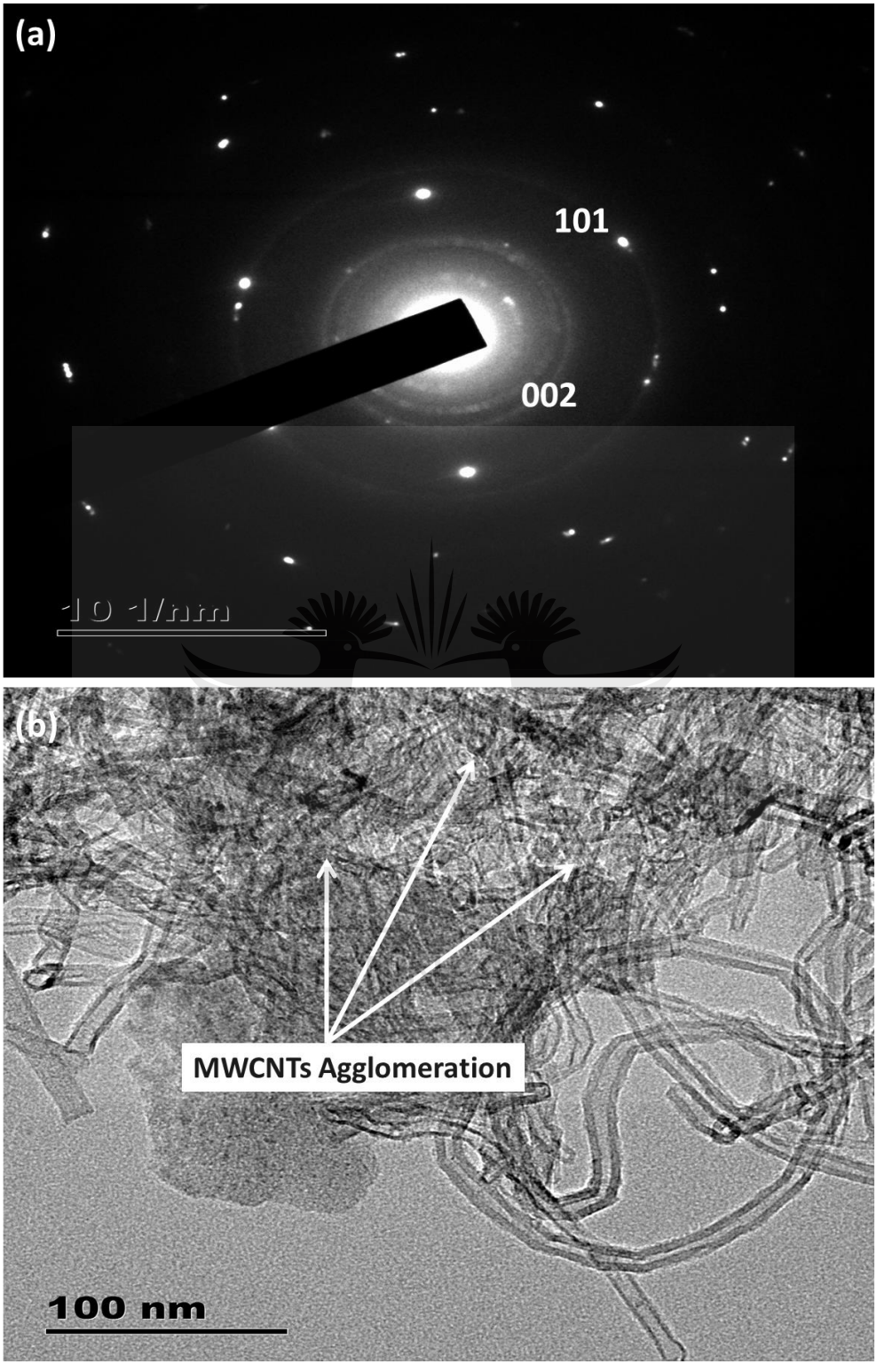
(a)
101
002
5 1/nm
(b)
MWCNTs Agglomeration
100 nm

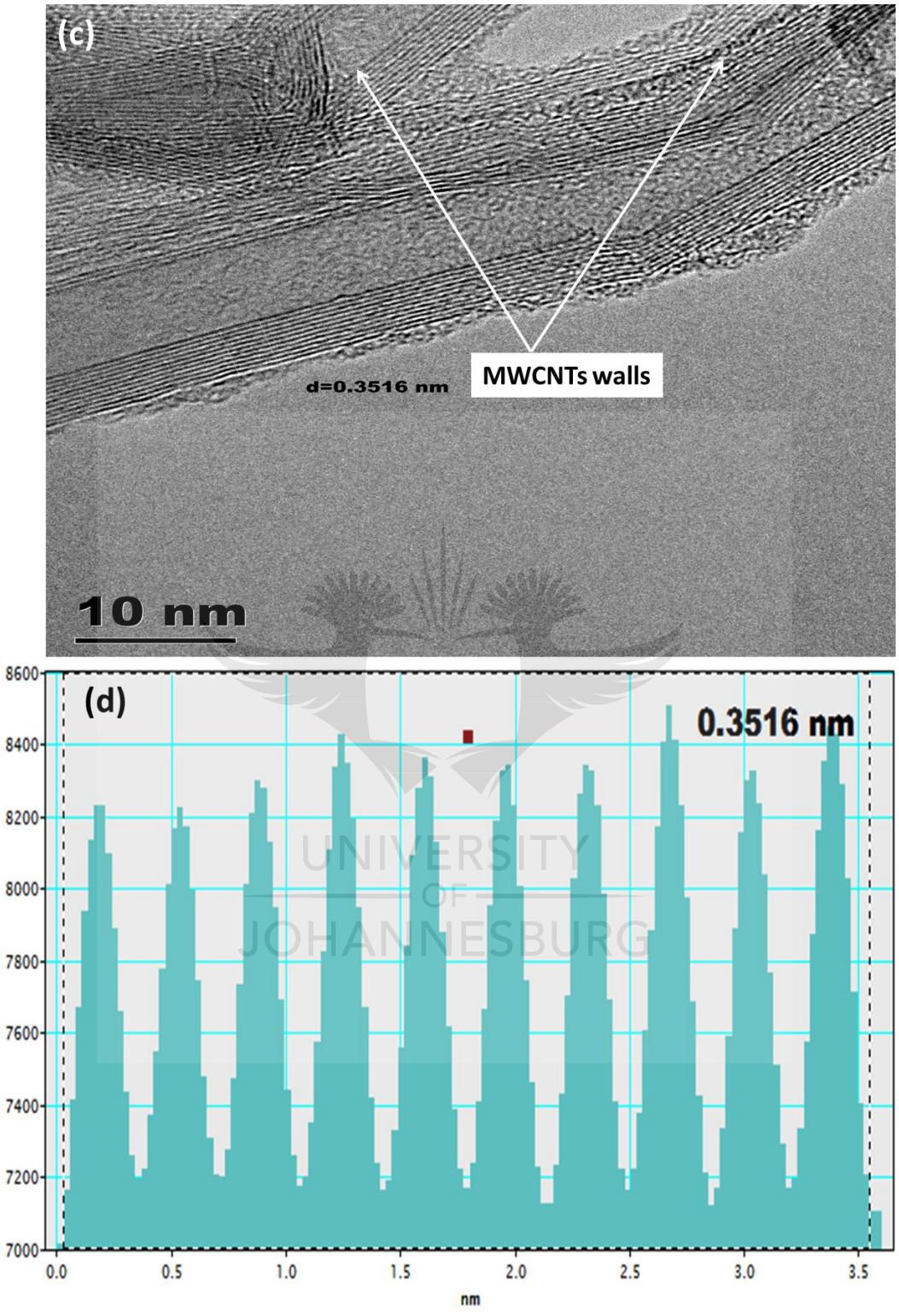

Figure 4.9. HRTEM of the milled NiAl-1wt% MWCNTs, HEBM 2 hours: (a) SAED pattern, (b) Image of nanotubes (c)MWCNTs walls, and (d) FFT.

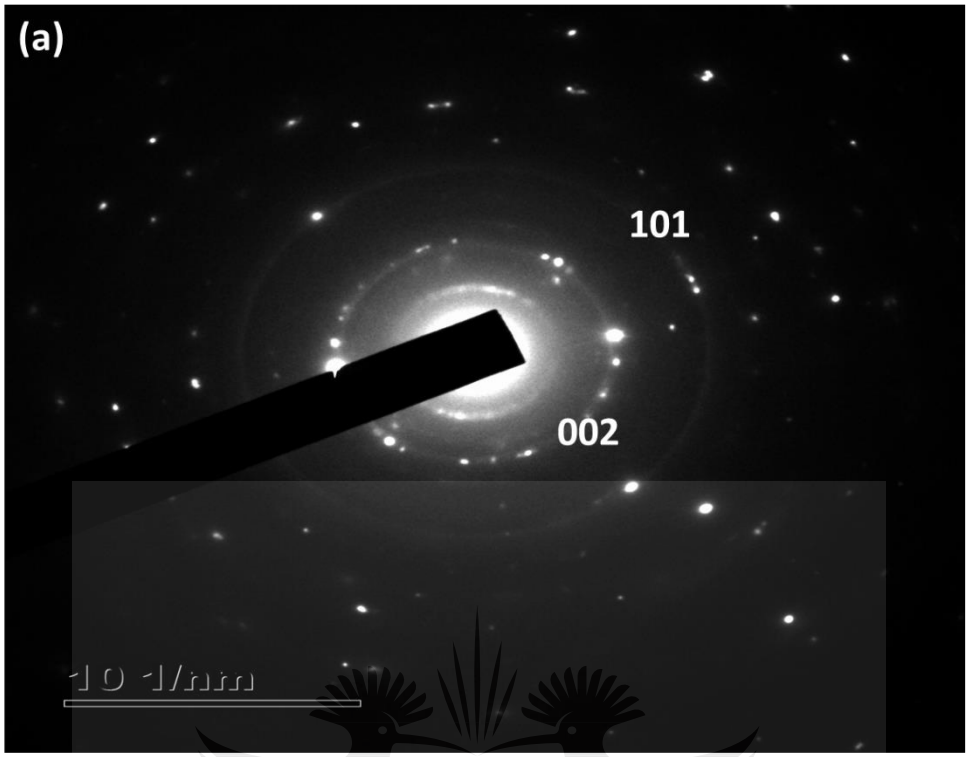
(a)
101
002
10 1/nm

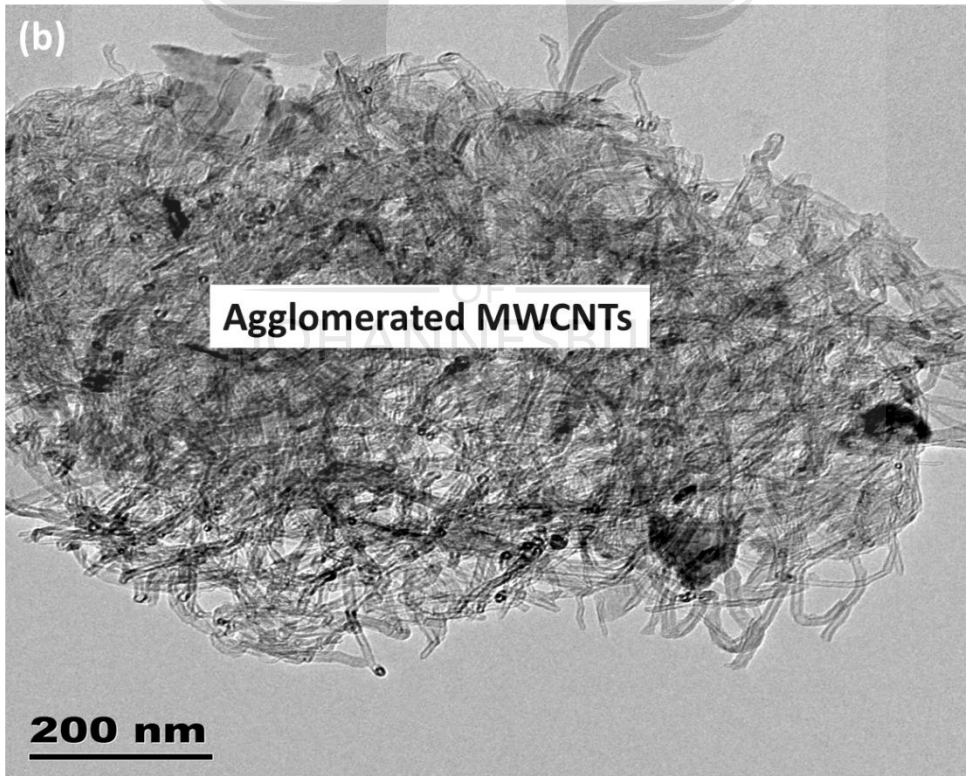
(b)
Agglomerated MWCNTs
200 nm

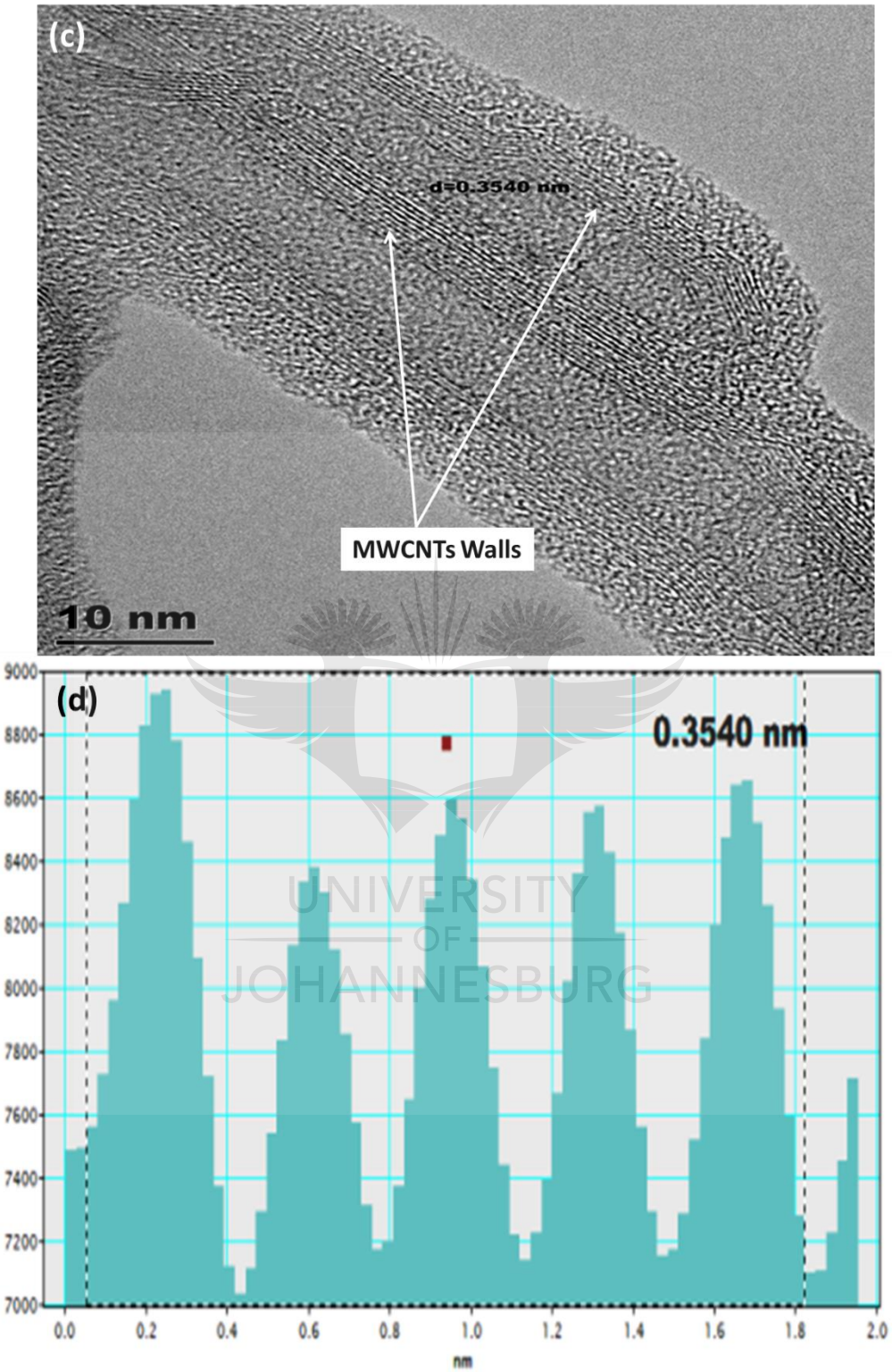

Figure 4.10. HRTEM of milled NiAl-1wt% MWCNTs, HEBM 3 hours: (a) SAED pattern, (b) image of the nanotubes (c) MWCNTs walls, and (d) FFT.

4.4 SUMMARY

Chapter four discussed the synthesis of the milled powders obtained by using the planetary ball milling process. The morphology, composition and the structural integrity of the powders were observed using the SEM, XRD and Raman spectroscopy. The SEM images revealed a relative dispersion and agglomerations of MWCNTs in the composites. The XRD confirms the formation of NiAl peaks as the dominant peak and the Raman spectra revealed I_D/I_G ratio of the composites. This ratio depicts the structural integrity of the MWCNTs within the NiAl and it decreased with prolonged milling. The dispersion level of MWCNTs in NiAl matrix was analyzed using the TEM and this revealed the presence of dislocations in form of streaks and spots in the composites. The role of impact energy from the ball milling process is very significant in overpowering the Van der Waals forces in nanotubes, to ensure good dispersion. However, the mechanical energy observed from this investigation resulted into strains on the structure of the nanotubes, supposedly due to the overpowering effect of the Van der Waals forces on the impact energy.

CHAPTER FIVE

5 RESULTS AND DISCUSSION ON THE SINTERING CHARACTERISTICS OF MILLED MWCNTs INTO NiAl

In this chapter, the characterization of the consolidated NiAl and NiAl-1wt% MWCNTs composites at varied heating rates between 50-150 ^{o}C/min was carried out to determine the microstructures, structural changes and the crystallographic orientations. The microstructures of the consolidated samples were examined using the SEM, the phase identification of the samples was carried out with the XRD, and the grain analysis of the consolidated samples were also determined using the SEM-EBSD detector. The micrographs and XRD patterns are presented below.

5.1 MICROSTRUCTURES OF THE CONSOLIDATED SAMPLES

Figure 5.1 represents the SEM microstructures of the consolidated NiAl at the heating rates of 50 ^{o}C/min, 100 ^{o}C/min, and 150 ^{o}C/min. From Figure 5.1(a), the microstructure of the consolidated NiAl with the heating rate of 50 ^{o}C/min revealed the presence of pores (indicated with white arrows). A similar microstructure was observed when the heating rate was increased to 100 ^{o}C/min (Figure 5.1(b), but there were more pores in the specimen. The microstructure of the consolidated NiAl at the heating rate of 150 ^{o}C/min showed limited pores (Figure 5.1(c). It was observed that the porosity of the consolidated NiAl increased from 50 ^{o}C/min to 100 ^{o}C/min, and afterwards, there was a decrease in the porosity for the consolidated NiAl at the heating rate of 150 ^{o}C/min (this sample showed the least porosity among the consolidated NiAl). This suggests that higher heating rate resulted into more interparticle bonding of the powder, thereby ensuring the closure of pores. Figure 5.1(d-l) shows the SEM morphologies of the consolidated NiAl-MWCNTs composites (HEBM, 1 hour, 2 hours, and 3 hours). The morphologies of the consolidated NiAl-

MWCNTs composites (HEBM, 1 hour), at the heating rates of 50, 100, and 150 ^{o}C/min is represented in Figure 5.1(d-f). The microstructure displayed the presence of porosity which increased from the heating rate of 50 ^{o}C/min to 150 ^{o}C/min. Also, the images of the consolidated NiAl-MWCNTs composites (HEBM, 2 hours) were presented in Figure 5.1(g-i) with the evidence of porosity, which increased from the heating rate of 50 ^{o}C/min to 150 ^{o}C/min. The same trend was observed in the consolidated NiAl-MWCNTs composites (HEBM, 3 hours), as shown in Figure 5.1(j-l). All the consolidated NiAl-MWCNTs composites showed similar trend of microstructures after SPS. In the course of sintering process, various mechanisms takes place which include localized and bulk deformation of particles, thermal and non-thermal effects, and particle re-arrangement, that affects the densification behaviour (Cavaliere *et al.*, 2017). Hence, influencing the properties and microstructure of the bulk-sample (Cavaliere *et al.*, 2017). It was observed from this study that the porosity of the consolidated composites increased with the heating rates. At the heating rate of 150 ^{o}C/min, more porosity was observed in the microstructure of the composites. This trend was obviously different from the consolidated NiAl, the observed porosity decreased at the heating rate of 150 ^{o}C/min. This suggests that the presence of retained MWCNTs agglomerates (indicated with white arrows) may have influenced the increase in porosity observed in the composites from 50 to 150 ^{o}C/min due to the ball milling process. Furthermore, MWCNTs agglomerates may inhibit the diffusion of particle, hinder sinterability and delay sintering kinetics during consolidation (Wichmann *et al.*, 2008).

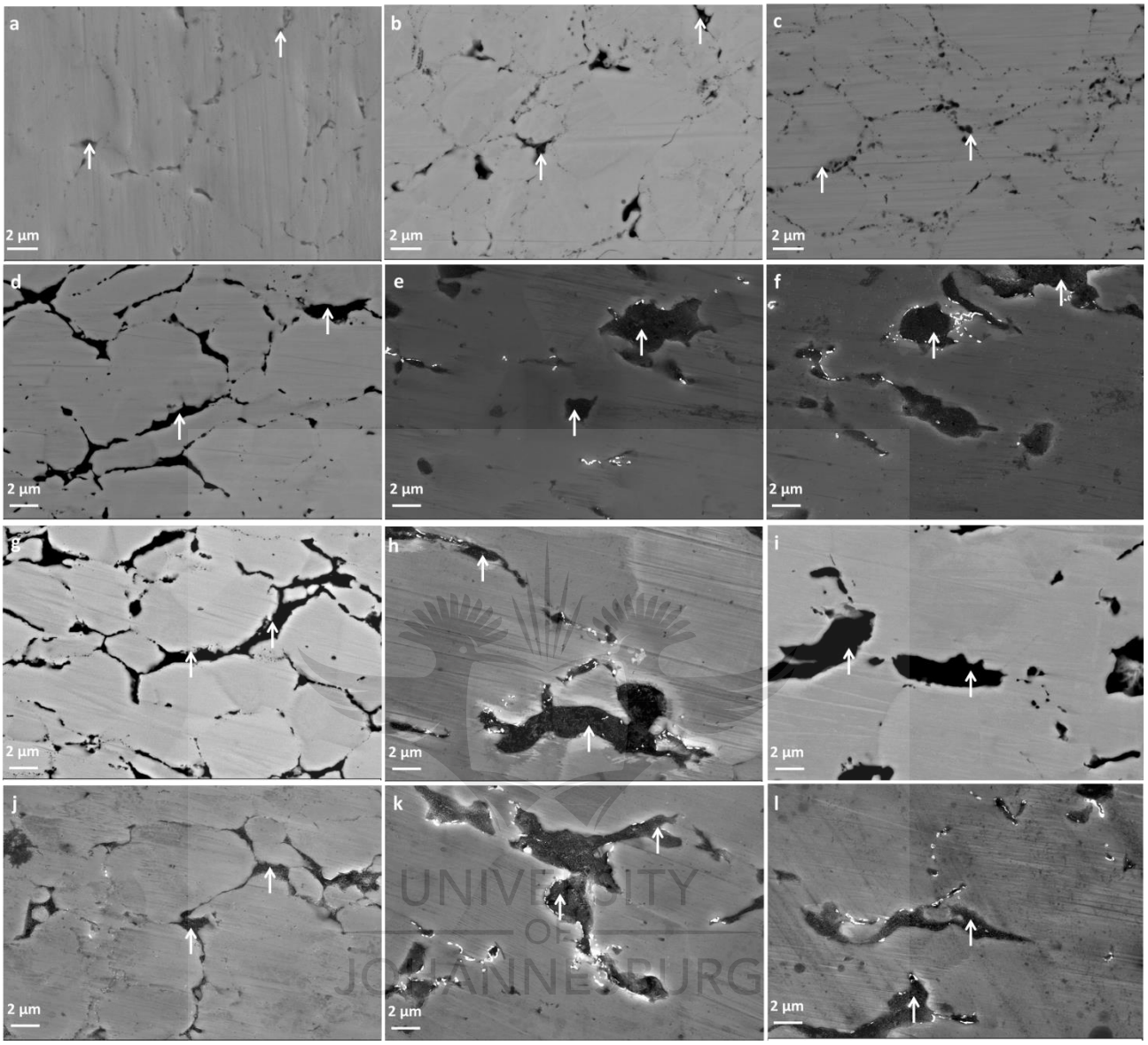

Figure 5.1: Illustrations of the SEM morphologies of the sintered NiAl and composites: (a) 50 ^{o}C/min, (b) 100 ^{o}C/min, and (c) 150 ^{o}C/min, (d) NiAl-MWCNTs/ 1h at 50 ^{o}C/min, (e) NiAl-MWCNTs/ 1h at 100 ^{o}C/min, (f) NiAl-MWCNTs/ 1h at 150 ^{o}C/min, (g) NiAl-MWCNTs/ 2h at 50 ^{o}C/min, (h) NiAl-MWCNTs/ 2h at 100 ^{o}C/min, (i) NiAl-MWCNTs / 2h at 150 ^{o}C/min, (j) NiAl-MWCNTs/ 3h at 50 ^{o}C/min, (k) NiAl-MWCNTs/ 3h at 100 ^{o}C/min, and (l) NiAl-MWCNTs/ 3h at 150 ^{o}C/min.

5.2 XRD PATTERN OF THE CONSOLIDATED SAMPLES

Figure 5.2(a-d) represents the XRD patterns of all the consolidated samples at the heating rates of 50, 100, and 150 ^{o}C/min. The XRD pattern of the consolidated NiAl revealed NiAl peaks as the dominant peaks in the pattern (Figure 5.2(a). The consolidated NiAl-MWCNTs composites (HEBM, 1 hour, 2 hours and 3 hours) showed the presence of NiAl and NiC peaks respectively at the heating rates of 50, 100, and 150 ^{o}C/min. NiAl was observed at 2Θ = 30.6^{o}, 44.1^{o}, 54.76^{o}, 64.2^{o}, and 81.5^{o} which corresponds to the planes (100), (110), (111), (200), and (211). NiC was observed at 2Θ = 44.1^{o}, thus corresponding to the plane (111). Also, the intensity of the consolidated samples did not change as the heating rates increased.

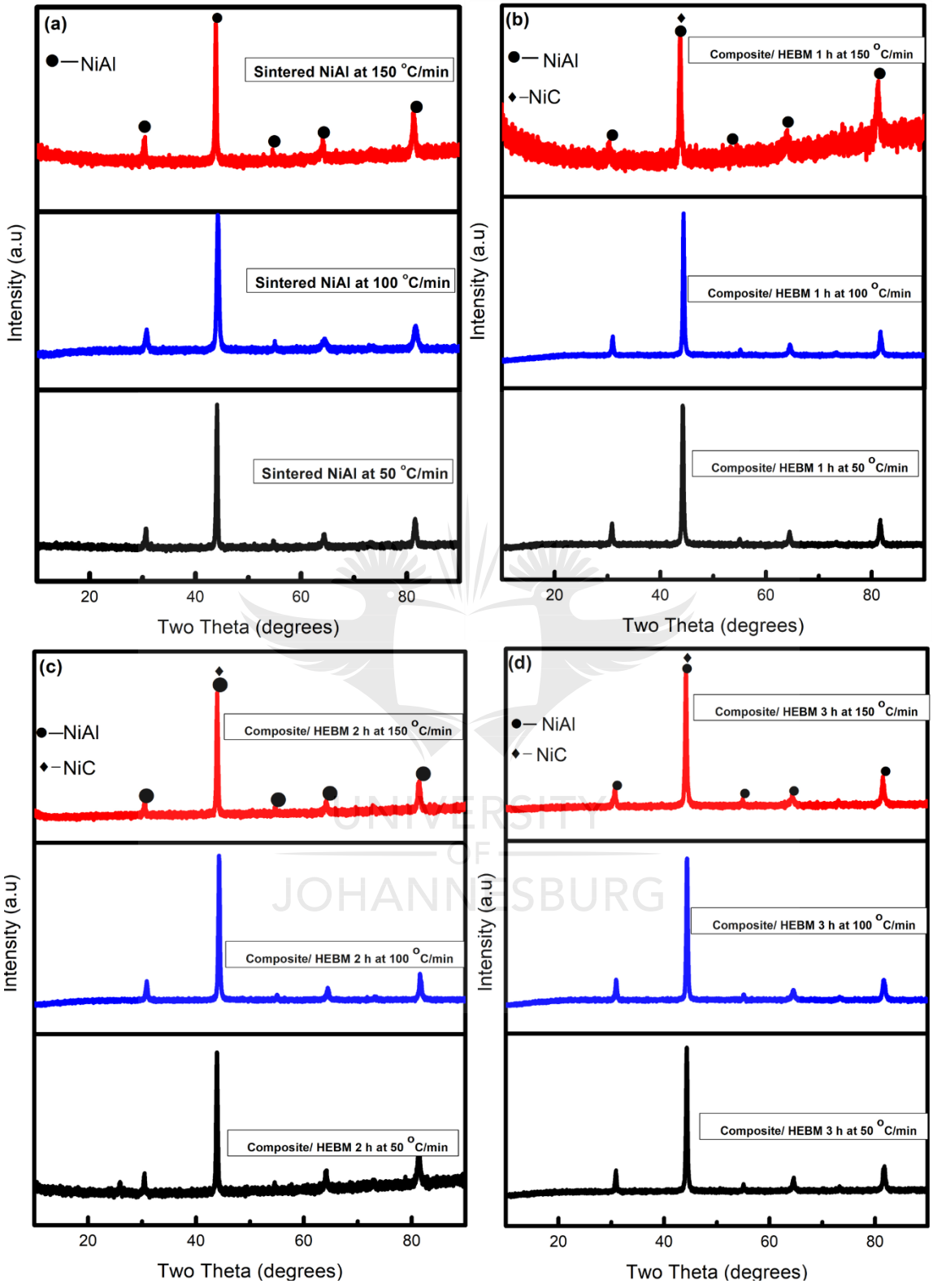

Figure 5.2. XRD pattern of all the consolidated samples at 50, 100, and150 °C/min.

5.3 FRACTURE MORPHOLOGY OF THE CONSOLIDATED SAMPLES

The fractured samples were obtained by using a precision cutter to make a small preliminary cut on the samples, and the samples were fractured on a bench vice with a hammer. Figure 5.3(a-c) depicts the fracture morphologies of the consolidated NiAl at the heating rates of 50, 100, and 150 ^{o}C/min. The fracture mode of the consolidated NiAl depicts the presence of river pattern which denotes brittle fractured surfaces. Figure 5.3(d-l) denotes the fracture morphologies of the consolidated NiAl-MWCNTs composites (HEBM, 1 hour, 2 hours, and 3 hours) at the heating rates of 50, 100, and 150 ^{o}C/min. The fracture mode of the consolidated composites revealed the presence of cavities (indicated with red arrow). Also, the fractured surfaces of the consolidated composites at the heating rates of 100, and 150 ^{o}C/min, were evident with the presence of dimple (pointed with yellow square). These are the characteristics of ductile fracture surfaces. The effect of heating rates was evident in the consolidated composites, which revealed the presence of more cavities as the heating rates were increased.

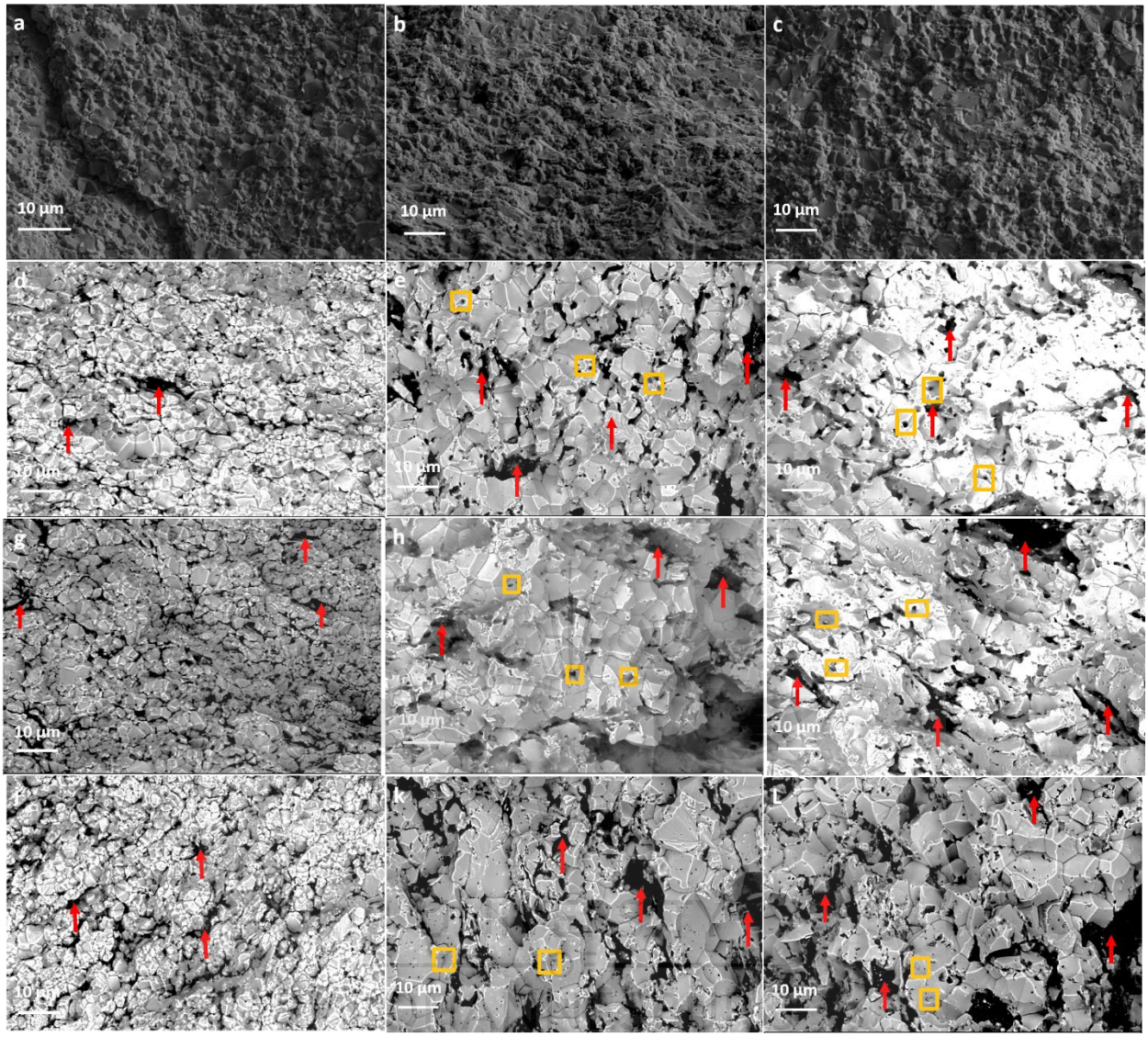

Figure 5.3. Fracture surfaces of the consolidated samples between the heating rates of 50-150 ^{o}C/min.

5.4 CRYSTAL ORIENTATIONS OF THE CONSOLIDATED SAMPLES

The crystal orientation of the consolidated NiAl and NiAl-MWCNTs composite (HEBM, 1 hour) was presented in Figure 5.4. The band contrast (BC) maps of the consolidated NiAl and NiAl-MWCNTs composite (HEBM, 1 hour) at the heating rates of 50, 100, and 150 ^{o}C/min were represented in Figure 5.4(a-f).

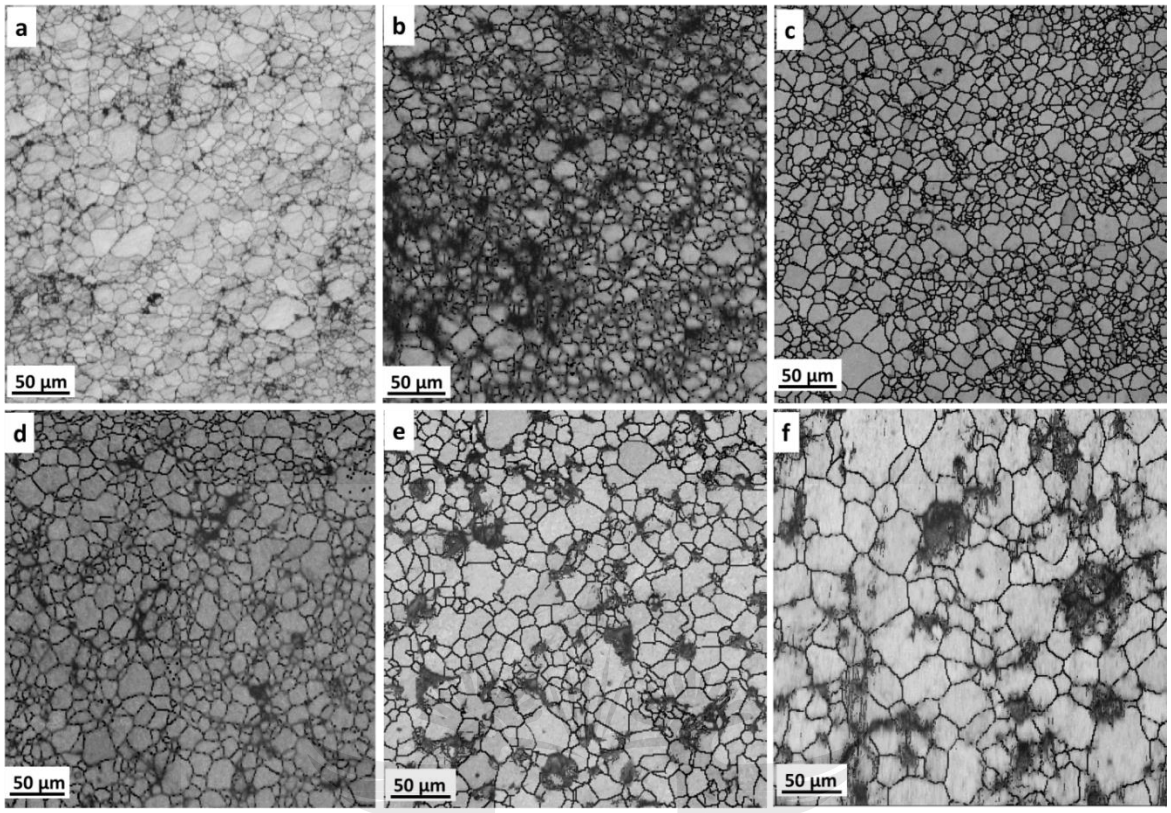

Figure 5.4. Band contrast maps of the sintered samples: (a) NiAl at 50 ^{o}C/min, (b) NiAl at 100 ^{o}C/min, (c) NiAl at 150 ^{o}C/min, (d) NiAl-MWCNTs at 50 ^{o}C/min, (e) NiAl-MWCNTs at 100 ^{o}C/min, and (f) NiAl-MWCNTs at 150 ^{o}C/min.

The BC maps were obtained from the electron backscattered patterns (EBSP) after indexing. From the BC maps, the grain boundaries were clearly observed, together with some black regions. These regions are referred as low-EBSP areas where the flamenco could not determine the phases present in the samples during indexing (Suárez *et al.*, 2014) . Furthermore, the BC map of the consolidated NiAl at the heating rate of 50 ^{o}C/min revealed few regions of low-EBSPs (Figure 5.4(a)). As the heating rate (100 ^{o}C/min) was increased, there were more low-EBSP regions on the BC map in Figure 5.4(b). Further increase in heating rate (150 ^{o}C/min) led to the decrease in the low-EBSP regions in Figure 5.4(c). The low-EBSPs in the consolidated NiAl may be ascribed to the presence of pores. The BC maps of the NiAl-MWCNTs composite (HEBM, 1 hour) revealed a different pattern from the consolidated NiAl. The low-EBSP region observed in the composite increased as

the heating rate was increased. This could be accredited to the regions of porosity where the retained MWCNTs agglomerates were located (Suárez *et al., 2*014).

The grain size maps of the consolidated NiAl and NiAl-MWCNTs composite (HEBM, 1 h) at the heating rates of 50, 100, and 150 ^{o}C/min respectively were presented in Figure 5.5(a-f). The grain size of the consolidated NiAl at the heating rates of 50, 100, and 150 ^{o}C/min was observed with similar crystal orientations. Moreover, the grain size of the NiAl-MWCNTs composite (HEBM, 1 h) was observed with a progressive increase in grain size as the heating rates increased, as illustrated in Figure 5.5(d-f). The consolidated NiAl-MWCNTs composite at the heating rate of 50 ^{o}C/min had better crystal orientations as compared to the other consolidated NiAl-MWCNTs composite. Although, a few numbers of researchers have reported a contrary view about the effect of rapid heating rates on grain size (Shen *et al.*, 2002; Aliyu *et al.*, 2015; Singh *et al.*, 2018). It was reported that rapid heating rate impedes surface diffusion for coarsening processes, thereby leading to the decrease in grain size. However, this study is in agreement with (Murayama & Shin, 2000). They reported that high heating rate results in grain growth because of high defect concentration formed during densification and rapid particle deformation.

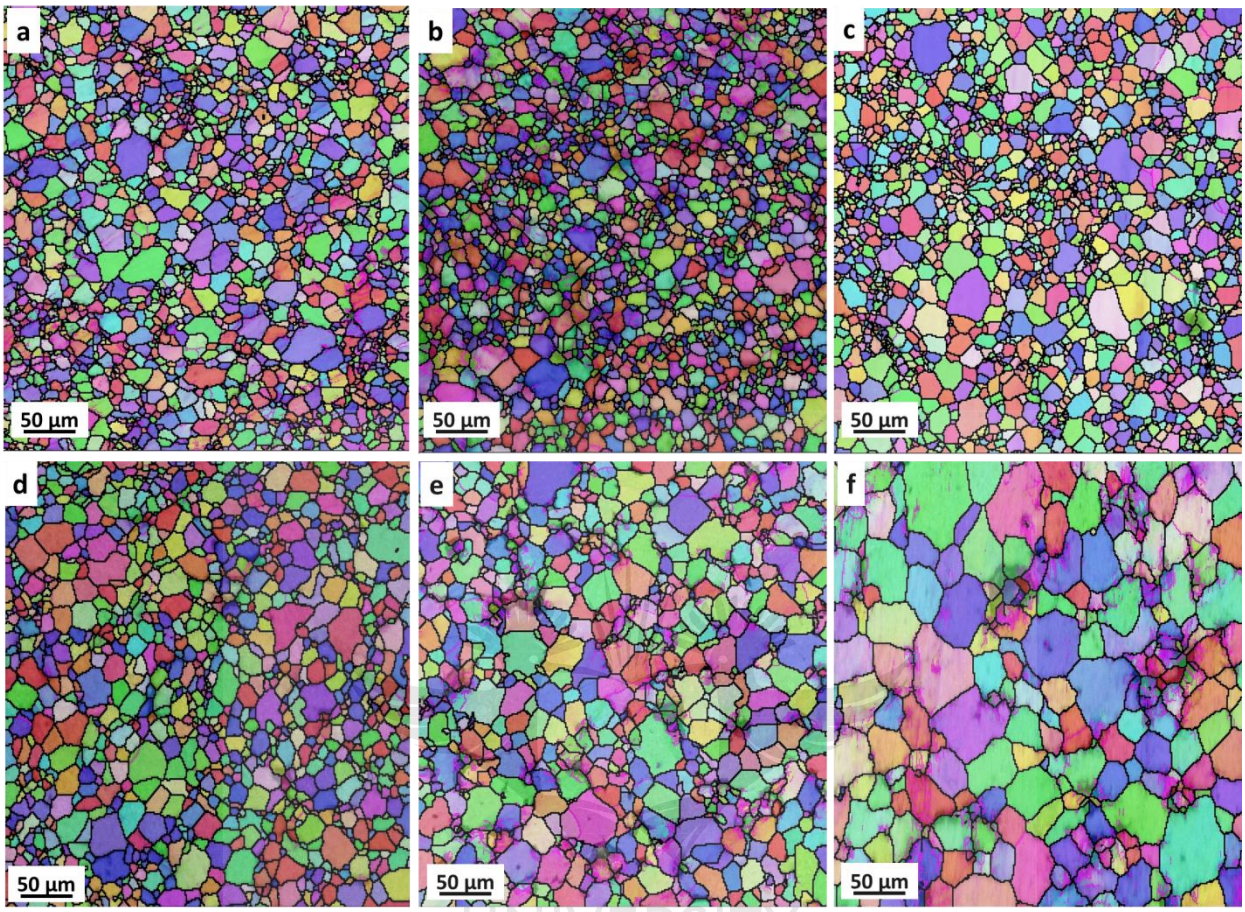

Figure 5.5. Grain size maps of the consolidated samples: (a) NiAl at 50 ^{o}C/min, (b) NiAl at 100 ^{o}C/min, (c) NiAl at 150 ^{o}C/min, (d) NiAl-MWCNTs at 50 ^{o}C/min, (e) NiAl-MWCNTs at 100 ^{o}C/min, and (f) NiAl-MWCNTs at 150 ^{o}C/min.

The mean grain size of the consolidated samples was evaluated using the linear intercept method, according to ASTM E112 (Conshohocken, 1996). The mean grain size (µm) of the consolidated at the heating rates of 50, 100, and 150 ^{o}C/min were measured as 3.24 ±2.5 µm, 3.14 ±2.1 µm, and 3.27 ±2.4 µm respectively. However, the mean grain size of the NiAl-MWCNTs composite (HEBM, 1 hour) at the heating rates of 50, 100, and 150 ^{o}C/min were measured as 3.93 ±2.5 µm, 4.78 ±3.4 µm, and 8.05 ±5.8 µm respectively. The mean grain size of the consolidated samples was illustrated by the plot of frequency distribution against the intercept length of the grains, as shown

in Figure 5.6(a-f) and the plot of the mean grain size of the consolidated samples was shown in Figure 5.7.

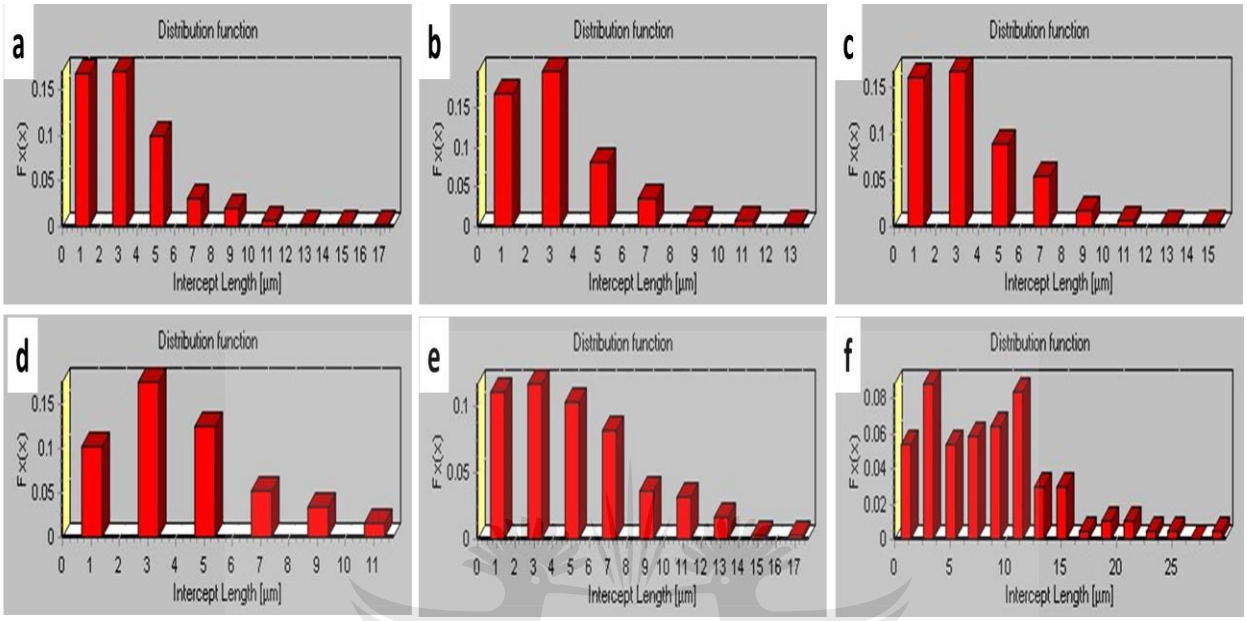

Figure 5.6. Grain size distribution of the consolidated samples: (a) NiAl at 50 ^{o}C/min, (b) NiAl at 100 ^{o}C/min, (c) NiAl at 150 ^{o}C/min, (d) NiAl-MWCNTs at 50 ^{o}C/min, (e) NiAl-MWCNTs at 100 ^{o}C/min, and (f) NiAl-MWCNTs at 150 ^{o}C/min.

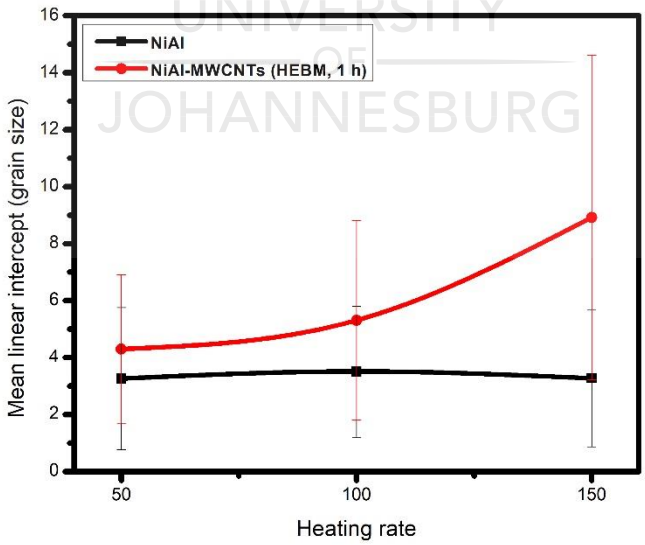

Figure 5.7. Plot of mean grain size of the consolidated samples at different heating rate.

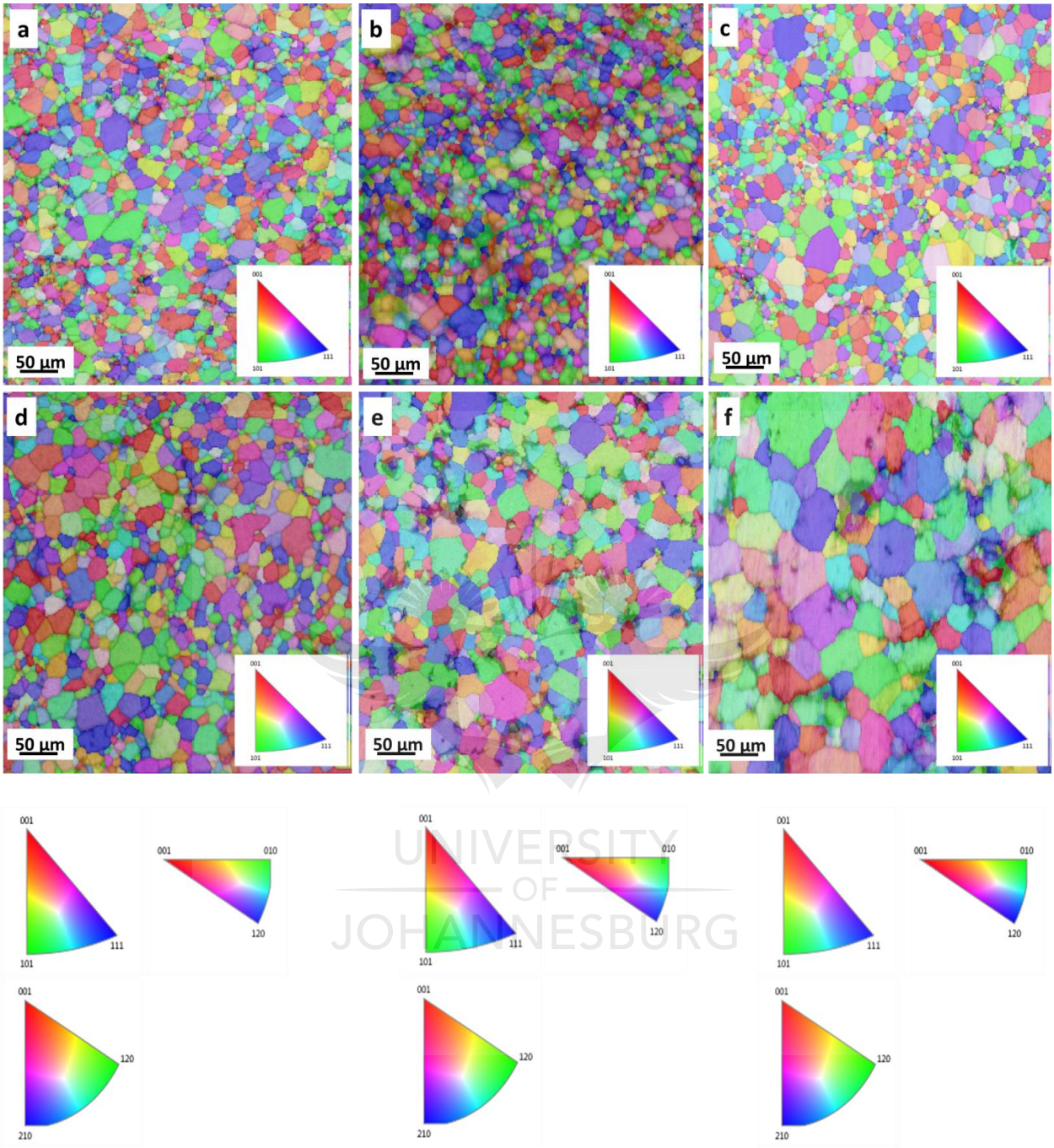

Figure 5.8. Inverse pole figure maps of the consolidated samples: (a) NiAl at 50 °C/min, (b) NiAl at 100 °C/min, (c) NiAl at 150 °C/min, (d) NiAl-MWCNTs at 50 °C/min, (e) NiAl-MWCNTs at 100 °C/min, and (f) NiAl-MWCNTs at 150 °C/min.

The inverse pole figure (IPF) maps show the alignment of the crystal directions with the consolidated samples axes at different heating rates, and it further predicts the texture of a sample.

The grain colours illustrates the crystal orientations, which indicates no predominance of any colour. This suggests that the consolidated NiAl and NiAl-MWCNTs composite (HEBM, 1 hour) at the heating rates of 50, 100, and 150 ^{o}C/min does not have texture or show the intensity of any colour (Simões *et al.*, 2014). The features observed in the IPF maps revealed that grain size increases with increasing heating rate amongst the consolidated composite, but there is no significant grain increase in the consolidated NiAl (Figure 5.8). The pole figure (PF) maps show the arrangement of the crystal directions relative to the consolidated samples (Figure 5.9). The maps were obtained using the complete data set with equal area projection and upper hemisphere. The cluster size and half width of the maps were set at 5^{o} and 10^{o} and the multiple of uniform density (MUD) values showed the region with maximum and minimum intensity. The red region depicts higher MUD and the blue region shows lower MUD (Figure 5.9), although the scales may differ (Ruzicka & Hugo, 2018). The map of the PF of all the consolidated samples shows no evidence of texture.

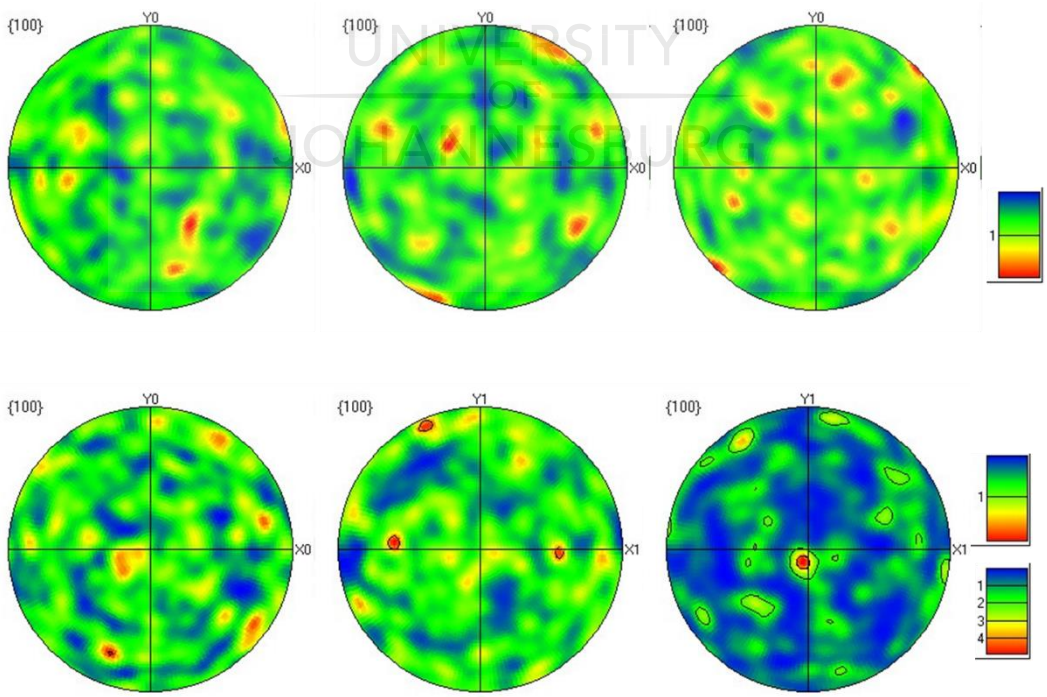

Figure 5.9. Pole figure maps of the consolidated samples: (a) NiAl at 50 ^{o}C/min, (b) NiAl at 100 ^{o}C/min, (c) NiAl at 150 ^{o}C/min, (d) NiAl-MWCNTs at 50 ^{o}C/min, (e) NiAl-MWCNTs at 100 ^{o}C/min, and (f) NiAl-MWCNTs at 150 ^{o}C/min.

5.5 SUMMARY

Chapter five discussed the characterization of all the consolidated samples. The SEM micrograph of the consolidated NiAl revealed the presence of pores in their grain boundaries and the consolidated composites also showed the presence of re-agglomerated MWCNTs. It was observed that the retained MWCNTs agglomerates increased when the heating rate was increased. The fracture surfaces of the consolidated NiAl revealed a brittle surface while the consolidated composites revealed a ductile surface. The grain size of the consolidated composites increased as the heating rate was increased. The grain size of all the consolidated samples showed no formation of texture.

CHAPTER SIX

6 RESULTS AND DISCUSSION ON THE MECHANICAL AND TRIBOLOGY PROPERTIES OF CONSOLIDATED MWCNTs REINFORCED NiAl

This chapter presents the mechanical and tribology analysis of the consolidated NiAl and NiAl-MWCNTs composite (HEBM, 1 hour, 2 hours and 3 hours) at the heating rates of 50, 100, and 150 ^{o}C/min. The densification mechanisms were analyzed using the SPS data and the relative density was calculated in accordance to the Archimedes' principle. The hardness value of the consolidated samples was obtained from the microhardness tester. Furthermore, the nanoindentation data was used to determine the nanohardness and elastic modulus of the consolidated samples. The coefficient of friction value of the sintered samples was obtained from the data retrieved from the tribometer.

6.1 DENSIFICATION MECHANISMS OF THE CONSOLIDATED SAMPLES

The sintering profile obtained from the SPS was used to assess the densification behaviour of consolidated NiAl and NiAl-MWCNTs composites (HEBM, 1 hour, 2 hours, and 3 hours) at the heating rates of 50, 100, and 150 ^{o}C/min. The temperature against time, displacement against time and shrinkage rate against time curves were analyzed. From Figure 6.1(a-c), the temperature against time plots of all the consolidated samples were illustrated. The sintering process started with chamber vacuuming, and afterwards pressure was exerted, which aids the powder compaction between the first 9 minutes at a constant temperature. At 250 ^{o}C, current was supplied to the system and a progressive heating of the powder occurred at a constant pressure of 50 MPa. The powder was completely heated at 1000 ^{o}C, held for 10 min (isothermal hold) and the powder was cooled at room temperature. From Figure 6.1(a), the consolidated samples at the heating rate of 50 ^{o}C/min had enough time for uniform heating and pressure to take place. This may be the reason for the

good densification observed in the sintered samples at 50 ^{o}C/min. As soon as the heating rate was increased to 100 ^{o}C/min (Figure 5.4(b)), the time employed to complete the sintering cycle was reduced and further increase in the heating rate at 150 ^{o}C/min (in Figure 6.1(c)), resulted to the decrease in the sintering cycle. The sintering profile of the consolidated NiAl at this heating rate exhibits a different pattern from the consolidated composites. It could be seen that the sintering operation began very late; this may be because of the pressure at the early stage of the powder compaction.

The displacement of the consolidated samples between the upper and lower sintering punches at various heating rates were presented in Figure 6.1(d-f). The relative displacement against time curve of the consolidated samples at the heating rate of 50 ^{o}C/min, was shown in Figure 6.1(d). From 0-0.48 mm after sintering for the period of 9 min, the displacement of the consolidated NiAl was evident at the early sintering stage, which may be due to the impact of pressure exerted on the powder (green compact), even though the temperature is very low to effect the punch displacement. From 0.48- 1.49 mm, the displacement of the punch was rapid at the period of 14 min due to the progressive rise in temperature, which softens the compact and led to the surface activation and particle re-arrangement of NiAl sample. This was followed by the escape of gases from the compact, then the displacement was steady with increasing sintering time (Bonifacio *et al.,* 2012). At the period of 23 min, a rapid displacement between the punches were noticed from 1.49-2.25 mm, which resulted into particle necking and neck growth as the temperature increases due to evaporation and condensation (Zhang *et al.,* 2010). This process resulted to the physical structural change of the compact (thermal softening) which led to grain re-shaping and smoothening (Falodun *et al.,* 2018). A further increase was observed in the displacement from 2.25-2.31 mm during the isothermal hold of 10 min, where maximum densification was attained by the sample.

This was followed by a snap rise in displacement as a result of shrinkage when the sample experienced cooling.

The displacement of consolidated NiAl-MWCNTs composite (HEBM, 1 hour, 2 hours, and 3 hours) at the heating rate of 50 ^{o}C/min had similar displacement behaviour with consolidated NiAl. All the sintering stages observed in the consolidated NiAl was also noticeable in the sintered composites (Zhaohui *et al.,* 2008; Diouf & Molinari, 2012). The relative displacements of the consolidated composites increased due to the pressure exerted on the compact, a steady displacement was evident at lower temperature. At this stage, the sintering mechanism was retarded because of the presence of MWCNTs which generated pores in the matrix powder. Furthermore, a rapid displacement was noticed when the temperature was increased due to thermal softening, thereby resulting to densification. This phenomena was also observed from the results reported by Okoro *et al.,* (2019). Similarly, the relative punch displacement of all the consolidated samples at the heating rates of 100 ^{o}C/min and 150 ^{o}C/min showed the same pattern with the consolidated sample at 50 ^{o}C/min, although sintering activity at a stage may be early or delayed, short or extended for the consolidated samples. Comparatively, the effect of heating rate on the consolidated samples was observed in the displacement against time curves. The displacement of the punches of the consolidated NiAl decreased as the heating rate was increased from 50 ^{o}C/min to 100 ^{o}C/min. Further increase in the heating rate (150 ^{o}C/min), resulted in higher displacement as observed in Figure 6.1(f). Conversely, the displacement of the consolidated composites decreased as the heating rate was increased from 50 ^{o}C/min to 150 ^{o}C/min. This may be attributed to the presence of porosity in the composites which increases as the heating rate was increased, thereby retarding the sintering mechanism. This was revealed by the SEM images in Figure 5.1.

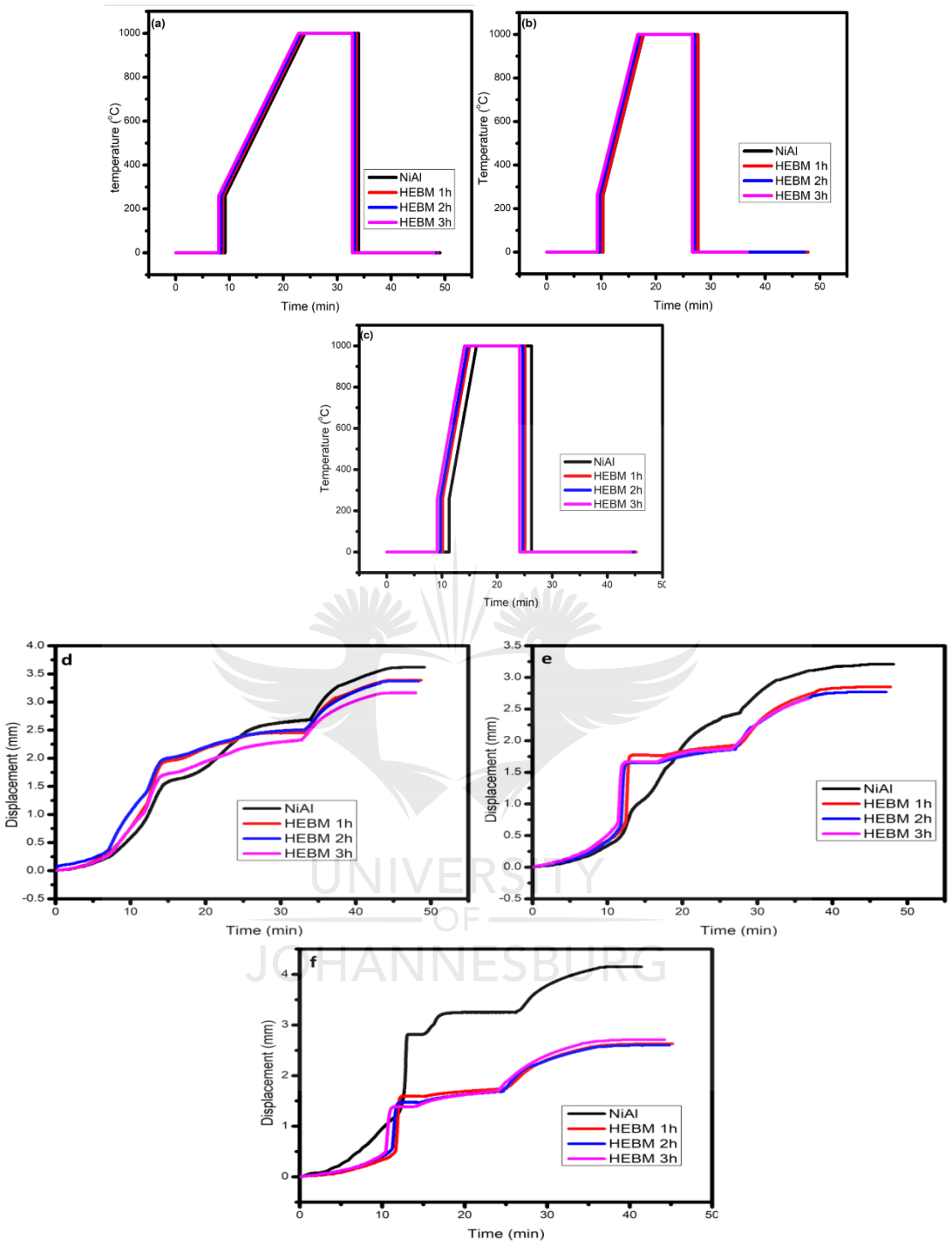

Figure 6.1. Illustration of the temperature against time curves: (a) 50 °C/min, (b) 100 °C/min, (c) 150 °C/min and displacement against time curves of the consolidated samples: (d) 50 °C/min, (e) 100 °C/min, and (f) 150 °C/min.

6.2 DISPLACEMENT OF THE PUNCHES AGAINST TEMPERATURE

The effect of heating rates was also investigated on the displacement of the punches against temperature of all the consolidated samples. Figure 6.2(a) indicates the consolidated samples at the heating rate of 50 ^{o}C/min. The relative displacement of the consolidated NiAl was observed from 0-0.48 mm, due to the impact of pressure exerted on the powder (green compact), even though the temperature is very low to impact the punch displacement. It increased when the temperature was above 250 ^{o}C, which softens the compact and led to the surface activation and particle re-arrangement sample. The displacement further increased at 511 ^{o}C, which resulted into particle necking and neck growth as the temperature increases due to evaporation and condensation (Zhang *et al.*, 2010). The displacement was constant, and it increased with the temperature between 511 ^{o}C to 1000 ^{o}C. This process resulted to the physical structural change of the compact (thermal softening) which led to grain re-shaping and smoothening (Falodun *et al.*, 2018). At 1000 ^{o}C, the sample was held for 10 min, and a further increase was observed in the displacement. At this stage, maximum densification was achieved, and it was followed by a snap rise in displacement as a result of shrinkage during cooling. The displacement of the consolidated composites at 50, 100, and 150 ^{o}C/min had the same trend with the consolidated NiAl, but the presence of MWCNTs which generated pores may have retarded the sintering mechanism. The displacement of the punches of the consolidated NiAl decreased as the heating rate was increased from 50 ^{o}C/min to 100 ^{o}C/min. Further increase in the heating rate (150 ^{o}C/min), resulted in higher displacement as observed in Figure 6.2(c). Also, the displacement of the consolidated composites decreased as the heating rate was increased from 50 ^{o}C/min to 150. This may be attributed to the presence of porosity in the composites which increases as the heating rate was increased, thereby retarding the sintering mechanism.

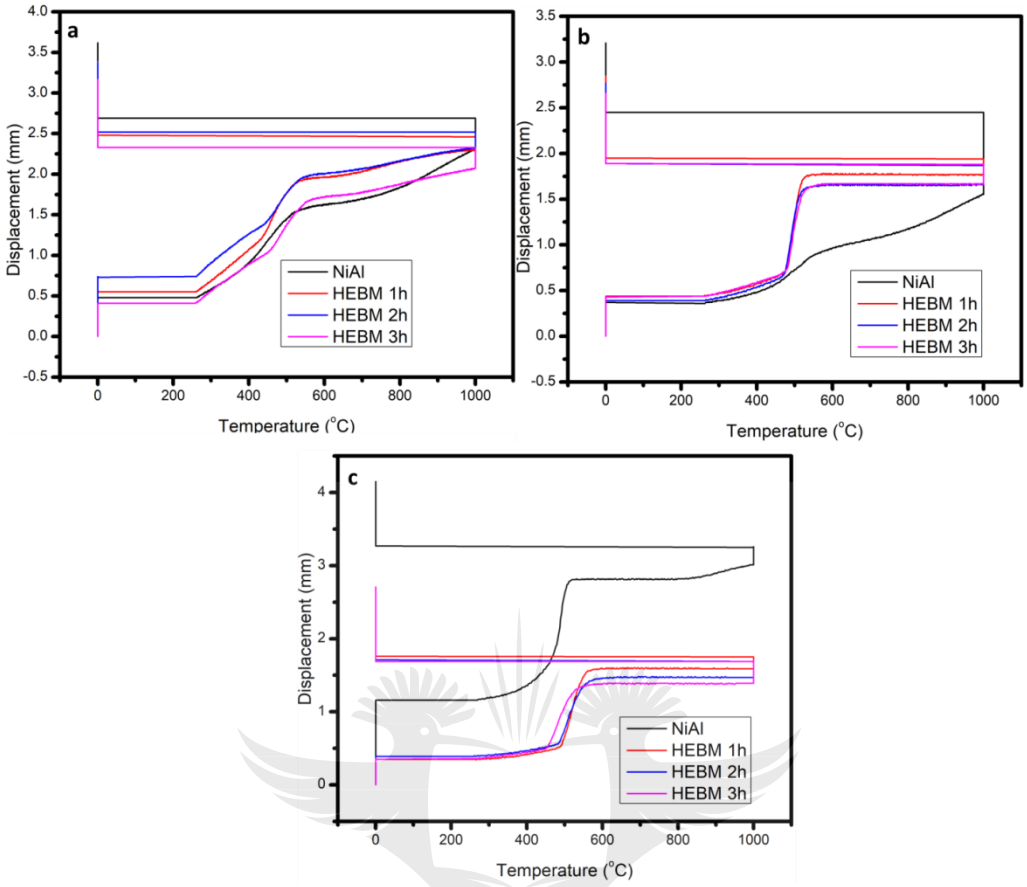

Figure 6.2. Displacement against temperature curves of the consolidated samples: (a) 50 °C/min, (b) 100 °C/min, and (c) 150 °C/min.

6.3 RELATIVE DENSITY OF THE CONSOLIDATED SAMPLES

The relative densities of the consolidated NiAl and NiAl-MWCNTs composites (HEBM, 1 hour, 2 hours, and 3 hours) at the heating rates of 50, 100, and 150 °C/min were presented in Table 6.1. The consolidated NiAl with the heating rate of 50 °C/min had the relative density of 94.9%, and the consolidated NiAl with the heating rate of 100 °C/min had the relative density of 90.8%. This indicates a sharp drop in relative density, may be due to the presence of more porosity in the consolidated sample at 100 °C/min. At the heating rate of 150 °C/min, it was observed with the RD of 96.2%. This demonstrates a sharp increase in RD, which is also traceable to the reduced pores observed in the sample. At higher heating rate, the pores of the consolidated NiAl were reduced.

The consolidated NiAl-MWCNTs composite (HEBM, 1 hour) at the heating rate of 50 ^{o}C/min had the relative density of 95.8%, and the consolidated composite with the heating rate of 100 ^{o}C/min had the relative density of 88.5%. Furthermore, the composite was found with the relative density of 86.2% at the heating rate of 150 ^{o}C/min. The trend shows that the relative density decreased with increasing heating rate, possibly due to the formation of retained agglomerates in the composite, which creates pores and further increase as the heating rate increased. This can be corroborated by the SEM images in Figure 5.1.

The consolidated NiAl-MWCNTs composite (HEBM, 2 hours) at the heating rate of 50 ^{o}C/min had the relative density of 94.5%, and the consolidated composite with the heating rate of 100 ^{o}C/min had the relative density of 88.2%. Also, the composite was found with the relative density of 85.5% at the heating rate of 150 ^{o}C/min. The consolidated NiAl-MWCNTs composite (HEBM, 3 hours) at the heating rate of 50 ^{o}C/min had the relative density of 92.3%, and the consolidated composite with the heating rate of 100 ^{o}C/min had the relative density of 88.1%. Furthermore, the composite was found with the relative density of 88.7% at the heating rate of 150 ^{o}C/min. The relative density of the consolidated composites followed the same trend with consolidated composite (HEBM, 1 hour). The plot of the relative densities was shown in Figure 6.3. The relative density of the consolidated composites at the heating rate of 50 ^{o}C/min was slightly higher than the composites at the heating rates of 100, and 150 ^{o}C/min respectively because of the enough time utilized for the occurrence of homogeneous pressure and heating during consolidation. Also, at lower heating rate, enough power input for particle bonding takes place. This is different in the case of high heating rate, minute time is used for particle binding because rapid particle heating occurs at a short time (Guo *et al.*, 2010; Snyder *et al.*, 2012). The consolidated composite (HEBM, 1 hour) at the heating

rate of 50 °C/min revealed the best RD of among the composite, supposedly due to relative dispersion of MWCNTs in the NiAl matrix as shown in Figure 4.4.

Table 6.1: Sintering parameters and relative density

Sample	Heating rate (°C/min	Relative density (%)	Sintering temp. (°C)
NiAl	50	94.9	1000
NiAl	100	90.8	1000
NiAl	150	96.2	1000
HEBM 1 h	50	95.8	1000
HEBM 1 h	100	88.5	1000
HEBM 1 h	150	86.2	1000
HEBM 2 h	50	94.5	1000
HEBM 2 h	100	88.2	1000
HEBM 2 h	150	85.8	1000
HEBM 3 h	50	92.3	1000
HEBM 3 h	100	88.1	1000
HEBM 3 h	150	88.7	1000

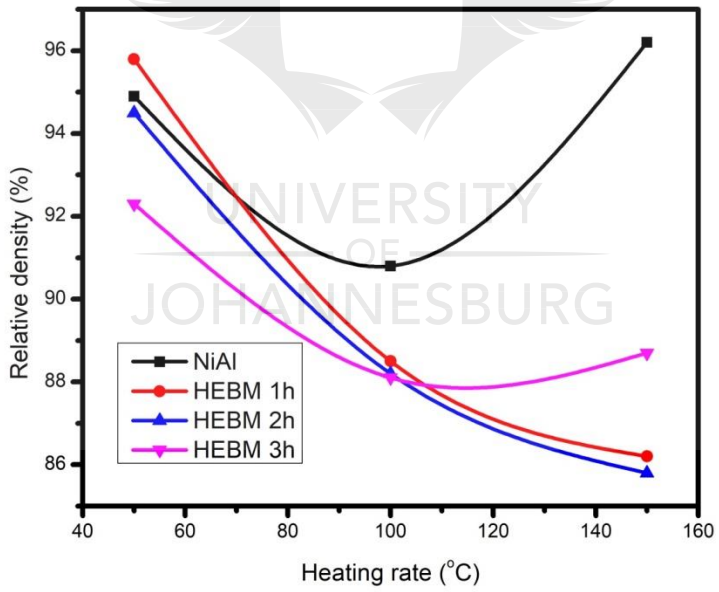

Figure 6.3. Plot of the relative densities of the consolidated samples at different heating rates.

6.4 HARDNESS PROPERTY OF THE CONSOLIDATED SAMPLES

The microhardness of the consolidated NiAl and NiAl-MWCNTs composites (HEBM, 1 hour, 2 hours, and 3 hours) at the heating rates of 50, 100, and 150 °C/min were presented in Figure 6.4.

The consolidated NiAl with the heating rate of 50 ^{o}C/min had the microhardness of 380.8 HV, and the consolidated NiAl with the heating rate of 100 ^{o}C/min had the microhardness of 327.4 HV. This indicates a sharp drop in microhardness, this is traceable to the decrease in density due to the presence of more porosity in the consolidated sample at 100 ^{o}C/min. At the heating rate of 150 ^{o}C/min, it was observed with the microhardness of 413.9 HV. This demonstrates a sharp increase in microhardness, which is also traceable to the reduced pores and high density observed in the sample. The consolidated NiAl-MWCNTs composite (HEBM, 1 hour) at the heating rate of 50 ^{o}C/min had the microhardness of 311.4 HV, and the consolidated composite with the heating rate of 100 ^{o}C/min had the microhardness of 293.1 HV. Furthermore, the composite was found with the microhardness of 264.6 HV at the heating rate of 150 ^{o}C/min. The trend shows that the microhardness decreased with increasing heating rate, possibly due to the decrease in density of the composite which arises from porosity.

The consolidated NiAl-MWCNTs composite (HEBM, 2 hours) at the heating rate of 50 ^{o}C/min had the microhardness of 287.3 HV, and the consolidated composite with the heating rate of 100 ^{o}C/min had the microhardness of 275.1 HV. Also, the composite was found with the microhardness of 259.5 HV, at the heating rate of 150 ^{o}C/min. The consolidated NiAl-MWCNTs composite (HEBM, 3 hours) at the heating rate of 50 ^{o}C/min had the microhardness of 283.9 HV, and the consolidated composite with the heating rate of 100 ^{o}C/min had the microhardness of 267.0 HV. Furthermore, the composite was found with the microhardness of 281.5 HV at the heating rate of 150 ^{o}C/min. The microhardness of the consolidated composites followed the same trend with consolidated composite (HEBM, 1 hour). The microhardness of the consolidated samples at different heating rates had similar trend with the relative density of the consolidated samples. Thus, it decreased as the heating rate was increased, which implies that as the porosity increases, the

relative density and hardness of the composites were decreased. The microhardness of the consolidated NiAl at different heating rates were observed to be higher than the consolidated composites, despite the addition of MWCNTs to the NiAl matrix. MWCNTs possesses excellent mechanical properties which enhanced metal matrices. From this study, the microhardness of the consolidated composites observed may be ascribed to the presence of nanotubes agglomerations due to the ball milling process.

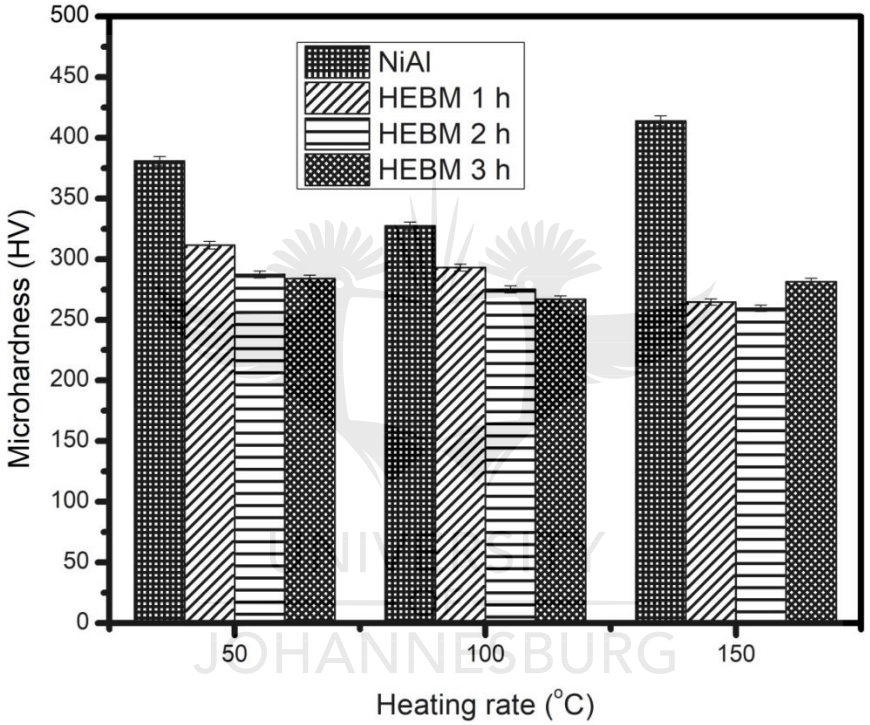

Figure 6.4. Vickers microhardness of all the consolidated samples.

6.5 NANOINDENTATION ANALYSIS OF THE CONSOLIDATED SAMPLES

The mechanical properties of the consolidated NiAl and NiAl-MWCNTs composites (HEBM, 1 hour, 2 hours, and 3 hours) at the heating rates of 50, 100, and 150 ^{o}C/min were analyzed using Oliver and Pharr approach (Oliver & Pharr, 2004). During the experiment, an indentation load of 75 mN was applied on the consolidated samples, no pop-in effects was recorded and the plots (loading and loading graph) were smooth. The load-displacement plots of the consolidated samples

at the heating rate of 50 ^{o}C/min was presented in Figure 6.5(a), the consolidated composite (HEBM, 2 hours) revealed the largest penetration depth at the load of 75 mN, accompanied by consolidated NiAl, consolidated composite (HEBM, 1 hour) and consolidated composite (HEBM, 3 hours). This indicates that consolidated composite (HEBM, 1 hour and 3 hours) showed the lowest penetration depth, which suggests an enhanced hardness arising from load transfer from NiAl matrix to MWCNTs. This agrees with the investigation by Attar *et al.,* (2017), they reported that large penetration depth of a sample may depicts low hardness.

The load-displacement plots of the consolidated composite (HEBM, 3 hours) at the heating rate of 100 ^{o}C/min was presented in Figure 6.5(b), indicating the largest penetration depth. Then, it was accompanied by consolidated NiAl, consolidated composite (HEBM, 2 hours) and consolidated composite (HEBM, 1 h). This indicates that consolidated composite (HEBM, 2 hours and 1 hour) showed the lowest penetration depth, which suggests an enhanced hardness arising from load transfer from NiAl matrix to MWCNTs.

The load-displacement plots of the consolidated composite (HEBM, 2 hours) at the heating rate of 150 ^{o}C/min was presented in Figure 6.5(c), indicating the largest penetration depth. Then, it was accompanied by consolidated composite (HEBM, 3 hours), consolidated composite (HEBM, 1 hour) and consolidated NiAl. This indicates that consolidated composite (HEBM, 1 hour and NiAl) showed the lowest penetration depth.

Similarly, the curve of the penetration-depth of the consolidated samples as a function of time, at the heating rates of 50, 100, and 150 ^{o}C/min was presented in Figure 6.6(a-c). The consolidated NiAl was observed with the penetration depths of 835.23 mm, 859.31 mm, and 775.05 mm respectively at 50, 100, and 150 ^{o}C/min. The consolidated composite (HEBM, 1 hour) was observed with the depths of 773.15 mm, 676.45 mm, and 787.94 mm respectively and the

consolidated composite (HEBM, 2 hours) was observed with the depths of 890.17 mm, 828.20 mm, 876.64 mm respectively. Furthermore, the consolidated composite (HEBM, 3 hours) was observed with the depths of 835.17 mm, 828.20 mm, and 876.64 mm respectively at 50, 100, and 150 ^{o}C/min. From all the observation, the consolidated composite (HEBM, 1 hour) depicts the maximum resistance to the load with the depths of 773.15 mm, 676.45 mm, and 787.94 mm respectively at the heating rates of 50, 100, and 150 ^{o}C/min. This may be attributed to pinning effect of dislocation motion of MWCNTs, thereby enhancing the stiffness and hardness of the composite. Also, this composite showed a relative dispersion of nanotubes as compared to the other composites.

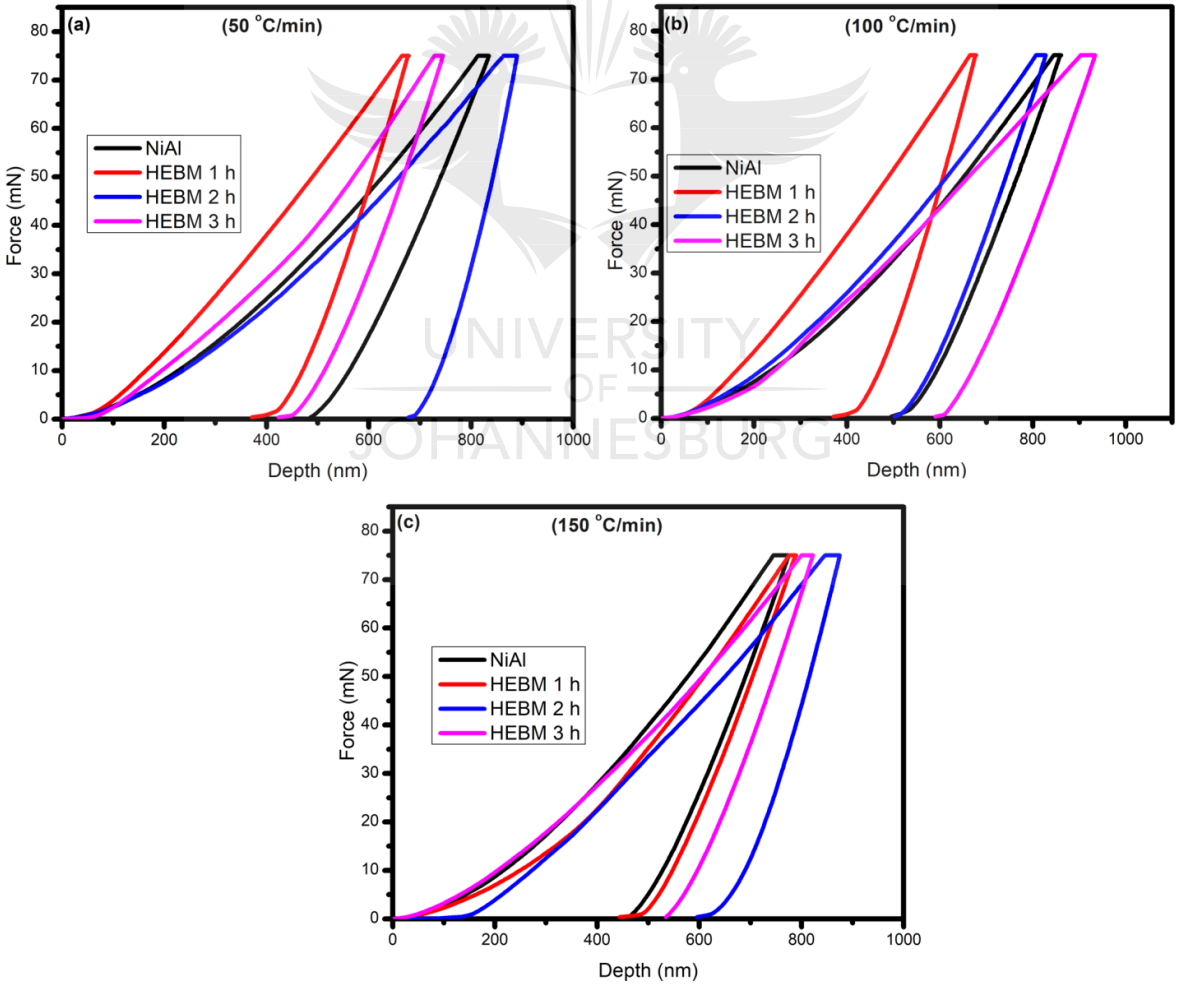

Figure 6.5. The plot of the load against depth of all the consolidated samples between the heating rates of 50-150 ^{o}C/min.

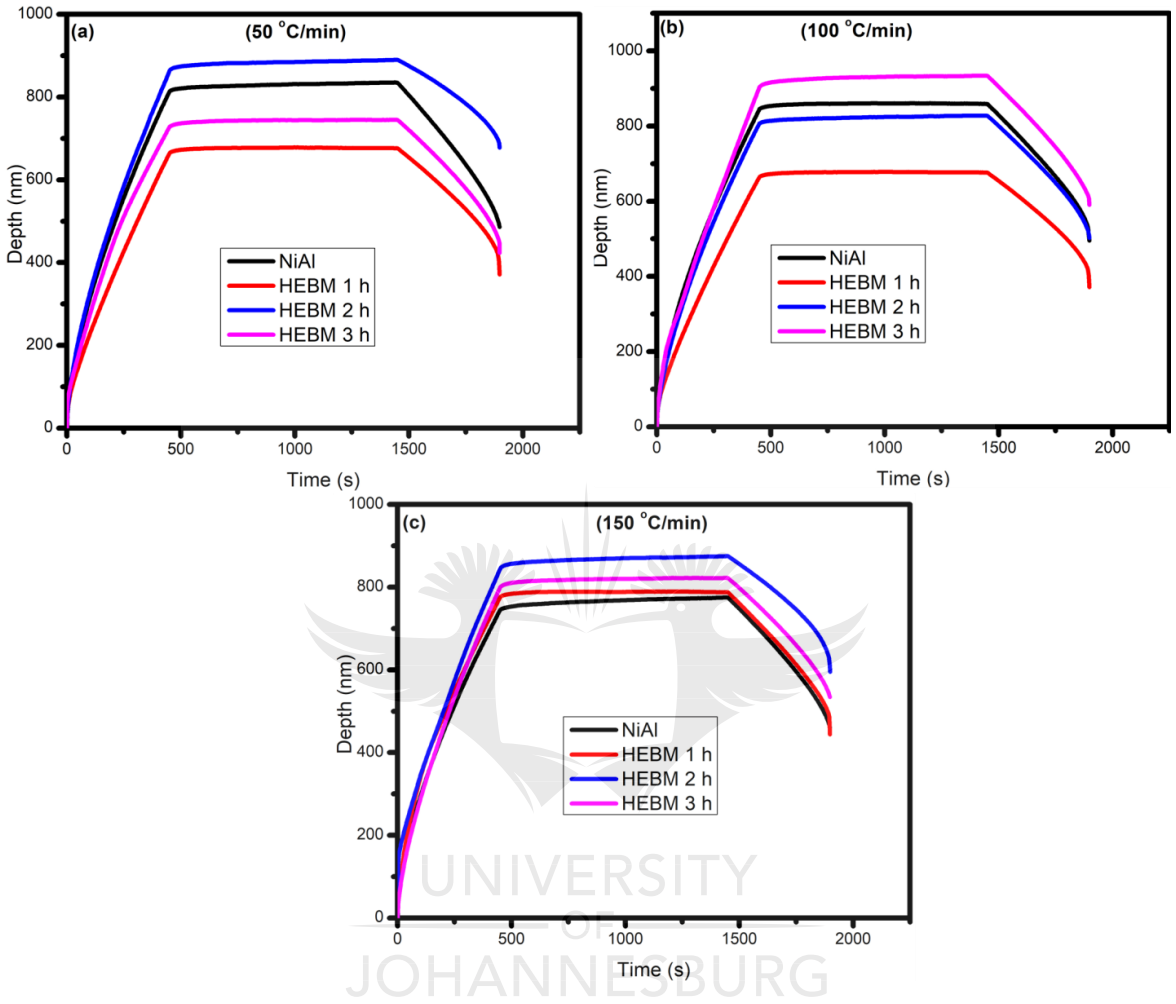

Figure 6.6. The plot of the penetration depth against time of all the consolidated samples between the heating rates of 50-150 ^{o}C/min.

6.5.1 Nanohardness and elastic modulus

The nanohardness of the consolidated NiAl and NiAl-MWCNTs composites (HEBM, 1 hour, 2 hours, and 3 hours) at the heating rates of 50, 100, and 150 ^{o}C/min were presented in Figure 6.7. The consolidated NiAl was observed with the nanohardness of 9278 MPa, 6534 MPa, and 10447 MPa at the indentation load of 75 mN. The consolidated composite (HEBM, 1 hour) was observed with the nanohardness of 9982 MPa, 13310 MPa, and 10171 MPa respectively and the

consolidated composite (HEBM, 2 hours) was observed with the nanohardness of 5428 MPa, 8908 MPa, and 6168 MPa respectively. Furthermore, the consolidated composite (HEBM, 3 hours) was observed with the nanohardness of 10908 MPa, 8406 MPa, and 8203 MPa respectively at the indentation load of 75 mN. It was observed that the consolidated composite (HEBM, 1 hour) depicts the best combination of nanohardness at the indentation load due to relative dispersion of nanotubes. Similarly, the elastic modulus of the consolidated NiAl and NiAl-MWCNTs composites (HEBM, 1 hour, 2 hours, and 3 hours) at the heating rates of 50, 100, and 150 ^{o}C/min were presented in Figure 6.8. The consolidated NiAl was observed with the elastic modulus of 80.1 GPa, 77.7 GPa, and 97.1 GPa at the indentation load of 75 mN. The consolidated composite (HEBM, 1 hour) was observed with the elastic modulus of 101.4 GPa, 139.2 GPa, and 95.7 GPa respectively and the consolidated composite (HEBM, 2 hours) was observed with the elastic modulus of 134.8 GPa, 86.8 GPa, and 109.4 GPa respectively. Furthermore, the consolidated composite (HEBM, 3 hours) was observed with the elastic modulus of 109.5 GPa, 69.8 GPa, and 95.9 GPa respectively at the indentation load of 75 mN. From the results, the consolidated composite (HEBM, 1 hour) depicts the best combination of elastic modulus at the indentation load of 75 mN, apparently due to the relative dispersion of nanotubes which impact stiffness in the composite. This further suggests better load transfer from the NiAl matrix to the nanotubes (Lin *et al.*, 2015).

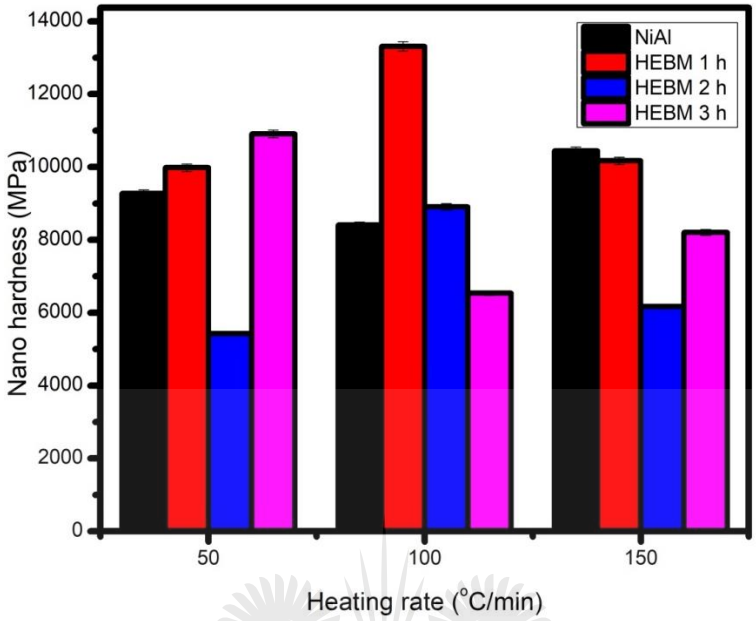

Figure 6.7. The nanohardness of all the consolidated samples between the heating rates of 50-150 °C/min.

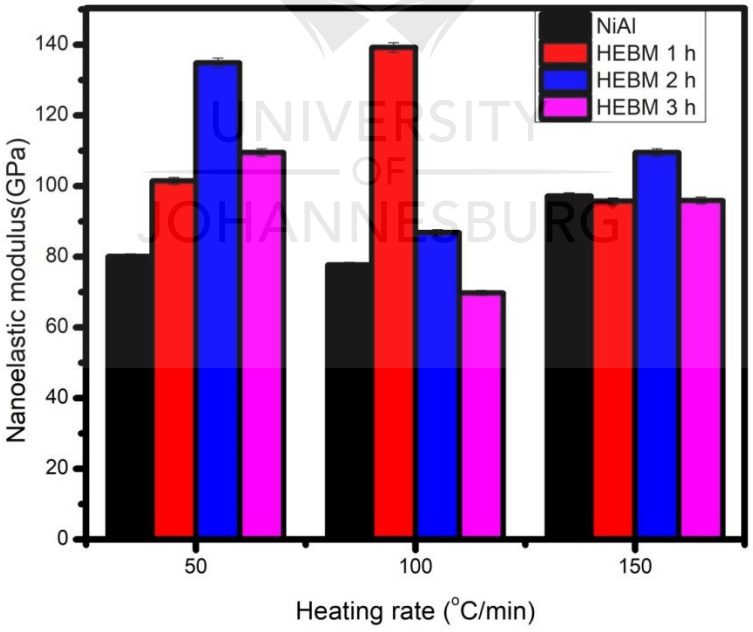

Figure 6.8. The nanoelastic modulus of all the consolidated samples between the heating rates of 50-150 °C/min.

6.6 WEAR ANALYSIS OF THE CONSOLIDATED SAMPLES

The tribology analysis of the consolidated samples was carried out at the heating rate of 150 ^{o}C/min using a ball on disc tribometer at different applied load. The coefficient of friction (COF) against time of all the consolidated samples were investigated. Figure 6.9 shows the coefficient of friction against the sliding time of all the consolidated samples under the applied load of 2 N. It was observed that the consolidated composite (HEBM, 3 hours) had the least mean or average coefficient of friction with the value of 0.57. This was followed by the consolidated composite (HEBM, 1 hour), with the mean COF value of 0.67. Meanwhile, the consolidated composite (HEBM, 2 hours), was found with the mean COF value of 0.67 and the consolidated NiAl showed the highest mean COF value of 0.78. It was duly observed that the presence of MWCNTs decreased the COF of the consolidated composites. From Figure 6.10, the COF against the sliding time of all the consolidated samples were observed under the exerted load of 5 N. The curve of the COF against the sliding time shows that, consolidated composite (HEBM, 3 hours) had the least average coefficient of friction with the value of 0.47. This was followed by the consolidated NiAl, with the mean COF value of 0.55. Meanwhile, the consolidated composite (HEBM, 1 hour), was found with the mean COF value of 0.60 and the consolidated composite (HEBM, 2 hours) showed the highest mean COF value of 0.93. Subsequently, the COF against time of the consolidated samples under the applied of 8 N was also investigated as seen in Figure 6.11 The consolidated composite (HEBM, 3 hours) revealed the least average coefficient of friction with the value of 0.50. This was followed by the consolidated NiAl, with the mean COF value of 0.65. Meanwhile, the consolidated composite (HEBM, 2 hours), was found with the mean COF value of 0.68 and the consolidated composite (HEBM, 1 hour) showed the highest mean COF value of 0.83. Comparatively, it could be seen that consolidated composite (HEBM, 3 hours) showed the least mean COF at the applied

loads of 2 N, 5 N and 8 N. This may be attributed to better relative density and hardness observed in the composite at the heating rate of 150 ^{o}C/min as illustrated in Table 6.2. The presence of the MWCNTs in the NiAl matrix also played a major role in decreasing the COF through the deformation and breaking of CNTs during the wear test which formed a lubricating tribolayer at the contact area (Mallikarjuna *et al.*, 2017; M. Zhou *et al.*, 2017). Figure 6.12 shows the plot of the COF against the applied load, it was observed that the COF decreased as the load was increased from 2 N to 5 N, may be due to increase in surface roughening of the samples. It was further increased when the load was increased to 8 N, (attributed to low quality of wear debris observed as higher load) (Chowdhury *et al.*, 2011), except for the dispersed composite with the HEBM of 2 hour which was observed to increase from the applied load of 2 N to 5 N.

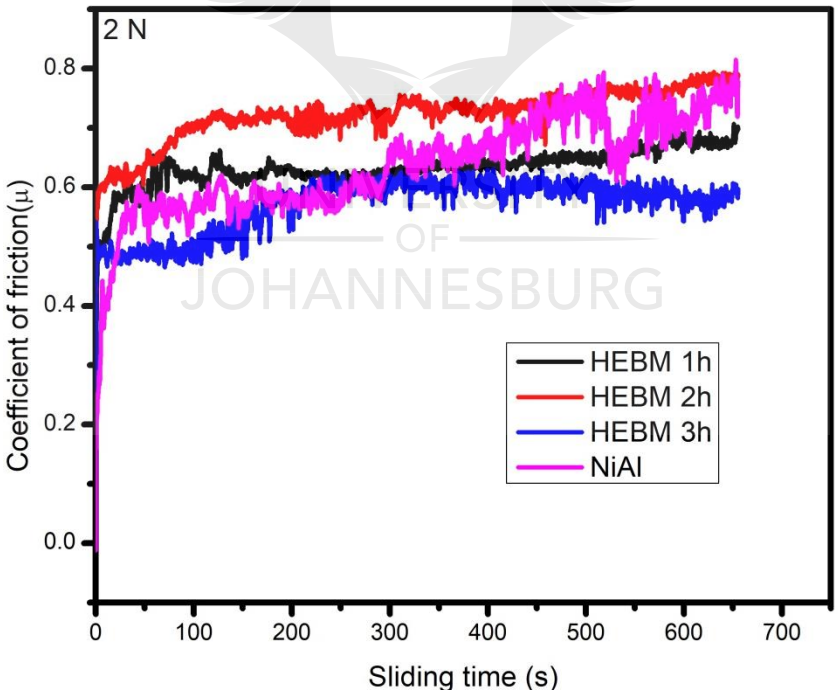

Figure 6.9. The curve of the COF against the sliding time of the consolidated samples at 2 N.

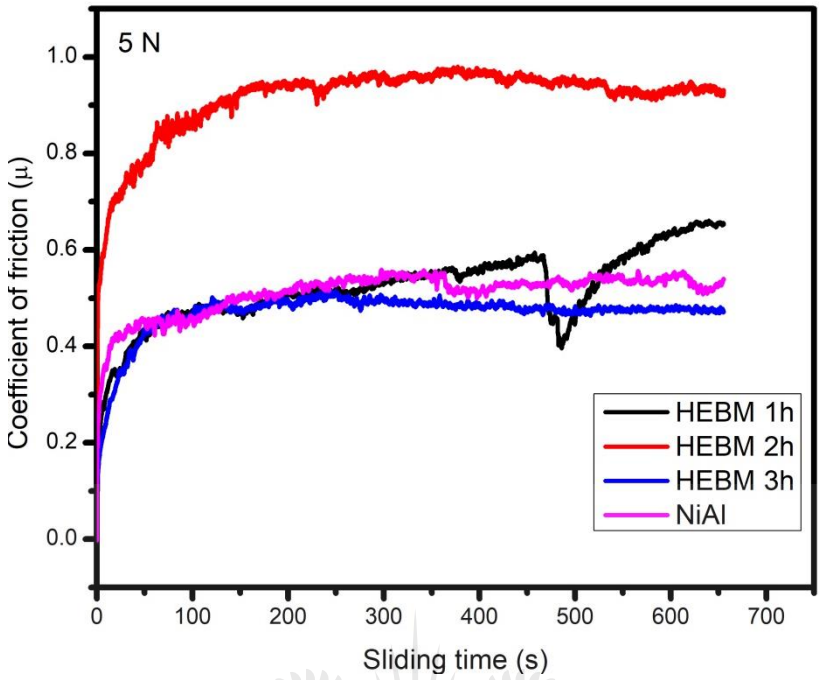

Figure 6.10 The curve of the COF against the sliding time of the sintered samples 5 N.

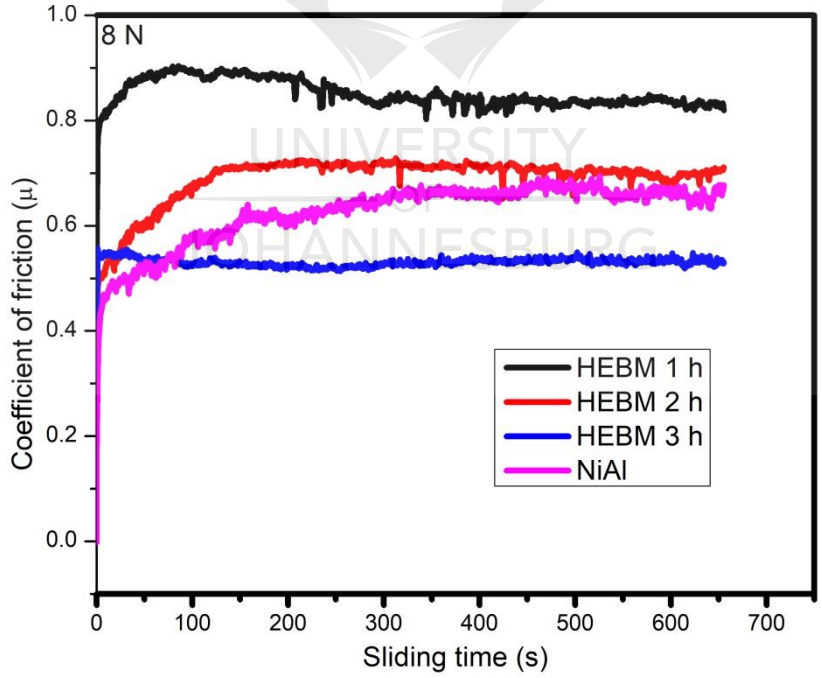

Figure 6.11. The curve of the COF against the sliding time of the sintered samples 8 N.

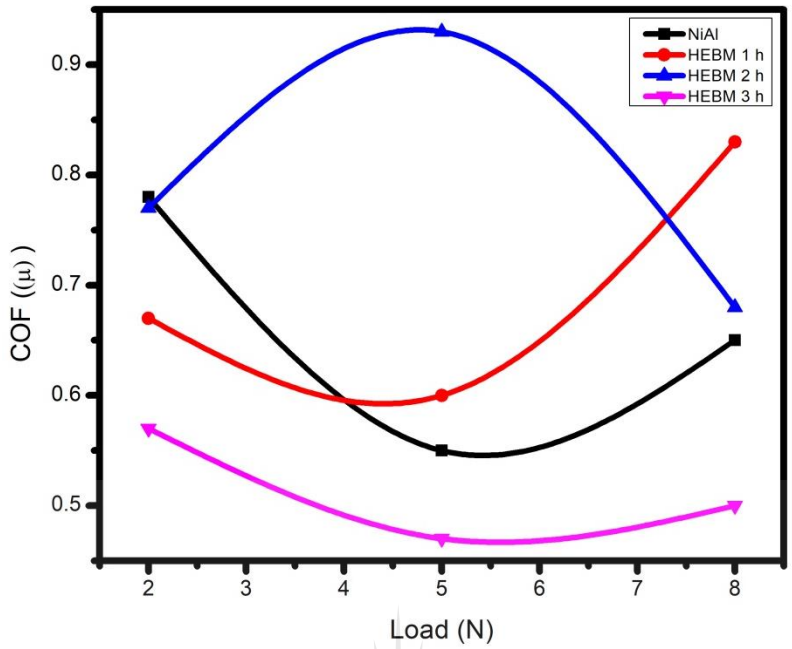

Figure 6.12. The curve of the COF against the load (2, 5, and 8 N) of the consolidated samples.

Table 6.2: Sintering parameters, mechanical properties and coefficient of friction.

SC	ST (°C)	HR (°C/min	RD (%)	VMH (HV)	NH (GPA)	NE (GPa)	COF (μ) 2 N	COF (μ) 5 N	COF (μ) 8 N
NiAl	1000	50	94.9	380.8±4.0	9.2±0.1	80.1±0.8	-	-	-
NiAl	1000	100	90.8	327.4±3.3	8.4±0.1	77.7±0.7	-	-	-
NiAl	1000	150	96.2	413±4.1	104±0.2	97.1±0.9	0.78	0.55	0.65
HE 1 h	1000	50	95.8	311.4±3.0	9.9±0.1	101.4±1.0	-	-	-
HE 1 h	1000	100	88.5	293.1±2.9	13.3±0.2	139.2±1.3	-	-	-
HE 1 h	1000	150	86.2	264.6±2.6	10.1±0.1	95.7±0.9	0.67	0.60	0.83
HE 2 h	1000	50	94.5	287.3±2.9	5.4±0.1	134.8±1.3	-	-	-
HE 2 h	1000	100	88.2	275.1±2.7	8.9±0.2	86.8±0.8	-	-	-
HE 2 h	1000	150	85.8	259.5±2.6	6.1±0.1	109.4±1.0	0.77	0.93	0.68
HE 3 h	1000	50	92.3	283.9±3.0	10.9±0.1	109.5±1.1	-	-	-
HE 3 h	1000	100	88.1	267±2.7	6.5±0.2	69.8±0.7	-	-	-
HE 3 h	1000	150	88.7	281.5±3.2	8.2±0.3	95.9±1.0	0.57	0.47	0.50

SC: Sample code, ST: Sintering temperature, HR: Heating rate, RD: Relative density, VMH: Vickers hardness, NH: Nanohardness, NE: Nanoelastic modulus, COF: Coefficient of friction, and HE: HEBM.

6.7 SUMMARY

Chapter seven discussed the mechanical and tribology properties of the consolidated samples at the heating rates of 50, 100, and 150 ^{o}C/min. The densification mechanism of the consolidated samples at the heating rate of 50 ^{o}C/min, showed that the samples had enough time for the densification process to take place as compared to the other sintered samples at the heating rate of 100 ^{o}C/min and 150 ^{o}C/min. The Vickers microhardness and the relative density of the consolidated NiAl decreased from 50-100 ^{o}C/min and it further increased as the heating rate was increased. For the consolidated composites, it decreased as the heating rates were increased. The load-displacement plots were used to determine the nanohardness and nanoelastic modulus values of the consolidated samples. It could be seen that consolidated samples with higher penetration depths at the indentation load of 75 mN had lower nanohardness values. Also, the presence of MWCNTs may have improved the elastic modulus and the wear property of the consolidated composites.

7 CONTRIBUTIONS, CONLUSION AND RECOMMENDATION

7.1 CONTRIBUTION TO KNOWLEDGE

The investigation on the dispersion and influence of heating rates on the mechanical properties of spark plasma sintered multi-walled carbon nanotubes reinforced nickel aluminide is promising due to the intrinsic properties of the materials. Even though, several studies have been reported on the spark plasma sintering of nickel aluminide composites but the influence of heating rates on its mechanical properties and crystallographic orientations has not been sufficiently reported. As a result, it was necessary to explore the dispersion and the consolidation of multi-walled nanotubes reinforced nickel aluminide composite powders. The following contributions were made;

The developed NiAl-MWCNTs composite was achieved through the combination of two planetary ball millings and the dispersion characteristics of MWCNTs was observed through the variation of the HEBM hours, which has not been previously reported in the literature. The effect of heating rates on the mechanical properties of the fabricated NiAl-MWCNTs composites showed a decrease as the heating rates increased. The nanoindentation analysis of the developed NiAl-MWCNTs composite have been evaluated and discussed in this research work. This provided insights on the significant roles of nanotubes in enhancing the nanohardness and nanoelastic modulus of the composite. There have been controversial opinions as far as the influence of high heating rate on the grain size of consolidated samples from the literatures. Some researchers are of the opinion that high heating rate would increase or decrease grain size based on surface diffusion, power law creep and grain boundary diffusion. This study has contributed to the body of knowledge by providing information that high heating rate would increase grain size of the consolidated composite because of the retained nanotubes agglomerates within the metal matrix which hindered the sintering process.

7.2 CONCLUSION

The dispersion of MWCNTs in NiAl matrix through the unique planetary ball millings and their consolidation by spark plasma sintering has been discussed in this research work. The influence of heating rates between 50-150 ^{o}C/min on the microstructures, phase identifications, crystal orientations and mechanical properties of the sintered composites have been evaluated and the following conclusions were made:

The SEM micrograph of the milled NiAl powder showed large rough particles which was obtained as a result of cold welding and fracturing of the particles and this was confirmed by the XRD patterns of the sample. This further showed relative dispersions and agglomerations of MWCNTs within the NiAl-MWCNTs composites, in which the agglomerations increased with the milling time. This was corroborated by the Raman analysis which indicated an increase in I_D/I_G ratio of MWCNTs for the dispersed composites as the heating rates increased. Furthermore, the TEM analysis revealed that the coaxial and halo rings of the composite-powders were not intact, and it gradually faded out as the milling time was increased due to the presence of strain. The microstructures of the consolidated NiAl revealed the presence of pores, while the consolidated composites (HEBM, 1 hour, 2 hours and 3 hours) showed the presence of retained MWCNTs agglomerates which retards sintering procedure and thereby increased the pores within the composites as the heating rates increased. The grain size of the consolidated composites increased as the heating rate was increased, and the crystallographic orientations depicts no predominant of any colour which suggests no formation of texture. The relative density and Vickers microhardness of the consolidated composites decreased as the heating rate increases because of the increase in porosity due to the presence of nanotubes agglomerates. Nanoindentation curves showed that higher penetration depths translate to low nanohardness and the presence of MWCNTs was

responsible for better elastic modulus of the consolidated composites. The dispersion of nanotubes had significant impacts on the nanoindentation properties and the consolidated composite (HEBM, 1 hour) had the best combination of nanohardness and elastic modulus due to relative dispersion of MWCNTs observed in the composite. Also, better coefficient of friction was achieved due to the lubricating properties of the nanotubes.

7.3 RECOMMENDATION

In this study, the consolidated composites had shown good mechanical properties, but there are areas of concerns that could be improve in this investigation. It is obvious that better dispersion of nanotubes within NiAl matrix without defects would translates to better and improve mechanical properties. The ball milling procedures can be improved through proper optimization of the milling (HEBM) parameters and different contents of MWCNTs can be utilized for better assessment of grain refinement. Optimization of the sintering parameters especially the sintering temperature, holding time can be investigated to achieve excellent mechanical properties that would be utilized for high temperature applications in the aerospace industry.

REFERENCES

Adegbenjo, A O, Olubambi, P. A., Potgieter, J. H., Shongwe, M. B., & Ramakokovhu, M. (2017). Spark plasma sintering of graphitized multi-walled carbon nanotube reinforced Ti6Al4V. *Materials & Design*, *128*, 119–129.

Adegbenjo, Adewale Oladapo, Obadele, B. A., & Olubambi, P. A. (2018). Densification, hardness and tribological characteristics of MWCNTs reinforced Ti6Al4V compacts consolidated by spark plasma sintering. *Journal of Alloys and Compounds*, *749*, 818–833. https://doi.org/10.1016/j.jallcom.2018.03.373

Agarwal, A., Bakshi, S. R., & Lahiri, D. (2016). *Carbon nanotubes: reinforced metal matrix composites*. CRC press.

Ajayan, P. M., & Ebbesen, T. W. (1997). Nanometre-size tubes of carbon. *Reports on Progress in Physics*, *60*(10), 1025.

Aliyu, I. K., Saheb, N., Hassan, S. F., & Al-Aqeeli, N. (2015). Microstructure and Properties of Spark Plasma Sintered Aluminum Containing 1 wt.% SiC Nanoparticles. *Metals*, *5*(1), 70–83. https://www.mdpi.com/2075-4701/5/1/70

Allaedini, G., Mahmoudi, E., Aminayi, P., Tasirin, S. M., & Mohammad, A. W. (2016). Optical investigation of reduced graphene oxide and reduced graphene oxide/CNTs grown via simple CVD method. *Synthetic Metals*, *220*, 72–77.

Ameri, S., Sadeghian, Z., & Kazeminezhad, I. (2016). Effect of CNT addition approach on the microstructure and properties of NiAl-CNT nanocomposites produced by mechanical alloying and spark plasma sintering. *Intermetallics*, *76*, 41–48.

https://doi.org/https://doi.org/10.1016/j.intermet.2016.06.010

Arai, S., Endo, M., & Kaneko, N. (2004). Ni-deposited multi-walled carbon nanotubes by electrodeposition. *Carbon*, *42*(3), 641–644.

Asadabad, M. A., & Eskandari, M. J. (2016). Electron diffraction. In *Modern Electron Microscopy in Physical and Life Sciences*. IntechOpen.

Attar, H., Ehtemam-Haghighi, S., Kent, D., Okulov, I. V, Wendrock, H., Bönisch, M., Volegov, A. S., Calin, M., Eckert, J., & Dargusch, M. S. (2017). Nanoindentation and wear properties of Ti and Ti-TiB composite materials produced by selective laser melting. *Materials Science and Engineering: A*, *688*, 20–26.

Ayache, J., Beaunier, L., Boumendil, J., Ehret, G., & Laub, D. (2010). *Sample preparation handbook for transmission electron microscopy: techniques* (Vol. 2). Springer Science & Business Media.

Azarniya, A., Azarniya, A., Sovizi, S., Hosseini, H. R. M., Varol, T., Kawasaki, A., & Ramakrishna, S. (2017). Physicomechanical properties of spark plasma sintered carbon nanotube-reinforced metal matrix nanocomposites. *Progress in Materials Science*, *90*, 276–324.

Azarniya, A., Safavi, M. S., Sovizi, S., Azarniya, A., Chen, B., Madaah Hosseini, H. R., & Ramakrishna, S. (2017). Metallurgical Challenges in Carbon Nanotube-Reinforced Metal Matrix Nanocomposites. *Metals*, *7*(10), 384. http://www.mdpi.com/2075-4701/7/10/384

Bakshi, S. R., Lahiri, D., & Agarwal, A. (2010). Carbon nanotube reinforced metal matrix composites - a review. *International Materials Reviews*, *55*(1), 41–64.

https://doi.org/10.1179/095066009X12572530170543

Belin, T., & Epron, F. (2005). Characterization methods of carbon nanotubes: a review. *Materials Science and Engineering: B*, *119*(2), 105–118. https://doi.org/https://doi.org/10.1016/j.mseb.2005.02.046

Benjamin, J S, & Volin, T. E. (1974). The mechanism of mechanical alloying. *Metallurgical Transactions*, *5*(8), 1929–1934. https://doi.org/10.1007/bf02644161

Benjamin, John S. (1990). Mechanical alloying — A perspective. *Metal Powder Report*, *45*(2), 122–127. https://doi.org/https://doi.org/10.1016/S0026-0657(10)80124-9

Bethune, D. S., H. Klang, C., de Vries, M., Gs, G., Savoy, R. J., Vazquez, J., & Beyers, R. (1993). *Cobalt-Catalysed Growth of Carbon Nanotubes With Single-Atomic-Layer Walls* (Vol. 363). https://doi.org/10.1038/363605a0

Bhat, A., Balla, V. K., Bysakh, S., Basu, D., Bose, S., & Bandyopadhyay, A. (2011). Carbon nanotube reinforced Cu–10Sn alloy composites: mechanical and thermal properties. *Materials Science and Engineering: A*, *528*(22–23), 6727–6732.

Bochenek, K., & Basista, M. (2015). Advances in processing of NiAl intermetallic alloys and composites for high temperature aerospace applications. *Progress in Aerospace Sciences*, *79*, 136–146. https://doi.org/https://doi.org/10.1016/j.paerosci.2015.09.003

Bonifacio, C. S., Rufner, J. F., Holland, T. B., & van Benthem, K. (2012). In situ transmission electron microscopy study of dielectric breakdown of surface oxides during electric field-assisted sintering of nickel nanoparticles. *Applied Physics Letters*, *101*(9), 93107.

Bowman, R. R., Noebe, R. D., & Darolia, R. (1989). Mechanical properties and deformation

mechanisms of NiAl. *HITEMP Review*, 41–47.

Cahn, R. W. (1991). Load-bearing ordered intermetallic compounds—a historical view. *MRS Bulletin*, *16*(5), 18–23.

Cavaliere, P., Sadeghi, B., & Shabani, A. (2017). Carbon nanotube reinforced aluminum matrix composites produced by spark plasma sintering. *Journal of Materials Science*, *52*(14), 8618–8629. https://doi.org/10.1007/s10853-017-1086-6

Chaim, R. (2007). Densification mechanisms in spark plasma sintering of nanocrystalline ceramics. *Materials Science and Engineering: A*, *443*(1–2), 25–32.

Changrong, X., Xiaoxia, G., Fanqing, L., Dingkun, P., & Guangyao, M. (2001). Preparation of asymmetric Ni/ceramic composite membrane by electroless plating. *Colloids and Surfaces A: Physicochemical and Engineering Aspects*, *179*(2–3), 229–235.

Chawla, K. K. (2006). Metal matrix composites. *Materials Science and Technology*.

Chen, B, Kondoh, K., Imai, H., Umeda, J., & Takahashi, M. (2016). Simultaneously enhancing strength and ductility of carbon nanotube/aluminum composites by improving bonding conditions. *Scripta Materialia*, *113*, 158–162.

Chen, Biao, Li, S., Imai, H., Jia, L., Umeda, J., Takahashi, M., & Kondoh, K. (2015). Load transfer strengthening in carbon nanotubes reinforced metal matrix composites via in-situ tensile tests. *Composites Science and Technology*, *113*, 1–8. https://doi.org/https://doi.org/10.1016/j.compscitech.2015.03.009

Chen, W. X., Tu, J. P., Wang, L. Y., Gan, H. Y., Xu, Z. D., & Zhang, X. B. (2003). Tribological application of carbon nanotubes in a metal-based composite coating and composites.

Carbon, *41*(2), 215–222.

Chen, X., Zhang, G., Chen, C., Zhou, L., Li, S., & Li, X. (2003). Carbon nanotube composite deposits with high hardness and high wear resistance. *Advanced Engineering Materials*, *5*(7), 514–518.

Chen, X H, Cheng, F. Q., Li, S. L., Zhou, L. P., & Li, D. Y. (2002). Electrodeposited nickel composites containing carbon nanotubes. *Surface and Coatings Technology*, *155*(2–3), 274–278.

Chen, Xu HUAN, Peng, J. C., Li, X. Q., Deng, F. M., Wang, J. X., & Li, W. Z. (2001). Tribological behavior of carbon nanotubes—reinforced nickel matrix composite coatings. *Journal of Materials Science Letters*, *20*(22), 2057–2060.

ChhowallaM, A., & Amaratunga, G. A. J. (2001). Synthesis of carbon 'onions' in water. *Nature*, *414*, 506–507.

Cho, Y., Choi, G., & Kim, D. (2006). A method to fabricate field emission tip arrays by electrocodeposition of single-wall carbon nanotubes and nickel. *Electrochemical and Solid-State Letters*, *9*(3), G107–G110.

Choa, Y.-H., Yang, J.-K., Kim, B.-H., Jeong, Y.-K., Lee, J.-S., Nakayama, T., Sekino, T., & Niihara, K. (2003). Preparation and characterization of metal/ceramic nanoporous nanocomposite powders. *Journal of Magnetism and Magnetic Materials*, *266*(1–2), 12–19.

Chowdhury, M. A., Khalil, M. K., Nuruzzaman, D. M., & Rahaman, M. L. (2011). The effect of sliding speed and normal load on friction and wear property of aluminum. *International Journal of Mechanical and Mechanics Engineering*, *11*(1), 53–57.

Chrzanowska, J., Hoffman, J., Małolepszy, A., Mazurkiewicz, M., Kowalewski, T. A., Szymanski, Z., & Stobinski, L. (2015). Synthesis of carbon nanotubes by the laser ablation method: Effect of laser wavelength. *Physica Status Solidi (B)*, *252*(8), 1860–1867.

Conshohocken, W. (1996). ASTM International, E112: Standard Test Methods for Determining Average Grain Size. *West Conshocken*, *96*(2004), 1–26. https://doi.org/10.1520/E0112-10.Copyright

Darolia, R. (1991). NiAl alloys for high-temperature structural applications. *JOM*, *43*(3), 44–49. https://doi.org/10.1007/bf03220163

Das, T., Munroe, P., Bandyopadhyay, S., Bell, T., & Swain, M. V. (1997). Interfacial behaviour of 6061/ AI 2 0 3 l11etal l11atrix cOl11posites. *Processing*, *13*(September), 778–784. https://doi.org/10.1179/mst.1997.13.9.778

Delaney, P., Choi, H. J., Ihm, J., Louie, S. G., & Cohen, M. L. (1998). Broken symmetry and pseudogaps in ropes of carbon nanotubes. *Nature*, *391*(6666), 466.

Delhaes, P., Couzi, M., Trinquecoste, M., Dentzer, J., Hamidou, H., & Vix-Guterl, C. (2006). A comparison between Raman spectroscopy and surface characterizations of multiwall carbon nanotubes. *Carbon*, *44*(14), 3005–3013.

Deng, C. F., Ma, Y. X., Zhang, P., Zhang, X. X., & Wang, D. Z. (2008). Thermal expansion behaviors of aluminum composite reinforced with carbon nanotubes. *Materials Letters*, *62*(15), 2301–2303. https://doi.org/https://doi.org/10.1016/j.matlet.2007.11.086

Desai, A. V, & Haque, M. A. (2005). Mechanics of the interface for carbon nanotube–polymer composites. *Thin-Walled Structures*, *43*(11), 1787–1803.

https://doi.org/https://doi.org/10.1016/j.tws.2005.07.003

Devaraj, S., Sankaran, S., & Kumar, R. (2013). Influence of spark plasma sintering temperature on the densification, microstructure and mechanical properties of Al-4.5 wt.%Cu alloy. *Acta Metallurgica Sinica (English Letters)*, *26*(6), 761–771. https://doi.org/10.1007/s40195-013-0159-z

Dey, A., & Pandey, K. M. (2015). MAGNESIUM METAL MATRIX COMPOSITES-A REVIEW. *Reviews on Advanced Materials Science*, *42*(1).

Diouf, S., & Molinari, A. (2012). Densification mechanisms in spark plasma sintering: Effect of particle size and pressure. *Powder Technology*, *221*, 220–227. https://doi.org/https://doi.org/10.1016/j.powtec.2012.01.005

Dollar, M., Dymek, S., Hwang, S. J., & Nash, P. (1992). The occurrence of< 110> slip in NiAl. *Scripta Metallurgica et Materialia*, *26*(1), 29–34.

Dresselhaus, M S, Dresselhaus, G., & Saito, R. (1995). Physics of carbon nanotubes. *Carbon*, *33*(7), 883–891.

Ducati, C., Koziol, K., Friedrichs, S., Yates, T. J. V, Shaffer, M. S., Midgley, P. A., & Windle, A. H. (2006). Crystallographic order in multi-walled carbon nanotubes synthesized in the presence of nitrogen. *Small*, *2*(6), 774–784.

Duque, J. G., Parra-Vasquez, A. N. G., Behabtu, N., Green, M. J., Higginbotham, A. L., Price, B. K., Leonard, A. D., Schmidt, H. K., Lounis, B., & Tour, J. M. (2010). Diameter-dependent solubility of single-walled carbon nanotubes. *ACS Nano*, *4*(6), 3063–3072.

Džunić, D., Mitrović, S., Babić, M., Bobić, I., Pantić, M., Adamović, D., & Nedeljković, B.

(2015). Nanoindentation of Za-27 Alloy Based Nanocomposites Reinforced with Al 2 O 3 Particles. *Tribology in Industry*, *37*(4).

Esawi, A. M. K., Morsi, K., Sayed, A., Taher, M., & Lanka, S. (2010). Effect of carbon nanotube (CNT) content on the mechanical properties of CNT-reinforced aluminium composites. *Composites Science and Technology*, *70*(16), 2237–2241. https://doi.org/https://doi.org/10.1016/j.compscitech.2010.05.004

Esawi, A., & Morsi, K. (2007). Dispersion of carbon nanotubes (CNTs) in aluminum powder. *Composites Part A: Applied Science and Manufacturing*, *38*(2), 646–650. https://doi.org/10.1016/j.compositesa.2006.04.006

Falodun, O. E., Obadele, B. A., Oke, S. R., Maja, M. E., & Olubambi, P. A. (2018). Effect of sintering parameters on densification and microstructural evolution of nano-sized titanium nitride reinforced titanium alloys. *Journal of Alloys and Compounds*, *736*, 202–210.

Falodun, O. E., Obadele, B. A., Oke, S. R., Okoro, A. M., & Olubambi, P. A. (2019). Titanium-based matrix composites reinforced with particulate, microstructure, and mechanical properties using spark plasma sintering technique: a review. *The International Journal of Advanced Manufacturing Technology*. https://doi.org/10.1007/s00170-018-03281-x

Feng, Y., Yuan, H. L., & Zhang, M. (2005). Fabrication and properties of silver-matrix composites reinforced by carbon nanotubes. *Materials Characterization*, *55*(3), 211–218.

Ferrari, A. C. (2007). Solid State Communications. Raman spectroscopy of graphene and graphite: Disorder, electron–phonon coupling, doping and nonadiabatic effects. *Solid State Commun*, *143*, 47–57.

Ferrer-Anglada, N., Gomis, V., El-Hachemi, Z., Weglikovska, U. D., Kaempgen, M., & Roth, S. (2006). Carbon nanotube based composites for electronic applications: CNT–conducting polymers, CNT–Cu. *Physica Status Solidi (A)*, *203*(6), 1082–1087.

Field, R. D., Lahrman, D. F., & Darolia, R. (1991). Slip systems in< 001> oriented NiAl single crystals. *Acta Metallurgica et Materialia*, *39*(12), 2951–2959.

Fischer-Cripps, A. C. (2006). Critical review of analysis and interpretation of nanoindentation test data. *Surface and Coatings Technology*, *200*(14), 4153–4165. https://doi.org/https://doi.org/10.1016/j.surfcoat.2005.03.018

Foiles, S. M., & Daw, M. S. (2011). Application of the embedded atom method to Ni3Al. *Journal of Materials Research*, *2*(1), 5–15. https://doi.org/10.1557/JMR.1987.0005

Friedrichs, S., Windle, A. H., Koziol, K., Ducati, C., & Midgley, P. A. (2005). Single-chirality multi-walled carbon nanotubes. *Microscopy and Microanalysis*, *11*(S02), 1536–1537.

Frommeyer, G., & Rablbauer, R. (2008). High temperature materials based on the intermetallic compound NiAl reinforced by refractory metals for advanced energy conversion technologies. *Steel Research International*, *79*(7), 507–512.

Gamaly, E. G., & Ebbesen, T. W. (1995). Mechanism of carbon nanotube formation in the arc discharge. *Physical Review B*, *52*(3), 2083.

Geist, D., Gammer, C., Rentenberger, C., & Karnthaler, H. P. (2015). Sessile dislocations by reactions in NiAl severely deformed at room temperature. *Journal of Alloys and Compounds*, *621*, 371–377. https://doi.org/https://doi.org/10.1016/j.jallcom.2014.09.226

George, E. P., & Liu, C. T. (1990). Brittle fracture and grain boundary chemistry of microalloyed

NiAl. *Journal of Materials Research*, *5*(4), 754–762.

Gill, P., & Munroe, N. (2012). Study of carbon nanotubes in Cu-Cr metal matrix composites. *Journal of Materials Engineering and Performance*, *21*(11), 2467–2471.

Goh, C. S., Wei, J., Lee, L. C., & Gupta, M. (2005). Development of novel carbon nanotube reinforced magnesium nanocomposites using the powder metallurgy technique. *Nanotechnology*, *17*(1), 7.

Grabke, H. J. (1999). Oxidation of NiAl and FeAl. *Intermetallics*, *7*(10), 1153–1158. https://doi.org/https://doi.org/10.1016/S0966-9795(99)00037-0

Guo, B., Ni, S., Yi, J., Shen, R., Tang, Z., Du, Y., & Song, M. (2017). Microstructures and mechanical properties of carbon nanotubes reinforced pure aluminum composites synthesized by spark plasma sintering and hot rolling. *Materials Science and Engineering: A*, *698*, 282–288.

Guo, C., Zuo, Y., Zhao, X., Zhao, J., & Xiong, J. (2007). The effects of pulse–reverse parameters on the properties of Ni–carbon nanotubes composite coatings. *Surface and Coatings Technology*, *201*(24), 9491–9496.

Guo, T., Nikolaev, P., Thess, A., Colbert, D. T., & Smalley, R. E. (1995). Catalytic growth of single-walled manotubes by laser vaporization. *Chemical Physics Letters*, *243*(1–2), 49–54.

Guo, W.-M., Vleugels, J., Zhang, G.-J., Wang, P.-L., & Van der Biest, O. (2010). Effect of heating rate on densification, microstructure and strength of spark plasma sintered ZrB2-based ceramics. *Scripta Materialia*, *62*(10), 802–805. https://doi.org/https://doi.org/10.1016/j.scriptamat.2010.02.002

Habibnejad-Korayem, M., Mahmudi, R., & Poole, W. J. (2009). Enhanced properties of Mg-based nano-composites reinforced with Al2O3 nano-particles. *Materials Science and Engineering: A*, *519*(1–2), 198–203.

Harris, P. J. F. (1999). Carbon Nanotubes and Related Structures. Cambridge University Press. *Cambridge, UK*.

Hayat, M. D., Singh, H., He, Z., & Cao, P. (2019). Titanium metal matrix composites: An overview. *Composites Part A: Applied Science and Manufacturing*, *121*, 418–438. https://doi.org/https://doi.org/10.1016/j.compositesa.2019.04.005

He, T., He, X., Tang, P., Chu, D., Wang, X., & Li, P. (2017). The use of cryogenic milling to prepare high performance Al2009 matrix composites with dispersive carbon nanotubes. *Materials and Design*, *114*, 373–382. https://doi.org/10.1016/j.matdes.2016.11.008

Hu, W., Weirich, T., Hallstedt, B., Chen, H., Zhong, Y., & Gottstein, G. (2006). Interface structure, chemistry and properties of NiAl composites fabricated from matrix-coated single-crystalline Al2O3 fibres (sapphire) with and without an hBN interlayer. *Acta Materialia*, *54*(9), 2473–2488. https://doi.org/https://doi.org/10.1016/j.actamat.2006.01.032

Huang, L., Wu, B., Chen, J., Xue, Y., Liu, Y., Kajiura, H., & Li, Y. (2011). Synthesis of single-walled carbon nanotubes by an arc-discharge method using selenium as a promoter. *Carbon*, *49*(14), 4792–4800. https://doi.org/https://doi.org/10.1016/j.carbon.2011.06.091

Huang, Y. Y., & Terentjev, E. M. (2012). Dispersion of carbon nanotubes: mixing, sonication, stabilization, and composite properties. *Polymers*, *4*(1), 275–295.

Hulbert, D. M., Anders, A., Andersson, J., Lavernia, E. J., & Mukherjee, A. K. (2009). A

discussion on the absence of plasma in spark plasma sintering. *Scripta Materialia*, *60*(10), 835–838.

Iijima, S. (1991). Helical microtubules of graphitic carbon. *Nature*, *354*(6348), 56–58. https://doi.org/10.1038/354056a0

Iijima, S., & Ichihashi, T. (1993). Single-shell carbon nanotubes of 1-nm diameter. *Nature*, *363*(6430), 603.

Jafari Eskandari, M., Asadabad, M. A., Tafrishi, R., & Emamalizadeh, M. (2017). Transmission electron microscopy characterization of different nanotubes. *Inorganic and Nano-Metal Chemistry*, *47*(2), 197–201. https://doi.org/10.1080/15533174.2015.1137317

Jia, H., Zhang, Z., Qi, Z., Liu, G., & Bian, X. (2009). Formation of nanocrystalline TiC from titanium and different carbon sources by mechanical alloying. *Journal of Alloys and Compounds*, *472*(1–2), 97–103.

Journet, C., Maser, W. K., Bernier, P., Loiseau, A., de La Chapelle, M. L., Lefrant, dl S., Deniard, P., Lee, R., & Fischer, J. E. (1997). Large-scale production of single-walled carbon nanotubes by the electric-arc technique. *Nature*, *388*(6644), 756.

Kang, I., Schulz, M. J., Kim, J. H., Shanov, V., & Shi, D. (2006). A carbon nanotube strain sensor for structural health monitoring. *Smart Materials and Structures*, *15*(3), 737.

Kessel, H. U., & Hennicke, J. (2007). Aspects concerning the super-fast sintering of powder metallic and ceramic materials. *International Ceramic Review*, *56*(3), 164–166.

Kessel, H. U., Hennicke, J., Kirchner, R., & Kessel, T. (2010). Rapid sintering of novel materials by FAST/SPS—Further development to the point of an industrial production process with

high cost efficiency. *FCT Systeme GmbH*, *96528*.

Khalil, A., Hakeem, A. S., & Saheb, N. (2011). Optimization of process parameters in spark plasma sintering Al6061 and Al2124 aluminum alloys. *Advanced Materials Research*, *328*, 1517–1522.

Khalil, K. A. (2012). Advanced sintering of nano-ceramic materials. In *Ceramic Materials-Progress in Modern Ceramics*. InTech.

Kim, J. A., Seong, D. G., Kang, T. J., & Youn, J. R. (2006). Effects of surface modification on rheological and mechanical properties of CNT/epoxy composites. *Carbon*, *44*(10), 1898–1905.

Kim, T. A., Oh, S. M., Nahm, K. S., & Mo, Y. H. (2006). Preparation of Silicon-CNT (Carbon Nano Tube) Composites for Anode in Lithium Secondary Batteries. *Meeting Abstracts*, *3*, 163.

Kondoh, K., Threrujirapapong, T., Imai, H., Umeda, J., & Fugetsu, B. (2009). Characteristics of powder metallurgy pure titanium matrix composite reinforced with multi-wall carbon nanotubes. *Composites Science and Technology*, *69*(7), 1077–1081.

Kong, J., Cassell, A. M., & Dai, H. (1998). Chemical vapor deposition of methane for single-walled carbon nanotubes. *Chemical Physics Letters*, *292*(4), 567–574. https://doi.org/https://doi.org/10.1016/S0009-2614(98)00745-3

Koziol, K., Shaffer, M., & Windle, A. (2005). Three-dimensional internal order in multiwalled carbon nanotubes grown by chemical vapor deposition. *Advanced Materials*, *17*(6), 760–763.

Kumar, R., Singh, R. K., Singh, D. P., Vaz, A. R., Yadav, R. R., Rout, C. S., & Moshkalev, S. A. (2017). Synthesis of self-assembled and hierarchical palladium-CNTs-reduced graphene oxide composites for enhanced field emission properties. *Materials & Design*, *122*, 110–117.

Kumar, S., & Anandaheerthan, J. (2008). Production and Characterisation of Aluminium-Fly Composites using Stir Casting Method. *Department of Metallurgical & Materials Engineering National Institute of Technology Rourkela*.

Lee, C. H., Lu, H. H., Wang, C. A., Nayak, P. K., & Huang, J. L. (2011). Effect of heating rate on spark plasma sintering of a nanosized β-Si3N4-Based Powder. *Journal of the American Ceramic Society*, *94*(4), 1182–1190. https://doi.org/10.1111/j.1551-2916.2010.04196.x

Lehman, J. H., Terrones, M., Mansfield, E., Hurst, K. E., & Meunier, V. (2011). Evaluating the characteristics of multiwall carbon nanotubes. *Carbon*, *49*(8), 2581–2602.

Li, H., Guan, L., Shi, Z., & Gu, Z. (2004). Direct synthesis of high purity single-walled carbon nanotube fibers by arc discharge. *The Journal of Physical Chemistry B*, *108*(15), 4573–4575.

Liao, J., & Tan, M.-J. (2011). Mixing of carbon nanotubes (CNTs) and aluminum powder for powder metallurgy use. *Powder Technology*, *208*(1), 42–48.

Lin, D., Saei, M., Suslov, S., Jin, S., & Cheng, G. J. (2015). Super-strengthening and stabilizing with carbon nanotube harnessed high density nanotwins in metals by shock loading. *Scientific Reports*, *5*(October), 1–11. https://doi.org/10.1038/srep15405

Liu, B., Liu, L. R., & Liu, X. J. (2013). Effects of carbon nanotubes on hardness and internal

stress in Ni–P coatings. *Surface Engineering*, *29*(7), 507–510.

Liu, C. T., White, C. L., & Horton, J. A. (1985). Effect of boron on grain-boundaries in Ni3Al. *Acta Metallurgica*, *33*(2), 213–229.

Liu, E., Jia, J., Bai, Y., Wang, W., & Gao, Y. (2014). Study on preparation and mechanical property of nanocrystalline NiAl intermetallic. *Materials and Design*, *53*, 596–601. https://doi.org/10.1016/j.matdes.2013.07.052

Liu, Z. Y., Xu, S. J., Xiao, B. L., Xue, P., Wang, W. G., & Ma, Z. Y. (2012). Effect of ball-milling time on mechanical properties of carbon nanotubes reinforced aluminum matrix composites. *Composites Part A: Applied Science and Manufacturing*, *43*(12), 2161–2168.

Long, Y., Zhang, H., Wang, T., Huang, X., Li, Y., Wu, J., & Chen, H. (2013). High-strength Ti–6Al–4V with ultrafine-grained structure fabricated by high energy ball milling and spark plasma sintering. *Materials Science and Engineering: A*, *585*(Supplement C), 408–414. https://doi.org/https://doi.org/10.1016/j.msea.2013.07.078

Loretto, M. H., & Wasilewski, R. J. (1971). Slip systems in NiAl single crystals at 300 K and 77 K. *The Philosophical Magazine: A Journal of Theoretical Experimental and Applied Physics*, *23*(186), 1311–1328.

Lucas, A., Zakri, C., Maugey, M., Pasquali, M., Van Der Schoot, P., & Poulin, P. (2009). Kinetics of nanotube and microfiber scission under sonication. *The Journal of Physical Chemistry C*, *113*(48), 20599–20605.

Maja, M. E., Falodun, O. E., Obadele, B. A., Oke, S. R., & Olubambi, P. A. (2018). Nanoindentation studies on TiN nanoceramic reinforced Ti–6Al–4V matrix composite.

Ceramics International, *44*(4), 4419–4425.

Makino, Y. (1998). Application of band parameters to materials design. *ISIJ International*, *38*(9), 925–934.

Mallikarjuna, H. M., Ramesh, C. S., Koppad, P. G., Keshavamurthy, R., & Sethuram, D. (2017). Nanoindentation and wear behaviour of copper based hybrid composites reinforced with SiC and MWCNTs synthesized by spark plasma sintering. *Vacuum*, *145*, 320–333. https://doi.org/https://doi.org/10.1016/j.vacuum.2017.09.016

Matizamhuka, W. R. (2016). Spark plasma sintering (SPS)-an advanced sintering technique for structural nanocomposite materials. *Journal of the Southern African Institute of Mining and Metallurgy*, *116*(12), 1171–1180.

Matsugi, K. (1995). Effect of direct current pulse discharge on specific resistivity of copper and iron powder compacts. *Journal of the Japan Institute of Metals*, *59*, 740–745.

McCARTHY, G. J., & Thedchanamoorthy, A. (1988). Semi-Quantitative X-Ray Diffraction Analysis of Fly Ash by the Reference Intensity Ratio Method. *MRS Online Proceedings Library Archive*, *136*.

Meng, J., Jia, C., & He, Q. (2006). Effect of mechanical alloying on the structure and property of Ni3Al fabricated by hot pressing. *Journal of Alloys and Compounds*, *421*(1), 200–203. https://doi.org/https://doi.org/10.1016/j.jallcom.2005.09.082

Meyyappan, M. (2005). *Carbon nanotubes : science and applications*. CRC Press.

Mohammadnejad, A., Bahrami, A., Sajadi, M., Karimi, P., Fozveh, H. R., & Mehr, M. Y. (2018). Microstructure and mechanical properties of spark plasma sintered nanocrystalline Ni3Al-

xB (0.0< x< 1.5 at%) alloy. *Materials Today Communications*, *17*, 161–168.

Montazeri, A., Montazeri, N., Pourshamsian, K., & Tcharkhtchi, A. (2011). The effect of sonication time and dispersing medium on the mechanical properties of multiwalled carbon nanotube (MWCNT)/epoxy composite. *International Journal of Polymer Analysis and Characterization*, *16*(7), 465–476.

Mordike, B. L., & Ebert, T. (2001). Magnesium: properties—applications—potential. *Materials Science and Engineering: A*, *302*(1), 37–45.

Morsi, K., Esawi, A. M. K., Borah, P., Lanka, S., & Sayed, A. (2010). Characterization and spark plasma sintering of mechanically milled aluminum-carbon nanotube (CNT) composite powders. *Journal of Composite Materials*, *44*(16), 1991–2003. https://doi.org/10.1177/0021998310361990

Mukhopadhyay, K., Dwivedi, C. D., & Mathur, G. N. (2002). Conversion of carbon nanotubes to carbon nanofibers by sonication. *Carbon*, *8*(40), 1373–1376.

Munir, K. S., Kingshott, P., & Wen, C. (2015). Carbon nanotube reinforced titanium metal matrix composites prepared by powder metallurgy—a review. *Critical Reviews in Solid State and Materials Sciences*, *40*(1), 38–55.

Munir, K. S., Li, Y., Liang, D., Qian, M., Xu, W., & Wen, C. (2015). Effect of dispersion method on the deterioration, interfacial interactions and re-agglomeration of carbon nanotubes in titanium metal matrix composites. *Materials & Design*, *88*, 138–148. https://doi.org/https://doi.org/10.1016/j.matdes.2015.08.112

Munir, K. S., Li, Y., Lin, J., & Wen, C. (2018). Interdependencies between graphitization of

carbon nanotubes and strengthening mechanisms in titanium matrix composites. *Materialia*, *3*, 122–138. https://doi.org/https://doi.org/10.1016/j.mtla.2018.08.015

Munir, K. S., & Wen, C. (2016). Deterioration of the strong sp2 carbon network in carbon nanotubes during the mechanical dispersion processing—a review. *Critical Reviews in Solid State and Materials Sciences*, *41*(5), 347–366.

Munir, K. S., Zheng, Y., Zhang, D., Lin, J., Li, Y., & Wen, C. (2017a). Improving the strengthening efficiency of carbon nanotubes in titanium metal matrix composites. *Materials Science and Engineering: A*, *696*, 10–25.

Munir, K. S., Zheng, Y., Zhang, D., Lin, J., Li, Y., & Wen, C. (2017b). Microstructure and mechanical properties of carbon nanotubes reinforced titanium matrix composites fabricated via spark plasma sintering. *Materials Science and Engineering: A*, *688*, 505–523.

Munir, Z. A., Anselmi-Tamburini, U., & Ohyanagi, M. (2006). The effect of electric field and pressure on the synthesis and consolidation of materials: A review of the spark plasma sintering method. *Journal of Materials Science*, *41*(3), 763–777.

MURAYAMA, N., & SHIN, W. (2000). Effect of rapid heating on densification and grain growth in hot pressed alumina. *Journal of the Ceramic Society of Japan*, *108*(1261), 799–802.

Nardone, V. C., & Prewo, K. M. (1986). On the strength of discontinuous silicon carbide reinforced aluminum composites. *Scripta Metallurgica*, *20*(1), 43–48. https://doi.org/10.1016/0036-9748(86)90210-3

Nathal, M. V. (1995). High temperature composites. *Acta Metallurgica Sinica Series A, Physical*

Metallurgy & Materials Science, *8*(4–6), 467–476.

Nishida, Y. (2013). *Introduction to Metal Matrix Composites: Fabrication and Recycling*. Springer Science & Business Media.

Noebe, R. D. (1994). *The effect of various metallurgical parameters on the flow and fracture behavior of polycrystalline NiAl near the brittle-to-ductile transition*.

Noebe, R. D., Bowman, R. R., & Nathal, M. V. (1996). The Physical and Mechanical Metallurgy of NiAl. *Physical Metallurgy and Processing of Intermetallic Compounds*, 212–296. https://doi.org/10.1007/978-1-4613-1215-4_7

Novák, P., Šotka, D., Novák, M., Michalcová, A., Šerák, J., & Vojtěch, D. (2011). Production of NiAl–matrix composites by reactive sintering. *Powder Metallurgy*, *54*(3), 308–313.

Obadele, B. A., Ige, O. O., & Olubambi, P. A. (2017). Fabrication and characterization of titanium-nickel-zirconia matrix composites prepared by spark plasma sintering. *Journal of Alloys and Compounds*, *710*, 825–830.

Oghbaei, M., & Mirzaee, O. (2010). Microwave versus conventional sintering: A review of fundamentals, advantages and applications. *Journal of Alloys and Compounds*, *494*(1), 175–189. https://doi.org/https://doi.org/10.1016/j.jallcom.2010.01.068

Oh, Y., Choi, J., Kim, Y., Kim, K., & Baik, S. (2007). The effects of ball milling process on the diameter dependent fracture of single walled carbon nanotubes. *Scripta Materialia*, *56*(9), 741–744.

Okamoto, H. (2004). Al-Ni (aluminum-nickel). *Journal of Phase Equilibria and Diffusion*, *25*(4), 394.

Okoro, A. M., Machaka, R., Lephuthing, S. S., Awotunde, M. A., Oke, S. R., Falodun, O. E., & Olubambi, P. A. (2019). Dispersion characteristics, interfacial bonding and nanostructural evolution of MWCNT in Ti6Al4V powders prepared by shift speed ball milling technique. *Journal of Alloys and Compounds*. https://doi.org/https://doi.org/10.1016/j.jallcom.2019.01.174

Okoro, A. M., Machaka, R., Lephuthing, S. S., Oke, S. R., Awotunde, M. A., & Olubambi, P. A. (2019). Evaluation of the sinterability, densification behaviour and microhardness of spark plasma sintered multiwall carbon nanotubes reinforced Ti6Al4V nanocomposites. *Ceramics International*. https://doi.org/https://doi.org/10.1016/j.ceramint.2019.06.242

Oliver, W. C., & Pharr, G. M. (2004). Measurement of hardness and elastic modulus by instrumented indentation: Advances in understanding and refinements to methodology. *Journal of Materials Research*, *19*(1), 3–20.

Pekguleryuz, M., & Celikin, M. (2010). Creep resistance in magnesium alloys. *International Materials Reviews*, *55*(4), 197–217.

Pierard, N., Fonseca, A., Konya, Z., Willems, I., Van Tendeloo, G., & B.Nagy, J. (2001). Production of short carbon nanotubes with open tips by ball milling. *Chemical Physics Letters*, *335*(1), 1–8. https://doi.org/https://doi.org/10.1016/S0009-2614(01)00004-5

Pillai, A. M., Rajendra, A., & Sharma, A. K. (2012). Evaluation of effect of grain size on mechanical and tribological properties of pulse electrodeposited nanocrystalline nickel using nanoindentation techniques. *Transactions of the IMF*, *90*(3), 143–148.

Poole Jr, C. P., & Owens, F. J. (2003). *Introduction to nanotechnology*. John Wiley & Sons.

Prabhu, B., Suryanarayana, C., An, L., & Vaidyanathan, R. (2006). Synthesis and characterization of high volume fraction Al–Al2O3 nanocomposite powders by high-energy milling. *Materials Science and Engineering: A*, *425*(1), 192–200. https://doi.org/https://doi.org/10.1016/j.msea.2006.03.066

Qian, D., Dickey, E. C., Andrews, R., & Rantell, T. (2000). Load transfer and deformation mechanisms in carbon nanotube-polystyrene composites. *Applied Physics Letters*, *76*(20), 2868–2870.

Rajan, T. P. D., Pillai, R. M., & Pai, B. C. (1998). Reinforcement coatings and interfaces in aluminium metal matrix composites. *Journal of Materials Science*, *33*(14), 3491–3503.

Rajeswari, K., Hareesh, U. S., Subasri, R., Chakravarty, D., & Johnson, R. (2010). Comparative evaluation of spark plasma (SPS), microwave (MWS), two stage sintering (TSS) and conventional sintering (CRH) on the densification and micro structural evolution of fully stabilized zirconia ceramics. *Science of Sintering*, *42*(3), 259–267.

Rastogi, R., Kaushal, R., Tripathi, S. K., Sharma, A. L., Kaur, I., & Bharadwaj, L. M. (2008). Comparative study of carbon nanotube dispersion using surfactants. *Journal of Colloid and Interface Science*, *328*(2), 421–428.

Reihanian, M., Bagherpour, E., & Paydar, M. H. (2009). A model for volume fraction and particle size selection in tri-modal metal matrix composites. *Materials Science and Engineering: A*, *513–514*, 172–175. https://doi.org/https://doi.org/10.1016/j.msea.2009.01.052

Reinert, L., Zeiger, M., Suarez, S., Presser, V., & Mücklich, F. (2015). Dispersion analysis of

carbon nanotubes, carbon onions, and nanodiamonds for their application as reinforcement phase in nickel metal matrix composites. *Rsc Advances*, *5*(115), 95149–95159.

Ren, Z. F., Huang, Z. P., Xu, J. W., Wang, J. H., Bush, P., Siegal, M. P., & Provencio, P. N. (1998). Synthesis of large arrays of well-aligned carbon nanotubes on glass. *Science*, *282*(5391), 1105–1107.

Rinzler, A. G., Liu, J., Dai, H., Nikolaev, P., Huffman, C. B., Rodriguez-Macias, F. J., Boul, P. J., Lu, A. H., Heymann, D., & Colbert, D. T. (1998). Large-scale purification of single-wall carbon nanotubes: process, product, and characterization. *Applied Physics A: Materials Science & Processing*, *67*(1), 29–37.

Robertson, I. M., & Wayman, C. M. (1984). Ni5Al3 and the nickel-aluminum binary phase diagram. *Metallography*, *17*(1), 43–55.

Rohatgi, P. K., Yarandi, F. M., Liu, Y., & Asthana, R. (1991). Segregation of silicon carbide by settling and particle pushing in cast aluminum-silicon-carbide particle composite. *Materials Science and Engineering A*, *147*(1), L1. https://doi.org/10.1016/0921-5093(91)90813-3

Rosca, I. D., Watari, F., Uo, M., & Akasaka, T. (2005). Oxidation of multiwalled carbon nanotubes by nitric acid. *Carbon*, *43*(15), 3124–3131.

Ruzicka, A. M., & Hugo, R. C. (2018). Electron backscatter diffraction (EBSD) study of seven heavily metamorphosed chondrites: Deformation systematics and variations in pre-shock temperature and post-shock annealing. *Geochimica et Cosmochimica Acta*, *234*, 115–147.

Saito, R., Fujita, M., Dresselhaus, G., & S Dresselhaus, M. (1992). *Electronic-Structure of Chiral Graphene Tubules* (Vol. 60). https://doi.org/10.1063/1.107080

Salama, E. I., Abbas, A., & Esawi, A. M. K. (2017). Preparation and properties of dual-matrix carbon nanotube-reinforced aluminum composites. *Composites Part A: Applied Science and Manufacturing*, *99*, 84–93.

Salvetat, J.-P., Bonard, J.-M., Thomson, N. H., Kulik, A. J., Forro, L., Benoit, W., & Zuppiroli, L. (1999). Mechanical properties of carbon nanotubes. *Applied Physics A*, *69*(3), 255–260.

Sauthoff, G. (1989). Intermetallic phases-materials developments and prospects. *Zeitschrift Für Metallkunde*, *80*(5), 337–344.

Schilke, P. W., & Schenectady, N. Y. (2004). Advanced Gas Turbine Materials and Coatings Gas Turbine Repair Technology. *Paper No. GER G*, *3569*.

Schulson, E. M., & Barker, D. R. (1983). *A brittle to ductile transition in NiAl of a critical grain size*.

Shelimov, K. B., Esenaliev, R. O., Rinzler, A. G., Huffman, C. B., & Smalley, R. E. (1998). Purification of single-wall carbon nanotubes by ultrasonically assisted filtration. *Chemical Physics Letters*, *282*(5–6), 429–434.

Shen, Z., Johnsson, M., Zhao, Z., & Nygren, M. (2002). Spark plasma sintering of alumina. *Journal of the American Ceramic Society*, *85*(8), 1921–1927.

Shi, X. L., Yang, H., Shao, G. Q., Duan, X. L., Yan, L., Xiong, Z., & Sun, P. (2007). Fabrication and properties of W–Cu alloy reinforced by multi-walled carbon nanotubes. *Materials Science and Engineering: A*, *457*(1–2), 18–23.

Shi, Y. L., Yang, Z., Li, M. K., Xu, H., & Li, H. L. (2004). Electroplated synthesis of Ni–P–UFD, Ni–P–CNTs, and Ni–P–UFD–CNTs composite coatings as hydrogen evolution

electrodes. *Materials Chemistry and Physics*, *87*(1), 154–161.

Shu, J., Li, H., Yang, R., Shi, Y., & Huang, X. (2006). Cage-like carbon nanotubes/Si composite as anode material for lithium ion batteries. *Electrochemistry Communications*, *8*(1), 51–54.

Siegel, R. W., Chang, S. K., Ash, B. J., Stone, J., Ajayan, P. M., Doremus, R. W., & Schadler, L. S. (2001). Mechanical behavior of polymer and ceramic matrix nanocomposites. *Scripta Materialia*, *44*(8–9), 2061–2064.

Simões, S., Viana, F., Reis, M. A. L., & Vieira, M. F. (2014). Improved dispersion of carbon nanotubes in aluminum nanocomposites. *Composite Structures*, *108*, 992–1000.

Singerman, S. A., Jackson, J. J., & Lynn, M. (1996). Titanium metal matrix composites for aerospace applications. *Superalloys 1996, Proceedings of Eighth International Symposium on Superalloys*.

Singh, L. K., Bhadauria, A., Jana, S., & Laha, T. (2018a). Effect of sintering temperature and heating rate on crystallite size, densification behaviour and mechanical properties of Al-MWCNT nanocomposite consolidated via spark plasma sintering. *Acta Metallurgica Sinica (English Letters)*, *31*(10), 1019–1030.

Singh, L. K., Bhadauria, A., Jana, S., & Laha, T. (2018b). Effect of Sintering Temperature and Heating Rate on Crystallite Size, Densification Behaviour and Mechanical Properties of Al-MWCNT Nanocomposite Consolidated via Spark Plasma Sintering. *Acta Metallurgica Sinica (English Letters)*, *31*(10), 1019–1030. https://doi.org/10.1007/s40195-018-0795-4

Snyder, A., Bo, Z., Hodson, S., Fisher, T., & Stanciu, L. (2012). The effect of heating rate and composition on the properties of spark plasma sintered zirconium diboride based

composites. *Materials Science and Engineering: A*, *538*, 98–102. https://doi.org/https://doi.org/10.1016/j.msea.2012.01.019

Sreekanth, P. S. R., Acharyya, K., Talukdar, I., & Kanagaraj, S. (2014). Studies on structural defects on 60Co irradiated multi walled carbon nanotubes. *Procedia Materials Science*, *6*, 1967–1975.

Suárez, M., Fernández, A., Menéndez, J. L., Torrecillas, R., Kessel, H. U., Hennicke, J., Kirchner, R., & Kessel, T. (2013). Challenges and Opportunities for Spark Plasma Sintering: A Key Technology for a New Generation of Materials. In B. Ertuğ (Ed.), *Sintering Applications* (p. Ch. 13). InTech. https://doi.org/10.5772/53706

Suárez, S., Ramos-Moore, E., Lechthaler, B., & Mücklich, F. (2014). Grain growth analysis of multiwalled carbon nanotube-reinforced bulk Ni composites. *Carbon*, *70*, 173–178.

Sung-Kyu, K. I. M., & Tae-Sung, O. H. (2011). Electrodeposition behavior and characteristics of Ni-carbon nanotube composite coatings. *Transactions of Nonferrous Metals Society of China*, *21*, s68–s72.

Suryanarayana, C. (2001). Mechanical alloying and milling. *Progress in Materials Science*, *46*(1), 1–184. https://doi.org/https://doi.org/10.1016/S0079-6425(99)00010-9

Talaş, Ş. (2018). *3 - Nickel aluminides* (R. B. T.-I. M. C. Mitra (ed.); pp. 37–69). Woodhead Publishing. https://doi.org/https://doi.org/10.1016/B978-0-85709-346-2.00003-0

Terrones, M. (2003). Science and Technology of the Twenty-First Century: Synthesis, Properties, and Applications of Carbon Nanotubes. *Annual Review of Materials Research*, *33*(1), 419–501. https://doi.org/10.1146/annurev.matsci.33.012802.100255

Thess, A., Lee, R., Nikolaev, P., Dai, H., Petit, P., Robert, J., Xu, C., Lee, Y. H., Kim, S. G., & Rinzler, A. G. (1996). Crystalline ropes of metallic carbon nanotubes. *Science, 273*(5274), 483–487.

Thostenson, E. T., Ren, Z., & Chou, T.-W. (2001). Advances in the science and technology of carbon nanotubes and their composites: a review. *Composites Science and Technology*, *61*(13), 1899–1912. https://doi.org/https://doi.org/10.1016/S0266-3538(01)00094-X

Tokita, M. (2015). Recent and future progress on advanced ceramics sintering by Spark Plasma Sintering. *Nanotechnologies in Russia*, *10*(3–4), 261–267. https://doi.org/10.1134/S1995078015020202

Vasanthakumar, K., Karthiselva, N. S., Chawake, N. M., & Bakshi, S. R. (2017). Formation of TiCx during reactive spark plasma sintering of mechanically milled Ti/carbon nanotube mixtures. *Journal of Alloys and Compounds*, *709*, 829–841. https://doi.org/10.1016/j.jallcom.2017.03.216

Vedula, K., Hahn, K. H., & Boulogne, B. (1988). Room temperature tensile ductility in polycrystalline B2 NiAl. *MRS Online Proceedings Library Archive*, *133*.

Vittori Antisari, M., Marazzi, R., & Krsmanovic, R. (2003). Synthesis of multiwall carbon nanotubes by electric arc discharge in liquid environments. *Carbon*, *41*(12), 2393–2401. https://doi.org/https://doi.org/10.1016/S0008-6223(03)00297-5

Wachtell L. Richard. (1952). An Investigation of Various Properties of NiAl. In *In W ADC TR 52-291* (pp. 1–45).

Wang, Q., Han, Y., Wang, Y., Qin, Y., & Guo, Z.-X. (2008). Effect of surfactant structure on the

stability of carbon nanotubes in aqueous solution. *The Journal of Physical Chemistry B*, *112*(24), 7227–7233.

Wang, Y. H., Li, Y. N., Lu, J., Zang, J. B., & Huang, H. (2006). Microstructure and thermal characteristic of Si-coated multi-walled carbon nanotubes. *Nanotechnology*, *17*(15), 3817.

Wasilewski, R. J., Butler, S. R., & Hanlon, J. E. (1967). Plastic deformation of single-crystal NiAl. *AIME MET SOC TRANS*, *239*(9), 1357–1364.

White, B., Banerjee, S., O'Brien, S., Turro, N. J., & Herman, I. P. (2007). Zeta-potential measurements of surfactant-wrapped individual single-walled carbon nanotubes. *The Journal of Physical Chemistry C*, *111*(37), 13684–13690.

Wichmann, M. H. G., Schulte, K., & Wagner, H. D. (2008). On nanocomposite toughness. *Composites Science and Technology*, *68*(1), 329–331. https://doi.org/10.1016/j.compscitech.2007.06.027

Wilson, T., Tyburski, A., DePies, M. R., Vilches, O. E., Becquet, D., & Bienfait, M. (2002). Adsorption of H2 and D2 on carbon nanotube bundles. *Journal of Low Temperature Physics*, *126*(1–2), 403–408.

Wong, W. L. E., & Gupta, M. (2007). Development of Mg/Cu nanocomposites using microwave assisted rapid sintering. *Composites Science and Technology*, *67*(7–8), 1541–1552.

WOOD, D. L., GRENOBLE, H. E., and WESTBROOK, J. H. (1964). Effect of Basic Physical Parameters on Engineering Properties of Intermetallic Compounds. In *Report WADD TR-60-184, Pts. I-VII, Wright-Patterson AFB, OH.* (pp. 1–29).

Xing, Y., Li, L., Chusuei, C. C., & Hull, R. V. (2005). Sonochemical oxidation of multiwalled

carbon nanotubes. *Langmuir*, *21*(9), 4185–4190.

Xiong, N., Bao, R., Yi, J., Fang, D., Tao, J., & Liu, Y. (2019). CNTs/Cu-Ti composites fabrication through the synergistic reinforcement of CNTs and in situ generated nano-TiC particles. *Journal of Alloys and Compounds*, *770*, 204–213. https://doi.org/https://doi.org/10.1016/j.jallcom.2018.08.116

Xu, C. L., Wei, B. Q., Ma, R. Z., Liang, J., Ma, X. K., & Wu, D. H. (1999). Fabrication of aluminum–carbon nanotube composites and their electrical properties. *Carbon*, *37*(5), 855–858. https://doi.org/https://doi.org/10.1016/S0008-6223(98)00285-1

Xu, R., Tan, Z., Xiong, D., Fan, G., Guo, Q., Zhang, J., Su, Y., Li, Z., & Zhang, D. (2017). Balanced strength and ductility in CNT/Al composites achieved by flake powder metallurgy via shift-speed ball milling. *Composites Part A: Applied Science and Manufacturing*, *96*, 57–66. https://doi.org/https://doi.org/10.1016/j.compositesa.2017.02.017

Yadav, V., & Harimkar, S. P. (2011). Microstructure and properties of spark plasma sintered carbon nanotube reinforced aluminum matrix composites. *Advanced Engineering Materials*, *13*(12), 1128–1134. https://doi.org/10.1002/adem.201100132

Yakobson, B. I., & Avouris, P. (2001). Mechanical Properties of Carbon Nanotubes. In Mildred S Dresselhaus, G. Dresselhaus, & P. Avouris (Eds.), *Carbon Nanotubes: Synthesis, Structure, Properties, and Applications* (pp. 287–327). Springer Berlin Heidelberg. https://doi.org/10.1007/3-540-39947-x_12

Yang, Y. L., Wang, Y. D., Ren, Y., He, C. S., Deng, J. N., Nan, J., Chen, J. G., & Zuo, L. (2008). Single-walled carbon nanotube-reinforced copper composite coatings prepared by

electrodeposition under ultrasonic field. *Materials Letters*, *62*(1), 47–50. https://doi.org/https://doi.org/10.1016/j.matlet.2007.04.086

Ye, J., Ajdelsztajn, L., & Schoenung, J. M. (2006). Bulk nanocrystalline aluminum 5083 alloy fabricated by a novel technique: Cryomilling and spark plasma sintering. *Metallurgical and Materials Transactions A: Physical Metallurgy and Materials Science*, *37*(8), 2569–2579. https://doi.org/10.1007/BF02586229

Yu, J., Grossiord, N., Koning, C. E., & Loos, J. (2007). Controlling the dispersion of multi-wall carbon nanotubes in aqueous surfactant solution. *Carbon*, *45*(3), 618–623.

Yu, M.-F., Lourie, O., Dyer, M. J., Moloni, K., Kelly, T. F., & Ruoff, R. S. (2000). Strength and breaking mechanism of multiwalled carbon nanotubes under tensile load. *Science*, *287*(5453), 637–640.

Zeng, X., Zhou, G., Xu, Q., Xiong, Y., Luo, C., & Wu, J. (2010). A new technique for dispersion of carbon nanotube in a metal melt. *Materials Science and Engineering: A*, *527*(20), 5335–5340. https://doi.org/https://doi.org/10.1016/j.msea.2010.05.005

Zhang, J. F., Shen, J., Shang, Z., Feng, Z. R., Wang, L. S., & Fu, H. Z. (2012). Microstructure and room temperature fracture toughness of directionally solidified NiAl-Mo eutectic in situ composites. *Intermetallics*, *21*(1), 18–25. https://doi.org/10.1016/j.intermet.2011.10.002

Zhang, Y., Gu, H., & Iijima, S. (1998). Single-wall carbon nanotubes synthesized by laser ablation in a nitrogen atmosphere. *Applied Physics Letters*, *73*(26), 3827–3829.

Zhang, Y., & Iijima, S. (1999). Formation of single-wall carbon nanotubes by laser ablation of fullerenes at low temperature. *Applied Physics Letters*, *75*(20), 3087–3089.

Zhang, Z. H., Shen, X. B., Wang, F. C., Lee, S. K., & Wang, L. (2010). Densification behavior and mechanical properties of the spark plasma sintered monolithic TiB2 ceramics. *Materials Science and Engineering A*, *527*(21–22), 5947–5951. https://doi.org/10.1016/j.msea.2010.05.086

Zhaohui, Z., Fuchi, W., Lin, W., Shukui, L., & Osamu, S. (2008). Sintering mechanism of large-scale ultrafine-grained copper prepared by SPS method. *Materials Letters*, *62*(24), 3987–3990.

Zhou, M., Qu, X., Ren, L., Fan, L., Zhang, Y., Guo, Y., Quan, G., Tang, Q., Liu, B., & Sun, H. (2017). The effects of carbon nanotubes on the mechanical and wear properties of AZ31 alloy. *Materials*, *10*(12), 1385.

Zhou, S., Zhang, X., Ding, Z., Min, C., Xu, G., & Zhu, W. (2007). Fabrication and tribological properties of carbon nanotubes reinforced Al composites prepared by pressureless infiltration technique. *Composites Part A: Applied Science and Manufacturing*, *38*(2), 301–306.

Zhu, J., Wei, S., Ryu, J., Budhathoki, M., Liang, G., & Guo, Z. (2010). In situ stabilized carbon nanofiber (CNF) reinforced epoxy nanocomposites. *Journal of Materials Chemistry*, *20*(23), 4937–4948.